

UNCLASS

SECURITY CLASSIFICATION OF THIS PAGE (When Data Entered)

READ INSTRUCTIONS
BEFORE COMPLETING FORM

REPORT DOCUMENTATION PAGE

1. REPORT NUMBER AFIT/CI/NR 83-37D		2. GOVT ACCESSION NO. AD-A132-543		3. REPORT'S CATALOG NUMBER	
4. TITLE (and Subtitle) A Study of Thick-Target X-Ray Spectra Using Photonuclear Reactions				5. TYPE OF REPORT & PERIOD COVERED THESIS/DISSERTATION	
7. AUTHOR(s) Karl L. Prado				6. PERFORMING ORG. REPORT NUMBER	
9. PERFORMING ORGANIZATION NAME AND ADDRESS AFIT STUDENT AT: University of Oklahoma				8. CONTRACT OR GRANT NUMBER(s)	
11. CONTROLLING OFFICE NAME AND ADDRESS AFIT/NR WPAFB OH 45433				10. PROGRAM ELEMENT, PROJECT, TASK AREA & WORK UNIT NUMBERS	
12. REPORT DATE 1983				13. NUMBER OF PAGES 183	
14. MONITORING AGENCY NAME & ADDRESS (if different from Controlling Office)				15. SECURITY CLASS. (of this report) UNCLASS	
16. DISTRIBUTION STATEMENT (of this Report) APPROVED FOR PUBLIC RELEASE; DISTRIBUTION UNLIMITED				15a. DECLASSIFICATION DOWNGRADING SCHEDULE	
17. DISTRIBUTION STATEMENT (of the abstract entered in Block 20, if different from Report)					
18. SUPPLEMENTARY NOTES APPROVED FOR PUBLIC RELEASE: IAW AFR 190-17 9 SEP 1983 Lynn E. Wolaver Dean for Research and Professional Development					
19. KEY WORDS (Continue on reverse side if necessary and identify by block number)					
20. ABSTRACT (Continue on reverse side if necessary and identify by block number) ATTACHED					

AD-A132-543

DTIC FILE COPY

DTIC
SEP 16 1983
S H

83-37

THE UNIVERSITY OF OKLAHOMA
GRADUATE COLLEGE

A STUDY OF THICK-TARGET X-RAY SPECTRA
USING PHOTONUCLEAR REACTIONS

A DISSERTATION
SUBMITTED TO THE GRADUATE FACULTY
in partial fulfillment of the requirements for the
degree of
DOCTOR OF PHILOSOPHY



BY
KARL L. PRADO
Oklahoma City, Oklahoma
1983

Accession For	
NTIS GRA&I	<input checked="" type="checkbox"/>
DTIC TAB	<input type="checkbox"/>
Unannounced	<input type="checkbox"/>
Justification	
By _____	
Distribution/	
Availability Codes	
and number	
Date	
A	

Gamma

Superscript 25

A STUDY OF THICK-TARGET X-RAY SPECTRA
USING PHOTONUCLEAR REACTIONS

By: Karl L. Prado

Megavoltage bremsstrahlung spectra which are produced in thick targets were investigated using photonuclear reactions. Ratios of photonuclear yields in teflon and in K_2SiF_6 were obtained that serve as sensitive indexes of thick target x-ray quality and endpoint energy in the energy range from about 14 to 30 MeV. Because thick target bremsstrahlung spectra have never before been used in the determination of photonuclear reaction cross sections, a numerical analysis computer calculation of thick target bremsstrahlung spectra was written to approximate the spectra of x-rays produced in thick targets of clinical electron linear accelerators and examine the feasibility of using such spectra for cross section determinations. The spectra obtained by computer simulation were used to calculate the photonuclear cross section of the $^{27}Al(\gamma, 2p)^{25}Na$ reaction from 25 to 33 MeV. The calculated cross section is reported and is compared to a previously reported cross section and to a cross section calculated using thin target bremsstrahlung spectra. Analysis of the results obtained indicate that thick target x-ray spectra can be used for photonuclear reaction cross section determination.

A-1

83 09 15 031

© 1983

KARL L. PRADO

ALL RIGHTS RESERVED

ACKNOWLEDGEMENTS

With deep appreciation and gratitude I acknowledge the assistance given me by all the people with whom I have been associated during the course of this research.

I am especially indebted to Dr. David Anderson for his guidance and support during the performance of this research project. His enthusiasm and patience were particularly helpful during times of experimental difficulties.

I am also indebted to Dr. Gail Adams for the academic and professional guidance he provided me during my studies at the University of Oklahoma. Studying under him has been a genuine privilege.

I wish to express my appreciation to the remaining members of my Graduate Committee: Dr. Bhagwat Ahluwalia, Dr. William Graham and Dr. Helmut Fischbeck, for their constructive criticism of this work. I also wish to thank them for their unselfish sharing of their experience and knowledge.

Appreciation is extended to Dr. Carl Bogardus and the Department of Radiation Therapy for allowing me to use the department's excellent facilities. I wish to thank Lou Vittes for his technical assistance with the accelerator and electronic components used in the research project. I also wish to thank Glenda Sims for taking time from her busy schedule to type this dissertation.

In addition, I wish to thank the staff of the Oklahoma University Health Sciences Center Computer Services for the programming assistance provided me.

Lastly, I wish to express my deepest appreciation and love to my wife, Belinda, and my children, Karlo, Marcos, and Sonya for their constant understanding and moral support. To them this work is humbly dedicated.

TABLE OF CONTENTS

	Page
LIST OF TABLES	vii
LIST OF ILLUSTRATIONS	viii
CHAPTER	
I. INTRODUCTION	1
II. THEORY	10
III. MATERIALS AND METHODS	58
IV. RESULTS	106
V. CONCLUSIONS	142
LIST OF REFERENCES	146
APPENDICES	
APPENDIX A	152
APPENDIX B	168
APPENDIX C	178
APPENDIX D	188
APPENDIX E	197
APPENDIX F	210

LIST OF TABLES

Table	Page
1. Photonuclear Reactions Used for Ratios	61
2. $^{27}\text{Al}(\gamma, 2p)^{25}\text{Na}$ Reaction	63
3. Linear Accelerator Operating Parameters	76
4. Sources used in Counting System Energy Scale Calibration	80
5. NBS Sources used in Counting System Efficiency Calibration	81
6. Counting System Photopeak Efficiency	83
7. Experimental Runs used to Compute Photonuclear Ratios	112
8. K_2SiF_6 Ratios	113
9. Teflon Ratios	114
10. Effect of Filtration on Photonuclear Ratios	118
B1. Transition Selection Rules	175
B2. Values of Statistical Factor S as a Function of Multipole order L	177

LIST OF ILLUSTRATIONS

Figure	Page
1. ^{16}O harmonic oscillator shell levels (a) and spin-orbit coupling levels (b)	19
2. Photonuclear yield as an overlap integral	22
3. A "stepwise" approximation to the bremsstrahlung spectrum of endpoint T_1	28
4. The bremsstrahlung process	35
5. Bremsstrahlung spectra from thin and thick targets	42
6. Growth of radioisotope of decay constant λ	45
7. RC circuit of radiation monitor system	46
8. Growth of potential across the capacitor C of the RC circuit of Fig. 7	48
9. Sample holder assemblies, (a) for irradiation, (b) for counting	64
10. Electromagnetic energy analyzing system	70
11. Relation between mean electron kinetic energy and deviation current to the bending magnets of the energy analysis system of the Sagittaire accelerator	73
12. Linear accelerator modification	74
13. Intrinsic germanium photopeak efficiency	84
14. Radiation monitor system arrangement	87
15. Sample irradiation geometry	89

Figure	Page
16. Thick target parameters used in the bremsstrahlung computer program	95
17. Relative yields of the (γ ,n) reaction in the ^{19}F , ^{39}K , and ^{12}C isotopes	107
18. The (γ ,n) cross sections in ^{19}F , ^{39}K , and ^{12}C	108
19. K_2SiF_6 sample decay	110
20. Teflon sample decay	111
21. K_2SiF_6 photonuclear yield ratios	115
22. Teflon photonuclear yield ratios	116
23. Comparison of the O'Dell spectrum calculated in this work with the spectrum of Berger and Seltzer (51)	121
24. Comparison of the O'Dell spectrum calculated in this work with the spectrum of Ferdinande (53)	122
25. Comparison of the O'Dell spectrum calculated in this work with the experimental data of O'Dell (79)	124
26. Sagittaire photon I (flattened) and photon II 25 MeV spectra	125
27. Gaussian fit to the experimental points of the measurement of electron multiple scattering angle	128
28. Normalized yield of $^{27}\text{Al}(\gamma,2p)^{25}\text{Na}$ reactions	130
29. Comparison of the total energy in Schiff and thick target spectra	131
30. Schiff and thick target reduced yields	133
31. The $^{27}\text{Al}(\gamma,2p)^{25}\text{Na}$ cross section obtained with thick target bremsstrahlung spectra	134
32. The $^{27}\text{Al}(\gamma,2p)^{25}\text{Na}$ cross section reported by Hull and Whitehead (21)	136

Figure	Page
33. The $^{27}\text{Al}(\gamma, 2p)^{25}\text{Na}$ cross section obtained with Schiff bremsstrahlung spectra	138
34. 30 MeV Schiff and thick target spectra used in the cross section analyses	139
A1. Spherical Coordinates	155
A2. The square well (a) and harmonic oscillator (b) potentials	159
A3. Energy levels due to an infinite square well potential (a) and a harmonic oscillator potential (b)	161
A4. Harmonic oscillator energy levels with spin-orbit coupling	164
B1. Definition of quantities relevant to the discussion of nuclear electric multipoles	171
C1. Block diagram of linear accelerator	183

A STUDY OF THICK-TARGET X-RAY SPECTRA
USING PHOTONUCLEAR REACTIONS

CHAPTER I

INTRODUCTION

High-energy linear accelerators are becoming increasingly more popular in radiation therapy departments because of the augmented treatment flexibility they provide radiation oncologists. The depth-dose characteristics of the photon beams produced by these accelerators maximize the dose deliverable to treatment volumes located at substantial depths while minimizing the dose to overlying healthy tissues. In addition, the rapid fall-off of the depth dose of the electron beams they may provide permits treatment of tumors located at slight depths while sparing underlying structures. The nominal energies of many high-energy accelerators exceed the threshold energy for photonuclear reactions. Thus, the study of photonuclear reactions is becoming an increasingly more important part of the medical radiological sciences.

Photonuclear reactions have been applied in many different ways in medical radiation physics. The radioactivity induced in radiation therapy patients has been used to investigate the distribution of dose

in the irradiated volume (1,2). Photonuclear activation analysis has been employed to detect trace amounts of certain elements in biological materials (3,4). Photoactivation has been used to determine megavoltage x-ray spectra (5). Photonuclear reaction thresholds and cross-section resonances have been employed in the energy calibration of accelerators (6-8). Ratios of photoactivation yields in pairs of metallic foils have been used to specify x-ray quality (9,10). Photoactivation has been used also to produce clinically useful amounts of short-lived positron-emitting isotopes used in nuclear medicine (11,12).

The research reported here utilized photonuclear reactions to study the bremsstrahlung spectra produced by a high-energy clinical linear accelerator. The study consisted of essentially three parts. First, ratios of photonuclear yields that describe the distribution in energy of photons in an x-ray beam were investigated. Second, a numerical analysis computer calculation of thick-target bremsstrahlung spectra was made to simulate the spectra of x rays produced in a clinical linear accelerator. Third, the yield of the $^{27}\text{Al}(\gamma, 2p)^{25}\text{Na}$ reaction was measured and the cross section determined to investigate the feasibility of using thick-target spectra for cross-section determination and to report on resonance structure in the cross section which previously has been unreported.

Overview

This report has been divided into five chapters. In Chapter I each of the three parts of the research are introduced and the objectives of each part are set forth. In Chapter II the characteristics of photonuclear reactions are described, the measurement and analysis of photo-

nuclear yields is discussed, and the equations used in subsequent calculations are derived. Chapter III describes the materials used in the research and delineates the procedures followed in each part of the work. Chapter IV presents the results of each of the three parts of the research. In Chapter V the conclusions made from the results obtained are set forth.

Photonuclear Ratios

X-ray quality is a term essentially used to describe the distribution in energy of photons in a bremsstrahlung beam. A statement of quality is useful to predict the penetration of the beam, to calculate differential absorption in various materials, and to attempt to explain variations in biological effectiveness (13). The most complete specification of quality is provided by the spectral distribution of fluence, or energy fluence, as a function of photon energy. The energy spectrum, however, is extremely difficult to measure, thus quality is commonly expressed in terms of certain parameters which are more simply measured.

For a given waveform, the most obvious parameter which may be used to describe x-ray quality is the x-ray generator's accelerating potential. This potential determines the final energy of the electrons producing the x rays. The final electron energy is taken to correspond to the maximum energy of the photons in the x-ray spectrum and is thus termed the endpoint energy. The specification of the endpoint energy alone of a bremsstrahlung spectrum is not sufficient to characterize its spectral quality. X-ray beams having the same endpoint energy may have quite different energy characteristics depending upon the thickness of the bremsstrahlung target and upon the amount of additional filtration in the beam.

Parameters that describe the penetrating ability of an x-ray spectrum have been used for many years to further characterize spectral quality. The most prominent of these parameters is the Half Value Layer (HVL), the thickness of a material that will reduce the intensity of an x-ray beam to one-half the original intensity. The HVL is sensitive to not only the endpoint energy of the spectrum, but also to the amount of filtration in the beam. For many low-energy (< 1 MeV) applications, an appropriate specification of quality is provided by the two parameters endpoint energy and HVL (13). The quality of x-ray beams used in radiation therapy are often additionally specified in terms of depth dose in an absorber. The specification adopted may take the form of a complete depth-dose curve from the surface of the absorber to the depth at which the dose is reduced to a certain value, say 10%; or it may be restricted to the depth-dose at one or two selected depths.

Unfortunately, for x-ray energies in the megavoltage range, the parameters that describe x-ray penetration ability (HVL and depth-dose) are relatively insensitive to changes in quality. This is a result of the slow change in the attenuation coefficients of all materials with increasing photon energy above about 3 MeV. Neth and Schulz (14) have calculated the percent change in HVL per MeV in different materials for thin-target spectra of endpoint energies from 5-40 MeV. The authors found that in even the most sensitive material (water), the average sensitivity ($\Delta\text{HVL}/\Delta E$) was found to change less than 2% per MeV for endpoint energies between 10 and 40 MeV. The ratio of the percent depth dose in tissue at 10 cm depth to that at 2 cm depth changes by less than 2% of the mean per MeV for betatron x rays, 100 cm SSD, 10 x 10 cm field, from

15-35 MeV (15,16). The ratio of ionization measurements made at 5 cm depth and 15 cm depth in water changes by only approximately 0.5% of the mean when irradiated with 15 to 30 MeV x rays from linear accelerators (17).

It is thus apparent that a more sensitive index of megavolt. x radiation quality is required. Comparison of radiation therapy treatment regimes requires a complete specification of the characteristics of the radiation beams used. A sensitive index of quality would aid in deciding whether dosimetry data (such as percent depth-dose) for one x-ray generator would be applicable to another. Similarly, the suitability of energy-dependent factors necessary for dose computations, such as instrument calibration factors and absorbed dose conversion factors, could be established by comparing the spectral quality index of the calibration machine with that of the user's machine. A sensitive index could also be used as a quality control device to assess the stability of radiation therapy machines and signal equipment faults before they become obvious by other means. Additionally, if the detector used to obtain such an index were small enough, it would be possible to measure the variations in spectral quality at selected locations in irradiated media.

A sensitive index of x-ray quality in the megavoltage energy range is provided by the ratio of photonuclear yields in carefully selected materials. Photonuclear ratios are based on the fact that photonuclear reactions in most elements result in radioactive nuclei whose decay rate can be measured to determine photonuclear yields. If the elements are chosen such that the photonuclear cross sections peak at different locations in the photon energy spectrum, the ratio of the photonuclear yields

produced in each element will vary quite sensitively with energy. Photo-nuclear yield ratios for thin-target bremsstrahlung spectra from 15 to 40 MeV have been measured and published by Nath and Schulz (9). Their method involved counting the activity induced in each of a pair of metallic foils. Their experiment produced unique "Photoactivation Ratios" from about 25 to 35 MeV. The ratio of the photonuclear yield of the $^{89}\text{Y}(\gamma, 2n)^{87}\text{Y}$ reaction to the photonuclear yield of the $^{65}\text{Cu}(\gamma, n)^{64}\text{Cu}$ reaction yielded the most sensitive quality index as a function of photon energy in the 25-35 MeV range. The maximum sensitivity was approximately 25% per MeV, a definite improvement over the indices of quality previously mentioned.

The purpose of the first part of this work was to seek photo-nuclear yield ratios sensitive to x-ray spectra produced by thick targets in the 15 to 25 MeV energy range where such ratios are lacking. Many high-energy medical linear accelerators have nominal energies in this range. The materials were chosen such that the photonuclear reactions in the elements producing the yields used to compute the ratios resulted in radioactive nuclei that emitted the same energy gamma ray. This permits the determination of ratios without prior knowledge of the efficiency of the radioactivity counter. The samples consisted of chemical compounds which contained the pair of elements from which photonuclear yield ratios were computed. This further facilitates ratio determination in that self-absorption factors need not be determined.

The $^{27}\text{Al}(\gamma, 2p)^{25}\text{Na}$ Cross Section

Several techniques have been employed to determine photonuclear reaction cross sections from experimental data. The fundamental methods of photonuclear measurements have been summarized by Strsach (18) and

have been described in some detail by Bogdankevich and Nikoleev (19). Frequently, a photonuclear reaction results in the formation of a radioactive nucleus as a result of the nuclear transformations induced by the high-energy photons. The activity induced in a sample of material exposed to a flux of high-energy photons is directly related to the cross section of the particular photonuclear reaction producing the radioactive species and to the number and energy of the photons traversing the sample. By measuring the activity of the sample after irradiation, it is possible to obtain the cross section of the reaction.

Most commonly, the source of high-energy photons used in photonuclear research is the bremsstrahlung beam of either betatrons or linear accelerators. Bremsstrahlung beams possess a spectrum of photon energies ranging from essentially zero to the maximum kinetic energy, or endpoint energy, of the electrons producing the bremsstrahlung; thus, photonuclear reactions produced by bremsstrahlung x rays are induced by many photons in the energy spectrum. On the other hand, the number of bremsstrahlung-induced reactions at a given endpoint energy is related to the photonuclear cross section as a function of energy. If the reactions produced result in radioactive nuclei, then we may define a photonuclear yield at a given endpoint energy, proportional to the number of photonuclear reactions, which is determined from a measurement of the radioactivity induced. If the bremsstrahlung endpoint energy is varied and yield measurements are made at each endpoint energy, then a yield curve, a graphic representation of the photonuclear yield as a function of bremsstrahlung endpoint energy, may be constructed. If the bremsstrahlung spectrum is known, the photonuclear cross section as a function of energy may then be

extracted mathematically from the yield curve.

Implicit in the previous discussion is the dependence of the cross section obtained upon the mathematical model chosen to describe the bremsstrahlung spectrum. Photonuclear experiments performed in the past have employed the Schiff integrated-over-angle spectrum (20) to describe the photon energy distribution of the bremsstrahlung beam (18,19). The Schiff calculations were performed under the assumption that the electron interacts only once in the target, i.e., the target is infinitely thin. Thus, in a strict sense, the use of Schiff spectra is justified only in experiments utilizing thin bremsstrahlung targets. In an experiment where photonuclear reactions are produced by thick-target bremsstrahlung (as is the case in this experiment), the bremsstrahlung spectra must be corrected for the spectral distortions introduced by electron collisional losses as well as by photon attenuation processes. Only then can a realistic cross section be determined from such an experiment.

In the second portion of the research presented here, the $^{27}\text{Al}(\gamma,2p)^{25}\text{Na}$ reaction yield was measured in 0.25 MeV increments from threshold to 33 MeV and the reaction cross section was calculated. This cross section has never been determined with such energy resolution before although the cross section has been reported previously (21). The increased energy resolution of this experiment enables a more detailed examination of resonance structure in the cross section possibly indicating the existence of higher energy nuclear states.

The Bremsstrahlung Spectrum

Photonuclear cross sections deduced from measurements of yield depend to a very large degree on the bremsstrahlung spectrum utilized in

the analysis. The review of photonuclear literature conducted in preparation for this work conveyed the fact that thick-target bremsstrahlung spectra had never before been used in photonuclear reaction cross section determinations regardless of the target thickness used in the experiment. To examine the feasibility of using thick-target spectra for cross section determinations, in the third part of this research a numerical analysis computer calculation of thick-target bremsstrahlung spectra was performed and the spectra obtained were used to calculate the $^{27}\text{Al}(\gamma, 2p)^{25}\text{Na}$ reaction cross section. The cross section was also calculated using thin-target spectra to determine the effect of spectral shape on the cross section obtained.

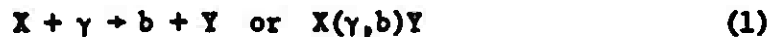
CHAPTER II

THEORY

Photonuclear Reactions

A photonuclear reaction, or nuclear photoeffect, is an electromagnetic interaction in which a photon is completely absorbed by a nucleus. The result is the emission of one or more nuclear constituents.

A reaction of this type may be represented by



where X is the target nucleus, γ represents the incoming photon, b is the emitted particle, and Y is the residual nucleus. Frequently the definition of a photonuclear reaction is restricted to include only those processes in which the emitted particles are either protons (γ, p), ($\gamma, 2p$), etc., neutrons (γ, n), ($\gamma, 2n$), etc., or aggregates of protons and neutrons (γ, np), ($\gamma, 2np$), (γ, α), etc. Thus photomeson production (γ, π) and nuclear resonance scattering (γ, γ') are excluded.

Photonuclear reactions are endoergic, that is, energy is required to initiate the reaction. The minimum amount of energy which can initiate the reaction is called the threshold energy. A photonuclear reaction is allowed energetically only when the photon energy equals or exceeds the reaction threshold energy. A photonuclear reaction's threshold energy

can be obtained from equations of energy and momentum conservation. For a reaction $X(\gamma, b)Y$, the threshold energy k_{\min} will be given by

$$k_{\min} = BE_b [1 + (BE_b / M_x c^2)] \quad (2)$$

where M_x is the mass of the target nucleus, c is the velocity of light, and BE_b , the binding energy of the emitted particle, is given by

$$BE_b = SE_b + E_y^* \quad (3)$$

where SE_b is the emitted particle's separation energy and E_y^* is the excitation energy of the residual nucleus. The separation energy SE_b may be calculated from the expression

$$SE_b = \Delta E_b + \Delta E_y - \Delta E_x \quad (4)$$

where ΔE_b , ΔE_y , and ΔE_x are called the mass decrements of the emitted particle, residual nucleus, and target nucleus, respectively. Typically, threshold energies of photonuclear reactions exceed 8 MeV.

The probability or relative frequency with which a photon of a determined energy will undergo a specific photonuclear absorption process in a certain absorber is indicated by that reaction's "cross section," σ ($\text{cm}^2/\text{nucleus}$). The cross section of the photonuclear reaction $X(\gamma, b)Y$ may be defined as the ratio of the number per sec of photons γ of energy k absorbed by the nucleus to the photon flux at that energy.

$$\sigma(k) = \frac{\# X(\gamma, b)Y \text{ reactions per sec resulting from the absorption of a photon of energy } k}{\# \text{ photons of energy } k \text{ per cm}^2 \text{ per sec.}} \quad (5)$$

Thus a particular photonuclear reaction will have a specific probability or cross section at a specific incident photon energy. The cross section has dimensions of length squared with the ad hoc unit of barns (1 barn = 10^{-24} cm²) being in common usage.

Above the threshold energy the cross section increases with increasing incident photon energy k for several MeV, reaches a maximum value, then decreases with further increases of photon energy. The shape of this rather broad peak is very characteristic of reactions of this type and is called the "giant resonance." Photon absorption in this region is almost exclusively by electric dipole interaction with only a small (6%) contribution by electric quadrupole transitions (22). These phenomena are further discussed subsequently in this section. The general characteristics of the giant resonance have been set forth by numerous authors, among them Strauch (18), Levinger (23), Wilkinson (24,25), and Hayward (26). In general the giant resonance may peak at about 0.1 barns within a region from 10 to 30 MeV with a full width at half maximum (Γ) of approximately 3-8 MeV (18,23,26). The energy E_m at which the cross section is a maximum is approximately 20 MeV for light elements (23,26). For heavy elements, E_m varies inversely with the element's mass number A , with dependences of $A^{-0.2}$ (23) and $A^{-0.3}$ (26) having been observed. The area under the $\sigma(k)$ curve, called the integrated cross section σ_{int} and given by

$$\sigma_{int} = \int \sigma(k) dk \quad (6)$$

is proportional to A with proportionality constant about 0.02 MeV-barns (23).

Goldhaber and Teller have explained the giant resonance in terms of a collective model of the nucleus (27). According to their explanation, the giant resonance excitation is one in which all protons collectively execute harmonic motion relative to all neutrons. The protons and neutrons may be regarded as two incompressible, interpenetrating fluids which oscillate back and forth relative to each other. The resonant frequency, and hence the quantum energy $\hbar\omega$, will depend on the nuclear size. Their calculations yield a resonance, the energy of which varies as $A^{-0.17}$, in rough accordance with experimental findings.

Although the collective model exactly exhausts the dipole sum rule (see section on Theories of Photonuclear Reactions) and has been moderately successful in predicting the experimentally observed trend of E_{res} as a function of A , it has its shortcomings. It has nothing to say about Γ , the width of the resonance, and provides no explanation for the anomalous emission of protons from heavy nuclei. The probability of this process is a factor of 10^4 times more common than one would expect when the energy of excitation is shared among all of the nucleons and when all have equal statistical probability of emission. In view of these difficulties it has been tempting to seek an alternative explanation. Such an explanation is afforded by the shell model.

Detailed inspection of the giant resonance of photonuclear reactions in light elements reveals cross section maxima and minima, or "structure," which imply increased photonuclear absorption at photon energies corresponding to excitation energies of particular nuclear states. This structure in the giant resonance is best explained in terms of allowed transitions between nucleon energy states which are obtained

through the independent particle or shell model of the nucleus. The shell model of nuclear structure is discussed in some detail in Appendix A. Allowed transitions between energy states are treated in Appendix B. In the next section photonuclear reaction theories will be discussed with particular emphasis on the independent particle model of nuclear structure. Throughout, existing theories are compared to available experimental findings.

Theories of Photonuclear Reactions

As described in Appendix B, transitions between states are proportional to the square of the transition matrix element. In the interaction of photons with bound electrons, as in the atomic photoeffect, the perturbation operator in the matrix element overlap integral is the electric dipole operator. The matrix element for electric dipole transitions M_{E1} is given by (28)

$$M_{E1} = im\omega_{ge} \int \psi_e^* \sum_i z_i \psi_g dt \quad (7)$$

where z is the component of the displacement along the electric vector of the electromagnetic field, $\omega_{ge} = E_e - E_g$ is the energy difference between the excited and ground states divided by \hbar , and $\sum_i z_i$ is the dipole moment of the atom found by summing the component of displacement over all electrons of the atom.

In the nuclear photoeffect, where photon interactions with protons and neutrons are treated, two major changes must be introduced:

1. An effective charge must be used of eN/A for protons, and $-eZ/A$ for neutrons, where A is the mass number, Z is the atomic number,

and $N = A - Z$ is the neutron number. The effective charge is introduced since the displacements of the nucleons should be measured from the nuclear center of mass.

2. The partly exchange (Majorana) character of the neutron-proton potential must be considered. Siegert's theorem states that exchange forces between neutrons and protons imply the existence of a current of charged particles (π mesons) between the nucleons. Thus, the complete calculation of the dipole matrix element should involve the sum of nucleon and π -meson currents.

Two methods have been used for theoretical calculations of the photon absorption cross section for nuclei. First, the dipole matrix element can be calculated for absorption of photons if explicit assumptions are made as to the ground state and excited state wave functions (for various energies). Second, use can be made of "sum-rules" in which transitions from the ground state are summed over all possible final states. This method involves knowledge only of the transition operators and of the wave function for the ground state. Since the ground state wave function is a solution of Schrodinger's equation and thus determines the potential, Schrodinger's equation could then in principle be solved for this potential for the wave functions of the various excited states. The first method is then used for calculations.

If the classical Thomas-Reiche-Kuhn (TRK) sum-rule for electric dipole absorption of photons by Z electrons in an atom is modified for the nuclear photoeffect by the two effects discussed above (the use of effective charges and the significance of Majorana exchange forces), an expression is obtained for the integrated cross section for electric

dipole absorption of photons by a nucleus of atomic number Z , mass number A , and neutron number N . This dipole absorption "sum-rule" is given by (22)

$$\sigma_{\text{int}} = \int \sigma(k) dk = 0.058 \frac{NZ}{A} (1 + 0.8X) \text{MeV-barns} \quad (8)$$

where X is the fraction of the neutron-proton force that has an exchange character. The upper limit of integration must be set at about the meson threshold since Siegert's theorem, on which the sum-rule is based, will be invalid beyond that (24). Values of X from 0.5 to 0.7 have been found from neutron-proton scattering experiments. The number 0.8 was calculated using a nuclear model of a degenerate Fermi gas; however, the value of σ_{int} is relatively independent of the nuclear model except for the value of the coefficient 0.8 and possible small terms (23).

The independent particle shell model (IPM) of the nucleus has been very successful in describing dipole transitions in light elements. Nuclear photoeffect calculations have been performed by various authors for harmonic oscillator, infinite square well and finite square well potentials (23). Wilkinson (24,25) has shown that essentially all of the dipole sum-rule is exhausted in transitions between the last filled shell levels to virtual shell levels in the continuum. Transitions from unfilled shells do not contribute appreciably. The most important transitions were found to be those between states whose principal quantum number and increase in orbital angular momentum is unity. In addition, his calculations showed that the strongest transitions are those between states of larger orbital angular momentum. The well-known angular momentum, parity, and isotopic spin selection rules (see Appendix B) are

assumed to hold. Since all shells below the uppermost filled shell are also filled, transitions between these states are forbidden by the Pauli exclusion principle and excitations between these shells can contribute no oscillator strength (transition probability) to the total sum; in the same way, downward transitions which contribute to the sum negatively are also forbidden. Thus, oscillator strength is "transferred upward" through the shells and the oscillator strength from the uppermost filled shell results from a collective absorption by all the nucleons in the shell with the excitation of one nucleon to the next allowable unfilled level (29). Wilkinson showed that the E1 transitions between last filled and virtual levels which are allowed by the selection rules are energetically clustered sufficiently close to blend into an apparent giant resonance. In addition, Wilkinson's IPM calculations have been able to account for a roughly correct oscillator strength and for reasonable resonance widths.

In spite of the success of Wilkinson's IPM calculations in explaining the nuclear photoeffect phenomena described above, the giant resonance energy E_m resulting from the calculations was too low. The problem was in his choice of a static potential whose depth was determined by nucleon binding energies of the nuclei treated (29). He suggested that use of a velocity-dependent shell model potential that does not commute with nucleon position and that considers a nucleon-reduced mass might result in increased estimates of E_m in better accord with experiments.

Further IPM calculations were performed by Elliott and Flowers (30), who calculated the energies and radiative widths for transitions

from the odd parity levels of ^{16}O , and by Brown and Bolsterli (31) and Brown, Castillejo and Evans (32) who considered the effect of particle-hole interactions on the E1 energy levels in the nuclear photoeffect. The calculations took into consideration spin-orbit coupling. When a nucleon is elevated by E1 photon absorption to a virtual shell level, a hole is left in the filled shell. Such holes can be treated in many ways like single particles in the shell. Since the process of hole formation is dipole, the excited particle and hole are strongly correlated in angle; that is, their angular momentum must be coupled to form a 1-state, assuming the original to be in a 0^+ state (see Appendices A and B). Because many particle-hole states can be formed and because these states are almost degenerate in energy, the particle-hole interaction can have a profound effect in redistributing dipole transition strength. The above authors' calculations using particle-hole interactions resulted in increased excitation energies, in better agreement with experimental results. Although a specific mixture of exchange forces (Majorana and Bartlett) was used, the general trend of levels obtained was found to be relatively insensitive to the exchange mixture chosen. The calculations indicated that the entire dipole oscillator strength will be exhausted at photon energies below 30 MeV. Figure 1 illustrates particle-hole transitions for the ^{16}O nucleus (29) showing the simple harmonic oscillator shell levels (a) with $\hbar\omega = 17$ MeV, and the same levels with spin-orbit coupling (b). The transitions predicted by Wilkinson are shown with vertical lines along with the transition energies.

Although the collective and the IPM models may seem very different, they make very similar predictions in many cases. Brink (33) has

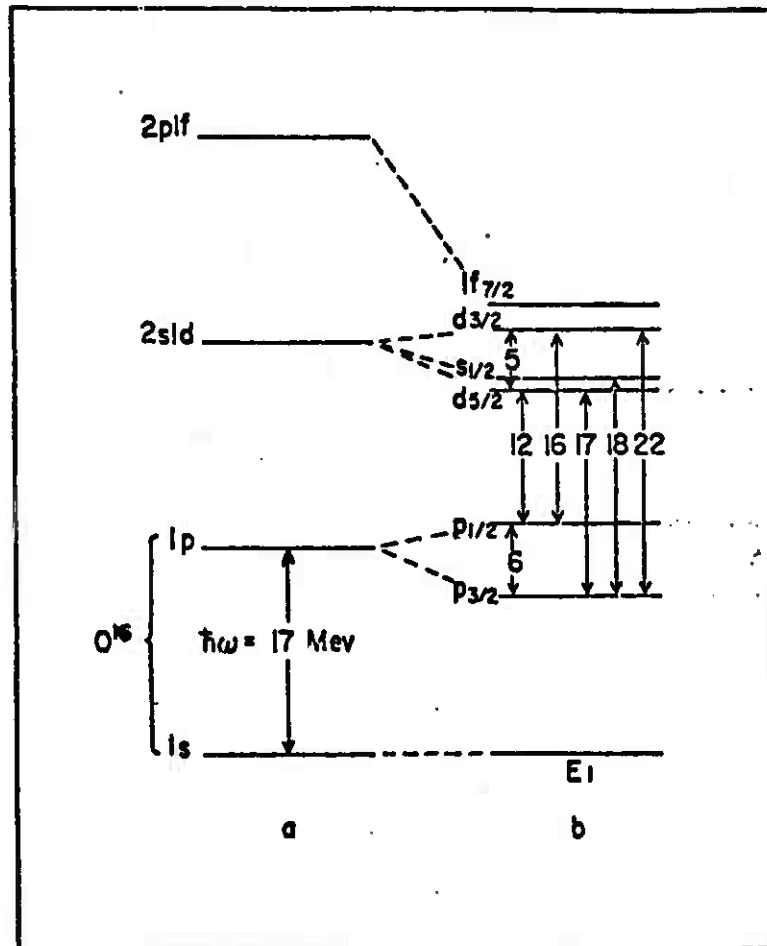


Figure 1. ^{16}O harmonic oscillator shell levels (a) and spin-orbit coupling levels (b). From Ref. (29).

demonstrated that the similarities probably are not accidental and that the two models are basically the same. The particle-hole or nucleon-nucleon correlations necessary to correct the independent particle model giant resonance predictions play an important collectivizing role in the theory. The pure IPM account has neglected the effects of interactions between the many superposed transitions. These interactions may very well be strong and the transitions may be pulled together by them to show a tighter grouping than expected by the raw IPM. It appears that introduction of nucleon-nucleon correlations into either model is necessary if the model is to describe anything more than the most gross feature of the photonuclear reaction cross section. A decision regarding the validity of one model or another is unimportant. Use is made of the model that yields the most accurate predictions.

Analysis and Solution of Photonuclear Yield Functions

Analysis

The calculation of cross sections from measured yield curves is the subject of this section. The analysis presented was formulated by Penfold and Leiss (34). In a photonuclear experiment a sample is exposed to a bremsstrahlung beam. The number of photonuclear reactions occurring within a sample depends upon the availability of target atoms, on the cross section for the particular reaction, and on the flux of photons incident upon the sample. The photon flux is measured by a calibrated ionization chamber which is irradiated simultaneously with the sample. A sample that contains n_t target nuclei per cm^2 is exposed to a beam of maximum energy T where $M(T,k)$ photons of energy between k and $k + dk$,

per unit range of k and per unit monitor response, enter the sample. If $\sigma(k)$ is the cross section in cm^2 per nucleus as a function of energy for the reaction under investigation, then the normalized yield of photonuclear reactions at a given bremsstrahlung endpoint energy per unit monitor response, $Y_n(T)$, is given by the integral

$$Y_n(T) = n_t \int_0^T M(T,k) \sigma(k) dk \quad (9)$$

The integral equation of Eq. (9) is called the photonuclear yield function. Repeated measurements of yield at different bremsstrahlung endpoint energies and a knowledge of the bremsstrahlung spectrum allow deduction of the cross section.

The photonuclear yield function, or simply photonuclear yield, may be thought of as an overlap integral as shown in Figure 2. The amount of yield $Y(T)$ will depend upon the degree to which the endpoint energy T of the bremsstrahlung spectrum $M(T,k)$ exceeds the threshold energy E_{th} of the photonuclear cross section $\sigma(k)$. In addition, the amount of yield depends on the relative shapes of the functions $M(T,k)$ and $\sigma(k)$.

The spectrum $M(T,k)$ is the bremsstrahlung photon flux that enters the sample per unit monitor response. This spectrum is the product of three factors:

- 1) An intrinsic bremsstrahlung spectrum function $\phi(T,k)$, which describes the x-ray spectrum emitted by a "thin" bremsstrahlung radiator. $\phi(T,k)$ is proportional to the bremsstrahlung cross section.
- 2) A spectrum modification function $f_s(k)$, which describes the

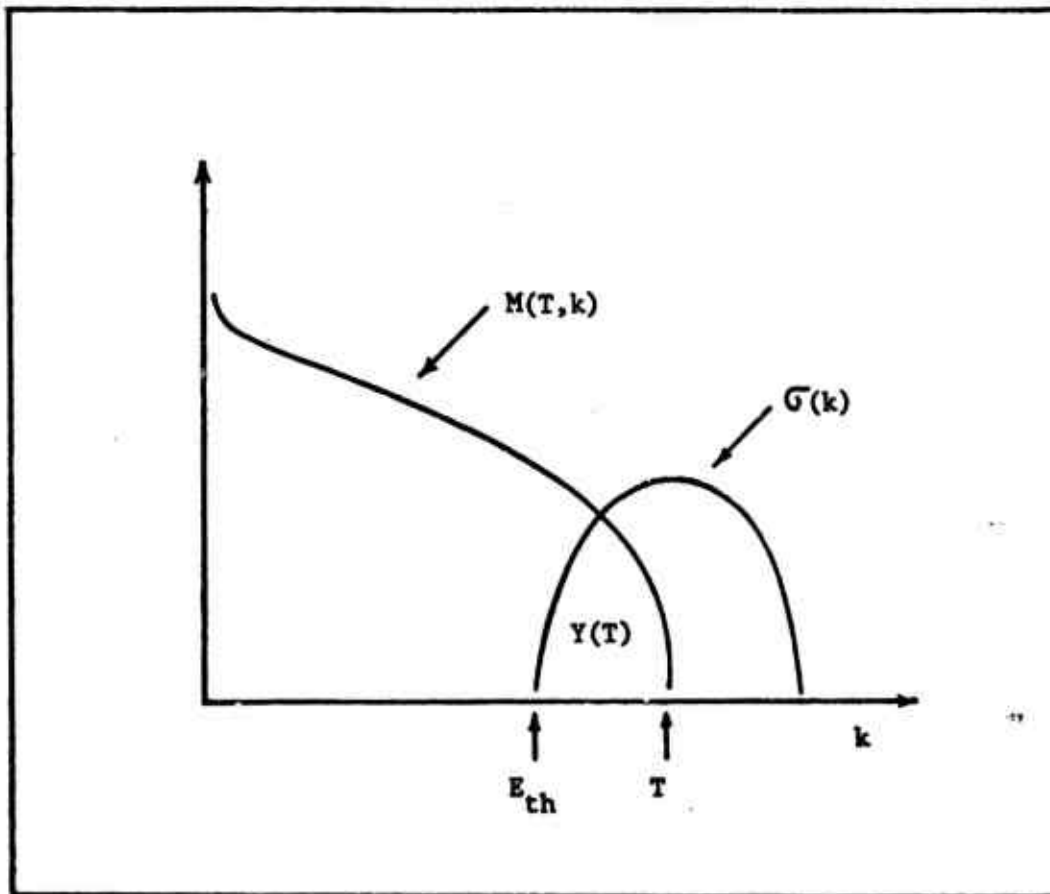


Figure 2. Photonuclear yield as an overlap integral.

deformation of the thin-target spectrum. The function of $f_s(k)$ accounts for the spectral distortion caused by electron collisional losses and by the attenuation of photons in the radiator and in structures which may be located in the beam between the radiator and the sample.

3) A monitor response function $F(T)$, which normalizes the spectrum that enters the sample-to-unit monitor response.

In view of the above, the spectrum $M(T,k)$ of Eq. (9) may be expressed as

$$M(T,k) = \frac{\phi(T,k)f_s(k)}{F(T)} = \frac{N(T,k)}{F(T)} \quad (10)$$

where $N(T,k)$ is the actual bremsstrahlung spectrum to which the sample is exposed. The spectrum $N(T,k)$ can be estimated by a numerical method. For the purpose of the present discussion it is assumed that $N(T,k)$ is known. The characteristics of this spectrum and the details of the numerical method used for its estimation are presented in a thorough fashion in the next section of this chapter (The Bremsstrahlung Spectrum).

In an analogous fashion one may define a spectrum function $M_m(T,k)$ which describes the photon flux entering the monitor chamber per unit monitor response. If the geometry of the experimental setup is such that the photon spectrum entering the monitor has first traversed the sample, then a spectrum distortion function $f_m(k)$ may be defined which describes the degradation of the bremsstrahlung spectrum $N(T,k)$ by photon absorption in the sample. Similarly to Eq. (10), $M_m(T,k)$ is

$$M_m(T,k) = \frac{N(T,k)f_m(k)}{F(T)} \quad (11)$$

The monitor response function $F(T)$ normalizes the spectrum incident on the monitor, $[N(T,k)f_m(k)]$, to unit response of the monitor. In other words, $F(T)$ gives the total number of photons in the bremsstrahlung spectrum that yields a unit count in the calibrated ionization chamber. $F(T)$ is defined as

$$F(T) = R(T) \int_0^T f_m(k)kN(T,k)dk \quad (12)$$

where $R(T)$ is the calibration factor of the monitor in units of response per unit incident energy. If the monitor and sample do not subtend identical solid angles and if the irradiation geometry is not perfectly reproducible between measurements of yield for different bremsstrahlung endpoint energies, an additional factor $\omega_m(T)/\omega_s(T)$ must be introduced into Eq. (12). This factor is a ratio of the angular distribution of the radiation integrated over the monitor solid angle to that integrated over the sample solid angle.

The spectrum distortion function $f_m(k)$ describes the photon attenuation due to interaction processes in the sample. At the high photon energies employed in photonuclear measurements, the predominant interaction processes are pair production and Compton scattering. The cross sections for these reactions at high photon energies vary very little as a function of energy. Therefore, the function $f_m(k)$ will not distort the spectrum's shape but will only reduce its intensity by a constant amount. One can then remove the function $f_m(k)$ from the integral and replace it by $f_t(T)$, a transmission factor as a function of bremsstrahlung endpoint energy which represents the fraction of the pho-

tons incident on the sample that are transmitted through the sample. In view of the above, the monitor response function $F(T)$ is now

$$F(T) = R(T)f_t(T)E(T) \quad (13)$$

where

$$E(T) = \int_0^T kN(T,k)dk \quad (13a)$$

is the total energy in the bremsstrahlung spectrum of endpoint energy T .

A solution to the photonuclear yield function, Eq. (9), may now be considered since the spectrum $M(T,k)$ has been defined through Eqs. (10) and (13). The photonuclear yield function now has the form

$$Y_n(T) = \frac{n_t}{F(T)} \int_0^T N(T,k)\sigma(k)dk \quad (14)$$

Here, the spectrum $N(T,k)$ is the actual bremsstrahlung spectrum seen by the sample. The monitor response function $F(T)$, which is defined by Eq. (13), has been removed from the integral because it does not vary as a function of the photon energy k . The remaining variables of Eq. (14) maintain their previous definitions.

The photonuclear yield function as given by Eq. (14) is dependent upon experimental conditions, in particular upon the radiation monitor used. Equation (14) may be rearranged into a form which is independent of the exact nature of the experimental arrangement. This rearranged form has been called the reduced yield function by Penfold and Leiss (34). The reduced yield $Y_r(T)$ may be defined as the photonuclear yield (number of photonuclear reactions) per target atom per cm^2 .

It is obtained by multiplying the normalized yield (number of photonuclear reactions per unit monitor response) $Y_n(T)$ times the monitor response function, $F(T)$, and then dividing the product by n_t , the number of target atoms per cm^2

$$Y_r(T) = \frac{Y_n(T)F(T)}{n_t} . \quad (15)$$

Using the above definition, the reduced photonuclear yield function is

$$Y_r(T) = \int_0^T N(T,k)o(k)dk . \quad (16)$$

It is to the reduced yield function $Y_r(T)$ that solutions are obtained. Note that the reduced yield $Y_r(T)$ is related to the experimentally determined normalized yield $Y_n(T)$ through Eq. (15) and that the monitor response function $F(T)$ can be obtained with Eq. (13).

Solutions

The solutions of the reduced yield function may be of two types:

1) solution of the integral equation directly or 2) solution of a set of linear equations which approximate the integral equation. $Y_r(T)$ is not known as a continuous function of endpoint energy T ; it is known only at a finite set of energies, T_1 . In practice, the yields $Y(T_1)$ are measured at n endpoint energies T_1 spaced in equal intervals ΔT . Therefore, a condition implicit in the solution of the integral equation, namely that the yield $Y_r(T)$ be known as a continuous function of energy, is not satisfied. Thus, the solutions sought here will be of the second type, solutions of linear equations which approximate the integral.

The reduced yield function can be replaced by a set of linear equations if a "step-wise" approximation to the bremsstrahlung spectrum is made, as shown in Figure 3. Let N'_{ij} be the number of photons in a bremsstrahlung spectrum $N(T_i, k)$ of endpoint energy T_i that possess energies between $k_j - \Delta T$ and k_j where ΔT (also called an energy bin) is a photon energy interval equal to the spacing of yield points on the yield curve.

$$N'_{ij} = \frac{1}{\Delta T} \int_{k_j - \Delta T}^{k_j} N(T, k) dk. \quad (17)$$

Each N'_{ij} depends on the relative position of the photon energy interval within the bremsstrahlung spectrum k_j : $j = 1, 2, \dots, i$, and on the endpoint energy of the spectrum T_i : $i = 1, 2, \dots, n$. The N'_{ij} can be calculated from functional approximations to the spectrum $N(T, k)$ (see next section).

In view of the above "step-wise" approximation, the reduced yield function becomes

$$Y(T_i) = \sum_{j=1}^i N'_{ij} \sigma_j; \quad i = 1, \dots, n \quad (18)$$

where

$$N_{ij} = N'_{ij} \Delta T \quad (18a)$$

and

$$\sigma_j = \frac{1}{\Delta T} \int_{k_j - \Delta T}^{k_j} o(k) dk \quad (18b)$$

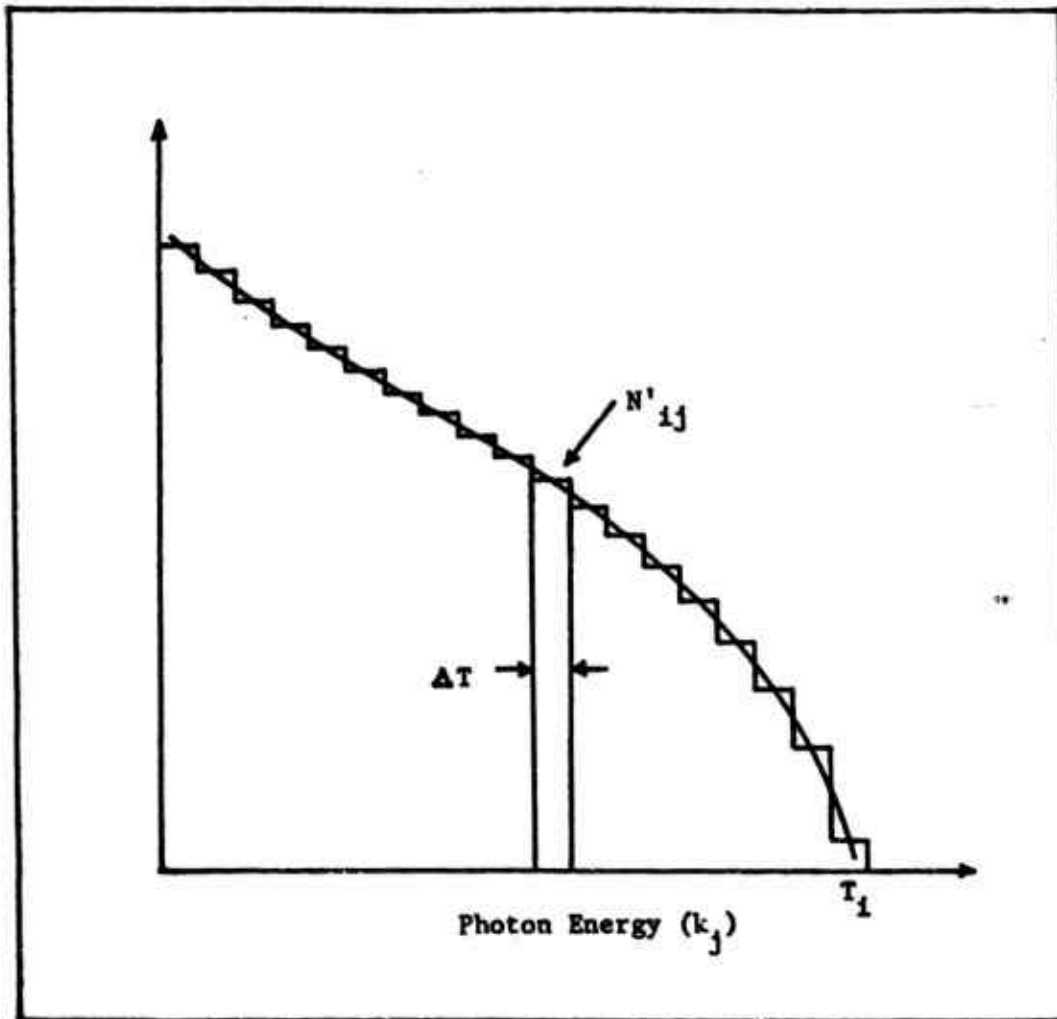


Figure 3. A "stepwise" approximation to the bremsstrahlung spectrum of endpoint T_1 .

is an average value of $\sigma(k)$ in the photon energy bin between $k_j - \Delta T$ and k_j . Note in Eq. (18) that the yield $Y(T)$ is the reduced yield $Y_r(T)$ of Eq. (16).

In matrix notation, Eq. (18) becomes

$$\vec{Y} = N\vec{\sigma} \quad (19)$$

where \vec{Y} is a column matrix with n rows of elements Y_j , $\vec{\sigma}$ is a column matrix with n rows of elements σ_j , and N is an n^{th} order triangular matrix with elements N_{ij} , $N_{ij} = 0$ when $j > i$. The matrix equation, Eq. (19), can be rewritten as

$$\begin{bmatrix} Y_1 \\ Y_2 \\ \cdot \\ \cdot \\ \cdot \\ Y_n \end{bmatrix} = \begin{bmatrix} N_{11} & 0 & 0 & \dots & 0 \\ N_{21} & N_{22} & 0 & \dots & 0 \\ \cdot & \cdot & \cdot & \cdot & \cdot \\ \cdot & \cdot & \cdot & \cdot & \cdot \\ \cdot & \cdot & \cdot & \cdot & \cdot \\ N_{n1} & N_{n2} & N_{n3} & \dots & N_{nn} \end{bmatrix} \begin{bmatrix} \sigma_1 \\ \sigma_2 \\ \cdot \\ \cdot \\ \cdot \\ \sigma_n \end{bmatrix} \quad (20)$$

Three methods of solution to the above set of equations have been proposed. The first method is the "Photon Difference Method" of Katz and Cameron (35). This method consists of solving the first equation for σ_1 , which when substituted in the second equation gives σ_2 , and so on. The worst defect of the photon difference method is the dependence of the calculated value of the cross section at a given energy on the results of calculations at all preceding energies. The errors arising from fluctuations in the yield curves at low energy are thus cumulated and transmitted to all cross sections at higher energies.

The second method is the "Matrix Inversion Method" of Penfold and Leiss (34). This method involves an inversion of the N matrix to obtain an inverse operator N^{-1} , which when applied to Eq. (19) yields the solutions σ_j

$$N^{-1}Y = N^{-1}N\sigma \quad (21)$$

The matrix N^{-1} consists of an appropriate set of what Penfold and Leiss called "B-numbers" that were calculated from Schiff spectra approximations. The matrix product $N^{-1}N$ represents a series of "weighting functions" that relate the solution $N^{-1}Y$ to the actual cross section. Penfold and Leiss have calculated sets of B-numbers and their associated weighting functions for thin-target bremsstrahlung of endpoint energies in the range from 2 MeV to 1 BeV (19,34).

The Penfold and Leiss method has been found to be extremely sensitive to the precision with which yields are measured. Moderate uncertainties in yield measurement may appear as photonuclear resonances often resulting in cross sections which oscillate excessively as a function of energy and are therefore physically unacceptable (36,37). A third method of photonuclear yield function analysis was developed by Cook (36) which minimizes the undulation, or structure, of the cross section function. The method has been called the "Least Structure Solution" of photonuclear yield functions.

The least structure method is basically a systematic smoothing technique which produces the most uniform set of cross sections consistent with the experimental data. The method applies all smoothing to the cross sections σ_j and not the yields Y_j , and it assumes no functional

form of the σ_j . Completely numerical methods are used. The amount of smoothing employed is determined by the variability of the input data and the distortions introduced by the smoothing can be estimated.

Cook's least structure solution of Eq. (19) selects those calculated values of o_j such that

$$\sum_j N_{ij} o_j \approx Y_i . \quad (22)$$

In other words, a solution o_j is acceptable if the calculated yield, $\hat{Y}_i = N_{ij} o_j$, is within an "acceptable range" of the measured yield Y_i at each endpoint energy T_i . A set of o_j 's are considered to be an acceptable solution if

$$\chi^2(o_j) = \sum_{i=1}^n \left[\frac{(\sum N_{ij} o_j - Y_i)^2}{(\Delta Y_i)^2} \right] \leq n \quad (23)$$

where $\chi^2(o_j)$ is a function closely related to the Chi-square distribution of statistics, the ΔY_i are standard deviations of the measured yield at each endpoint energy, and n is the number of data points on the yield curve.

The actual acceptable solutions, o_j , are arrived at by an iterative procedure. The procedure consists of determining the matrix M^{-1} such that [see Eq. (21)]

$$M^{-1} \vec{Y} = M^{-1} \vec{N} \vec{O} = \vec{R} \vec{O} \quad (24)$$

yields the acceptable set of solutions as determined by Eq. (23). The matrix M^{-1} is determined by calculus of variations techniques (38) and

is a function of: the bremsstrahlung matrix N ; the inverse of the bremsstrahlung matrix N^{-1} ; a smoothing matrix S which minimizes the difference between successive values of σ_j ; and a weighting matrix W of weighting factors inversely proportional to the variance of the yield points. The matrix product $M^{-1}N$ has been called the resolution function R . It can be thought of as an averaging of σ over a few energy bins with an approximate Gaussian function weighting (36).

A rigorous explanation of the Least Structure (LS) method for the solution of photonuclear yield functions is beyond the scope of this work. Such an explanation is available in references (29,36,37). However, because LS was used to determine the $^{27}\text{Al}(\gamma,2p)^{25}\text{Na}$ cross section, which was investigated in this work, a general explanation of the LS computational procedure is provided. The explanation is basically a description of a Fortran computer program which incorporates LS and which was devised by Cook (36).

Least Structure attempts to arrive at solutions σ_j to the photonuclear yield function [Eqs. (18) and (19)]

$$\vec{Y}_1 = \sum_j N_{1j} \vec{\sigma}_j \quad (25)$$

This is accomplished by calculating a matrix M (to be defined shortly) such that

$$\vec{Y}_1 = \sum_j M_{1j} \vec{\sigma}_j \quad (26)$$

yields solutions σ_j that do not oscillate as do those obtained by simply inverting the N matrix of Eq. (25). The matrix M is of the form

$$M_{ij} = N_{ij} + \lambda N_{ji}^{-1} W_i^{-1} S \quad (27)$$

where λ is a Lagrangian multiplier, N_{ji}^{-1} is the inverse of the transpose of the N_{ij} (bremsstrahlung) matrix, W_i^{-1} is the inverse of the weighting matrix $W_i = 1/(\sigma Y_i)^2$ where the σY_i are the standard deviations of the measured yields, and S is a smoothing matrix of the form

$$S = \sum_{j=2}^{n-1} (\sigma_{j+1} - 2\sigma_j + \sigma_{j-1})^2. \quad (28)$$

The matrix S (also called the structure function) is essentially a measure of the rate of change of the slope of the cross section as a function of endpoint energy. The LS solution to Eq. (25) is that set of σ_j which minimizes the structure function with the restriction that [see also Eq. (23)]

$$\chi^2 = \sum_{i=1}^n W_i (\sum N_{ij} \sigma_j - Y_i)^2 \leq n. \quad (29)$$

In the LS computer program, the Lagrangian multiplier λ is arbitrarily chosen as an input parameter. The equation

$$\vec{Y}_i = [N_{ij} + \lambda N_{ji}^{-1} W_i^{-1} S] \sigma_j \quad (30)$$

is then solved for the fixed λ . The solutions σ_j are substituted into Eq. (29) and χ^2 is computed. The calculated χ^2 is compared to an input χ_{in}^2 and an acceptable error $\Delta \chi_{in}^2$. If the solution is not acceptable, a new λ is selected and new solutions are obtained until both Eqs. (29) and (30) are satisfied.

The effectiveness of the least structure solution of photonuclear yield functions for cross section determination has been well proven and documented in the literature (37,39,40). Cook (37) and Anderson (39) measured the cross section for the ^{16}O photoneutron reaction, a reaction which has been extensively studied both experimentally and theoretically, using the least structure method and obtained results which were in very good agreement with existing theories and with results obtained by other investigators. The soundness of the technique was further verified by Cook (40) when he measured the cross section for the ^{12}C photoneutron reaction obtaining results consistent with those previously reported. The least structure method has been utilized since on several occasions for photonuclear reaction cross section determination (41-43).

The Bremsstrahlung Spectrum

This section describes the bremsstrahlung process and bremsstrahlung spectra. The theoretical calculations of the bremsstrahlung cross section are discussed in general with particular emphasis placed upon calculations performed in the Born approximation. Finally, the processes that lead to differences in bremsstrahlung spectra from thin and thick targets are described.

Bremsstrahlung is electromagnetic radiation which is produced when a charged particle is accelerated in the field of a charged particle. Bremsstrahlung as used here describes the electromagnetic radiation emitted by electrons decelerated upon their penetration into a bremsstrahlung radiator or target. The bremsstrahlung process is depicted schematically in Figure 4. An electron of charge e^- and kinetic energy T comes within the Coulomb field of a nucleus of charge $+Ze$ where it is

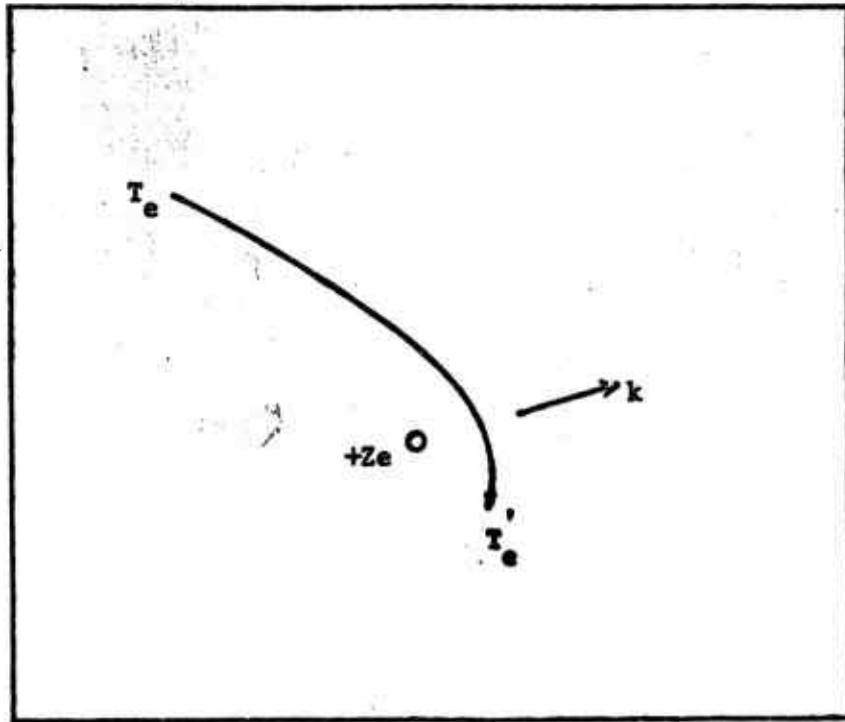


Figure 4. The bremsstrahlung process.

deflected producing a photon of energy k . The energy k of the photon is the difference between the electron's initial kinetic energy T and its final kinetic energy T' .

$$k = T - T' \quad (31)$$

Because the deflected electron can have any one of an essentially infinite number of kinetic energies between 0 and T , the photon may possess any energy up to T .

A classical electrodynamics formulation may be used to obtain an approximate functional form for the energy spectrum of the photon

$$N(k) = N_a \frac{d\sigma(k)}{dk} \quad (32)$$

where $N(k)$ is the number of photons of energy between k and $k + dk$, N_a is the number of target nuclei per cm^2 , and $d\sigma(k)/dk$ is the differential cross section for bremsstrahlung production in cm^2 . The bremsstrahlung cross section describes the relative probability with which the bremsstrahlung process will occur. A simplified expression for the bremsstrahlung cross section has the form (44)

$$\frac{d\sigma(k)}{dk} = Z^2 r_0^2 \alpha \phi(T, Z, k) / k \quad (33)$$

where Z is the atomic number of the target element, r_0 is the classical electron radius, α is the fine structure constant and $\phi(T, Z, k)$ is the so-called intensity function. From Eqs. (32) and (33) it is evident that for a given target the bremsstrahlung spectrum is inversely proportional to the energy of the emitted photon. Also seen is the direct relation-

ship between the photon's energy spectrum and the intensity function $\phi(T, Z, k)$.

An accurate expression for $\phi(T, Z, k)$ at large T and k has not been obtained classically. To describe $\phi(T, Z, k)$ fully, quantum electrodynamics is required. A most general quantum-mechanical analysis provides the following approximate expression for the bremsstrahlung cross section (19)

$$\frac{d\sigma(k)}{dk} \approx \frac{Q_f |H_{if}|^2}{p_0 c / E_0} \quad (34)$$

where Q_f is the density of final states, p_0 is the initial electron momentum, c is the speed of light in vacuo, E_0 is the total initial energy of the electron, and H_{if} is the matrix element for the transition from the initial state i to the final state f . From Eq. (34) it is seen that the bremsstrahlung cross section depends upon the square of the absolute value of the transition matrix element. This dependence is implicit in the intensity function of Eq. (33). The transition matrix element in turn depends upon the wave functions of the electron initial and final states.

To obtain an exact expression for the bremsstrahlung cross section it is essential to know the exact wave functions that describe the electron in the Coulomb field of the nucleus. However, the Dirac wave equation for an electron in a Coulomb field does not have finite solutions because the wave function in this case yields an infinite series (19,45,46). Thus, approximate wave functions must be used to calculate the transition matrix elements. In addition, some simplifying assumptions must be made in the calculations themselves. Therefore,

only approximations to the bremsstrahlung cross sections are obtainable.

Basically, the approximations made in the calculation of the bremsstrahlung cross section fall into one of two categories: 1) calculations performed in the Born approximation, and 2) extreme relativistic calculations. In the Born approximation calculations, the Coulomb field is considered a first-order perturbation of the electron initial state. The electron initial and final wave functions are described as plane waves (51,52). Extreme relativistic calculations (45,49) essentially encompass the calculations that do not use the Born approximation. In extreme relativistic calculations, Sommerfeld-Maue wave functions in a screened (atomic electrons "screen" the nuclear charge) Coulomb potential are used. These wave functions are described as plane and spherical waves (45). It turns out that extreme relativistic calculations are valid only for initial electron kinetic energies exceeding about 50 MeV (19). For this reason, and due to the fact that energies of interest here are well below that value, extreme relativistic calculations are not considered further in this treatment; Born approximation calculations are, hence, emphasized.

The Born condition restricts the atomic number of the target element and the electron initial and final velocities such that

$$2\pi Z/137\beta \ll 1 \quad (35)$$

where $\beta = v/c$ where v is the electron's velocity and c is the speed of light. It is evident that the conditions of the Born approximation are not strictly met for high Z targets such as those made of tungsten ($Z = 74$). In addition, the theory fails at the high-energy end of the spectrum

(the so-called tip) when the energy of the emitted photon approaches the kinetic energy of the incident electron and the velocity of the recoil electron is small compared to the speed of light. However, the use of the Born approximation formulas predict bremsstrahlung spectra which agree reasonably well with experiment (19,46).

The most important contributions to bremsstrahlung cross section formulations obtained within the framework of the Born approximation are due to Bethe and Heitler (47), Heitler (48) and Schiff (20). Bethe and Heitler obtained an expression for the bremsstrahlung cross section which is differential in electron angle and in photon angle and energy. Their expression was derived on the assumption that the field of the nucleus is a pure Coulomb field, i.e., no nuclear screening by atomic electrons was considered. Nuclear screening is an important parameter which must be taken into consideration, particularly in the case of bremsstrahlung spectra from high Z targets. Schiff integrated the Bethe-Heitler differential cross section assuming complete screening (20). The expressions he obtained apparently show the best agreement with available experimental data (19,46,50). The Schiff expressions have been widely used in the analysis of experimental results obtained with bremsstrahlung spectra from high-energy accelerators.

In his calculations, Schiff started with the Bethe-Heitler cross section and integrated it assuming that: 1) the initial and final energies of the electron are large compared to its rest energy; 2) the Coulomb field of the atom may be represented by the potential $(Ze/r)e^{-r/a}$ where $a \approx Z^{1/3}$ (Thomas-Fermi model); 3) terms of the order of $(Z^{1/3}/c)^2$ may be neglected. Under these assumptions he obtained the following

expression for the bremsstrahlung cross section differential in photon emission angle and energy

$$\frac{d\sigma(k,x)}{dkdx} = \frac{4Z^2}{137} r_0^2 \frac{dk}{k} x dx \left\{ \frac{16x^2 E}{(x^2 + 1)^4} - \frac{(E_0 + E)^2}{(x^2 + 1)^2 E_0^2} + \left[\frac{E_0^2 + E^2}{(x^2 + 1)^2 E_0^2} - \frac{4x^2 E}{(x^2 + 1)^4 E_0} \right] \ln M(x) \right\}, \quad (36)$$

whers

$$\frac{1}{M(x)} = \left(\frac{uk}{2E_0 E} \right)^2 + \left(\frac{Z^{1/3}}{111(x^2 + 1)} \right)^2 \quad (36a)$$

and

$$x = E_0 \Phi / u. \quad (36b)$$

In Eqs. (36), E_0 is the initial total electron energy, E is the final total electron energy, $k (= E_0 - E)$ is the energy of the radiated photon, Z is the atomic number of the target element, r_0 is the classical electron radius, u is the rest energy of the electron, and x is the reduced angle of emission of the radiated photon which is a function of the angle Φ , in radians, at which the photon is radiated with respect to the initial electron direction. The use of the atomic Thomas-Fermi model in considering the effects of screening lead to exaggerated values of $d\sigma(k,x)$, but the error introduced does not exceed 4% in the worst case when Z is large and screening is intermediate (19,20,46).

Thick-Target Bremsstrahlung Spectra

The arguments previously presented considered only bremsstrahlung

spectra from "thin" targets. A thin target is a bremsstrahlung radiator of thickness such that only one electron interaction occurs. The shape of the thin-target spectrum reflects the transition probabilities between the electron initial and final states. Most all linear accelerators possess "thick" targets because of the substantially larger photon fluences attainable. A thick target is a radiator of thickness such that many electron interactions occur. Such interactions include collisional as well as radiational interactions. The radiated photons can also interact within the target. Thus, in the thick-target situation, the shape of the bremsstrahlung spectrum additionally reflects the deformation of the thin-target spectrum due to the interactions in the target of the electrons and photons. The difference in spectral shape between bremsstrahlung produced in thin targets in contrast to that produced in thick targets is schematically represented in Figure 5.

Thick-target bremsstrahlung spectra calculations in the energy range from about 1 MeV to about 50 MeV have been performed by essentially two methods: 1) by Monte Carlo calculations such as those of Berger and Seltzer (51), and 2) by numerical analysis methods such as those employed by Lent and Dickinson (52) and by Ferdinand and co-workers (53). In the present work, a numerical analysis method similar in many respects to that of Ferdinand was used to estimate the bremsstrahlung spectra of the linear accelerator which was used. The approach is based on Hisdal's (54) method of correcting intermediate target spectra for the effects due to electron multiple scattering. The Molière (55) multiple scattering distribution is assumed. The method is described in detail in the Bremsstrahlung Spectrum section of Chapter III - Materials and Methods.

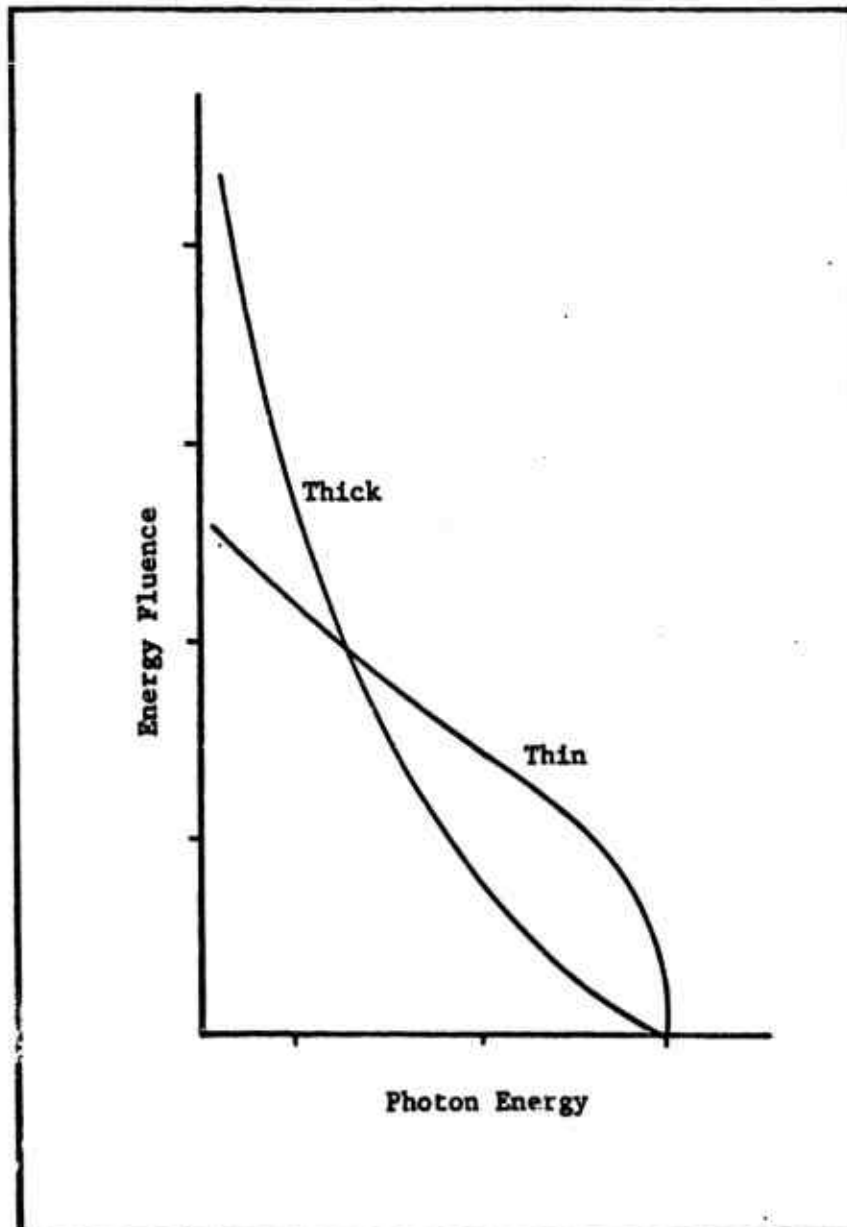


Figure 5. Bremsstrahlung spectra from thin and thick targets. Curves have been normalized to equal areas.

Measurement of Photonuclear Yield

The solution of the photonuclear yield function requires that the reduced yield $Y_r(T)$, photonuclear reactions at a certain bremsstrahlung endpoint energy T per target atom per cm^2 , be determined. This is accomplished by measuring the normalized yield $Y_n(T)$, the number of photonuclear reactions per unit monitor response, multiplying the normalized yield by the monitor response function of Eq. (13), $F(T)$, and dividing this product by n_t , the number of target atoms per cm^2 in the sample. The normalized yield $Y_n(T)$ is obtained experimentally. If photonuclear reactions produced in a sample result in radioactive nuclei, then the number of such reactions is simply a function of the radioactivity induced in the sample. If a radiation monitor, such as an ionization chamber, is irradiated simultaneously with the sample such that its response is directly proportional to the bremsstrahlung beam energy flux, then the normalized yield $Y_n(T)$ can be obtained from a measurement of the sample activity and from the monitor response. This section describes the methodology by which the normalized yield is determined.

The normalized yield $Y_n(T)$ is the quotient of two quantities which are each determined experimentally.

$$Y_n(T) = N_o(T)/V_o(T) \quad (37)$$

In Eq. (37), $N_o(T)$ is the total number of photonuclear reactions induced in the sample at a given bremsstrahlung endpoint energy, and $V_o(T)$ is a radiation monitor response which is proportional to the bremsstrahlung beam energy flux at a given endpoint energy. $N_o(T)$ is determined from a measurement of the sample activity. $V_o(T)$ is determined from the

response of a monitor system which will be described shortly.

The total number N_0 of photonuclear reactions induced may be expressed as the product of the photonuclear reaction production rate P_N and the irradiation time t_r

$$N_0 = P_N t_r. \quad (38)$$

If the reactions result in radioactive nuclei of decay constant λ , then the number $N(t)$ of radioactive nuclei present in the sample at any given time t is related to the constant production rate P_N through the expression

$$N(t) = \frac{1}{\lambda} P_N [1 - \exp(-\lambda t)]. \quad (39)$$

The relationship of Eq. (39) is shown in Figure 6. The number of radioactive nuclei "grows" with a $1 - \exp(-\lambda t)$ dependence with P_N/λ as an upper limit. Solving Eq. (39) for P_N and substituting the resulting expression in Eq. (38) results in the following equation for $N_0(T)$ in terms of $N(t)$

$$N_0(T) = N(t) \lambda t_r / [1 - \exp(-\lambda t)]. \quad (40)$$

The number of radioactive nuclei at any given time, $N(t)$, is rather sensitive to fluctuations in the production rate, which may be caused by variations in bremsstrahlung beam intensity. For this reason, it is desirable that the radiation monitor respond in time to the beam intensity in the same fashion as does $N(t)$. To this purpose, the output of the bremsstrahlung monitor, an NBS type P2 ionization chamber (56), is delivered to an RC electric circuit as shown in Figure 7 (57). The response $V(t)$ of a circuit of this type as a function of time is shown

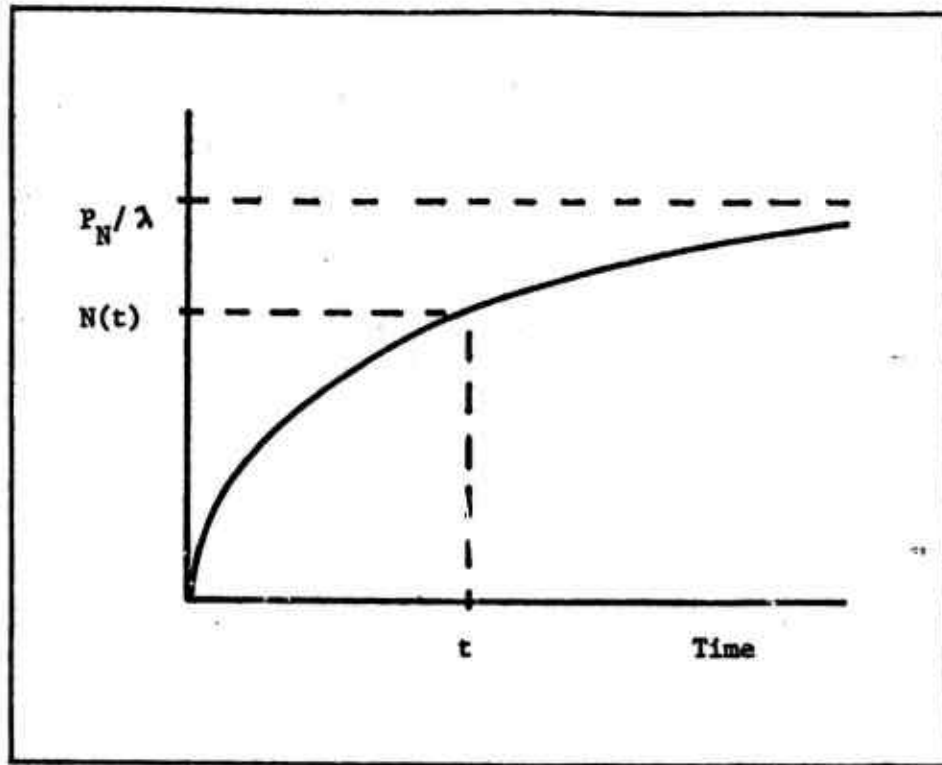


Figure 6. Growth of radioisotope of decay constant λ .

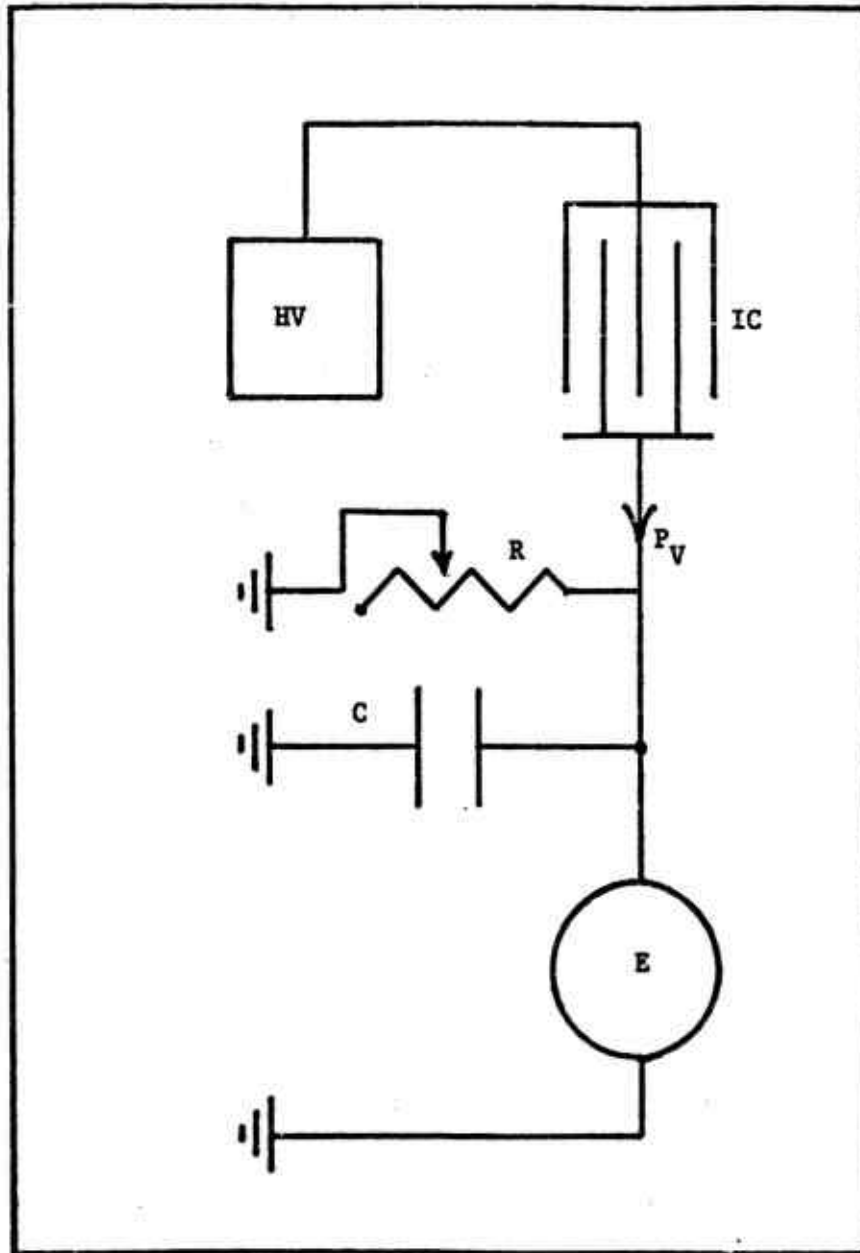


Figure 7. RC circuit of radiation monitor system.
HV - High Voltage. IC - Ionization Chamber.
R - Resistor. C - Capacitor. E - Electrometer.

in Figure 8. Since both the sample and the monitor are exposed simultaneously to the same bremsstrahlung beam intensity, $V(t)$ varies with time as does $N(t)$.

The total monitor response $V_o(T)$ is the product of the change in potential P_v as seen by the electrometer and of the time the potential undergoes change, the irradiation time t_r

$$V_o(T) = P_v t_r . \quad (41)$$

The rate of change of the potential across the RC circuit of Figure 7 can be described by the differential equation

$$\frac{dV(t)}{dt} = P_v - \frac{V(t)}{RC} \quad (42)$$

where $V(t)$, R , and C are the circuit's voltage as a function of time and the resistance and capacitance, respectively. Integration of Eq. (42) over time yields the following expression for the voltage $V(t)$

$$V(t) = RCP_v [1 - \exp(-t/RC)] . \quad (43)$$

Solving Eq. (43) for P_v and substituting in Eq. (41) results in the following expression for V_o

$$V_o = V(t)t_r/RC[1 - \exp(-t/RC)] . \quad (44)$$

The normalized yield of Eq. (37) is now specified through Eqs. (40) and (44). If the RC constant of the circuit is adjustable by means of a variable resistance such that

$$RC = 1/\lambda \quad (45)$$

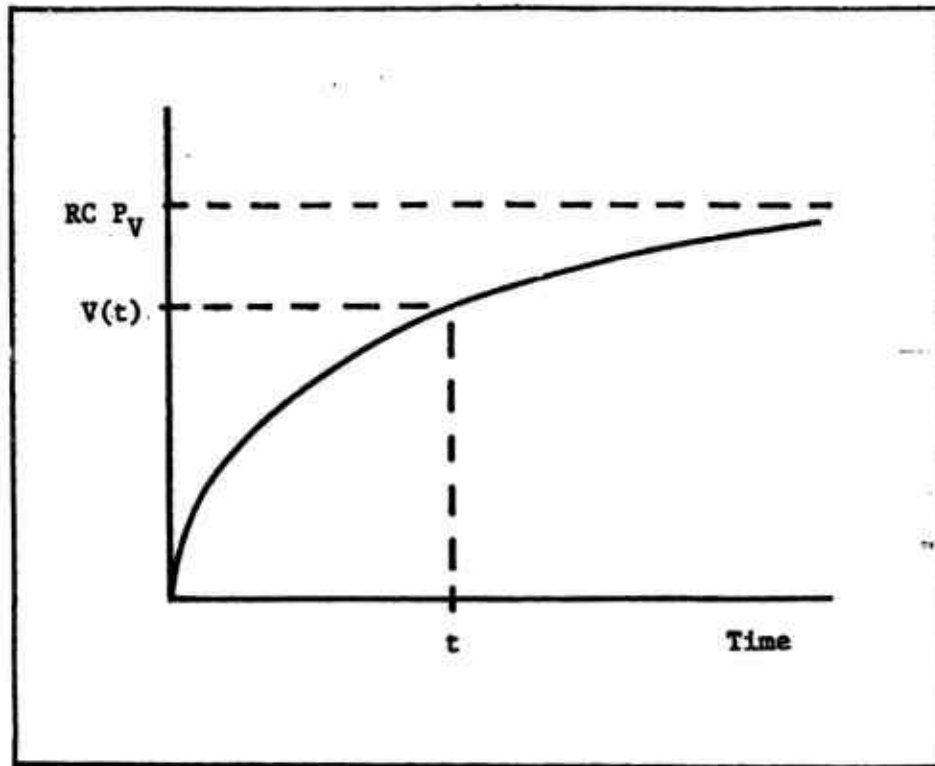


Figure 8. Growth of potential across the capacitor C of the RC circuit of Fig. 7.

then Eq. (37) reduces to

$$Y_{\text{R}}(T) = N(t_{\text{R}})/V(t_{\text{R}}) \quad (46)$$

where $N(t_{\text{R}})$ is the number of radioactive nuclei in the sample immediately following an irradiation of duration t_{R} , and $V(t_{\text{R}})$ is the integrated monitor system voltage measured by the electrometer after the ionization chamber has been irradiated for a time period t_{R} .

A sample containing $N(t_{\text{R}})$ radioactive nuclei of decay constant λ decays with an activity

$$A(t_{\text{R}}) = N(t_{\text{R}})\lambda \quad (47)$$

disintegrations per unit time. The sample activity is decreased during the time the sample is transported from its irradiation location to its appropriate position in the radioactivity counter. If this transit time is denoted t_{t} , the activity of the sample at the start of the counting period may be given by

$$A(t_{\text{t}}) = A(t_{\text{R}})\exp(-\lambda t_{\text{t}}). \quad (48)$$

The sample activity at time t_{R} from Eq. (47) is substituted in Eq. (48) to yield an expression for the sample activity at time t_{t} as a function of the number of radioactive atoms in the sample at time t_{R}

$$A(t_{\text{t}}) = N(t_{\text{R}})\lambda\exp(-\lambda t_{\text{t}}). \quad (49)$$

The sample activity is now measured using a gamma-ray pulse-height spectrometer system. Let C be the number of counts registered in a pulse-height interval (or window) ΔE_{Y} centered at the photopeak of an

appropriate gamma-ray energy E_γ of the radioisotope assayed. C is related to the activity of the sample at the start of the count $A(t_c)$ and to the counting time t_c through the integral equation

$$C = K \int_0^{t_c} A(t_c) [\exp(-\lambda t_c)] dt \quad (50)$$

The term in brackets accounts for radioactive decay during the counting period. The constant of proportionality K (counts per disintegration) relates the total number of sample disintegrations integrated over time t_c to the net number of counts registered in the pulse-height window of the counting system.

Integration of Eq. (50) produces

$$C = \frac{K}{\lambda} A(t_c) [1 - \exp(-\lambda t_c)] . \quad (51)$$

If the expression for $A(t_c)$ of Eq. (49) is now substituted in Eq. (51) and the resulting equation is solved for $N(t_r)$, the number of radioactive nuclei in the sample at time t_r , one obtains

$$N(t_r) = C/K\tau \quad (52)$$

where

$$\tau = \exp(-\lambda t_c) [1 - \exp(-\lambda t_c)] . \quad (52a)$$

The normalized yield $Y_n(T)$ of Eq. (46) is now completely specified. If we now rename the quantity $V(t_r)$ of Eq. (46) as simply V and substitute Eq. (52) into Eq. (46), the normalized yield becomes

$$Y_n(T) = C/K\tau V. \quad (53)$$

This is the required normalized yield expression [Eq. (37)] as a function of experimentally determined quantities. $Y_n(T)$ is the normalized yield, in number of photonuclear reactions per unit monitor response, required for the solution of the photonuclear yield function. C is the net number of counts in the gamma-ray spectrometer pulse-height window. The proportionality constant K relates the total number of radioactive decay events of the sample to the radioactivity count C . The constant K is a function of the counter efficiency for an emitter of the specific gamma-ray energy counted, of the relative intensity of the gamma ray, and of sample self-absorption. V is the output voltage signal of the RC circuit of the radiation monitor system integrated over the irradiation time t_x . And τ , defined by Eq. (52a), is simply a function of the radioisotope decay constant λ and of the sample transit and counting times t_t and t_c , respectively.

Photonuclear Ratios

In this section are derived the formulae used to calculate photonuclear ratios. Three assumptions have been made in the derivation. First, photonuclear reactions result in gamma-emitting radioactive nuclei such that the photonuclear yield may be determined by a gamma-ray detection system. Second, the elements in which photonuclear reactions are produced are contained in a single chemical compound. Third, the radioactivity produced in each element can be determined separately. The formulae are derived in a manner analogous to the derivation of the equation for the calculation of normalized yield.

The number of photonuclear reactions induced in a sample irradiated at constant intensity for a time t_r may be given as

$$N' = P_N t_r \quad (54)$$

where N' is the total number of photonuclear reactions produced in the sample, P_N is the constant photonuclear reaction production rate (reactions per unit time), and t_r is the irradiation time. If, as commonly occurs, the photonuclear reactions result in radioactive nuclei, these decay as they are produced. If the radioactive species decay with decay constant λ , then the sample's activity immediately following irradiation A_{tr} is

$$A_{tr} = P_N (1 - e^{-\lambda t_r}) \quad (55)$$

Solving Eq. (55) for P_N and then substituting the resulting expression in Eq. (54) yields

$$N' = A_{tr} t_r / (1 - e^{-\lambda t_r}) \quad (56)$$

If the sample radioactivity is counted at a location different from its irradiation position, the sample decays during the time it is transported from its location in the irradiation room to the radioactivity counter. If this transit time is denoted t_t , then the activity of the sample after transit and at the onset of counting is

$$A_{tt} = A_{tr} (e^{-\lambda t_t}) \quad (57)$$

where A_{tt} is the activity of the sample which remains after it has been removed from its location in the irradiation room and has been placed in

the counter. Solving Eq. (57) for A_{tr} and substituting the resultant expression in Eq. (56) yields the following expression for N' :

$$N' = A_{tt} t_r / (1 - e^{-\lambda t_r}) (e^{-\lambda t_t}) . \quad (58)$$

At this point, the sample is counted in a gamma-ray spectrometer. The total number of counts registered in a pulse-height interval, or window ΔE_γ , centered about the photopeak of an appropriate gamma-ray energy E_γ , is integrated. The sample is counted for a time t_c and the net number of counts (after background subtraction) registered in the photopeak is C . The number of net counts C is related to the sample's activity A_{tt} at the start of the count through the integral equation

$$C = K \int_0^{t_c} A_{tt} e^{-\lambda t} dt \quad (59)$$

where the exponential within the integral accounts for sample decay during the counting period. The constant of proportionality K relates the disintegration of the sample to the counts registered in the spectrometer pulse-height window. It is a function of the number of gamma rays per decay η , the counting system photopeak efficiency ϵ for gamma rays of energy E_γ from the sample if there were no self-absorption, and the sample self-absorption factor α

$$K = \eta \epsilon \alpha . \quad (60)$$

Integration of Eq. (59) yields

$$C = \frac{K}{\lambda} A_{tt} (1 - e^{-\lambda t_c}) . \quad (61)$$

Solving Eq. (61) for A_{tt} and substituting in Eq. (58) yields an expression for N' in terms of the measured counts C

$$N' = \frac{C\lambda t_r}{\eta \epsilon \alpha (1 - e^{-\lambda t_c})(1 - e^{-\lambda t_r})(e^{-\lambda t_t})} \quad (62)$$

In order to make N' , the number of photonuclear reactions which are produced in the sample, independent of the sample mass, N' is divided by n_s , the number of target nuclei in the sample. This quotient yields N , the number of photonuclear reactions induced in the sample per target nucleus

$$N = N'/n_s \quad (63)$$

where

$$n_s = \frac{N_A}{A} m_s p \gamma \quad (63a)$$

In Eq. (63a), N_A is Avogadro's number, A is the atomic mass of the target nucleus, m_s is the mass of the sample, γ is the fractional natural abundance of the target isotope, and p is the fraction of the sample molecular weight made up by the target element. The fraction p is

$$p = xA/M_w \quad (63b)$$

where A is the atomic weight of the target element, M_w is the molecular weight of the compound, and x is the number of atoms of the target element per molecule of compound.

The final expression for the number of photonuclear reactions per target nucleus induced in the sample is

$$N = \frac{C\lambda t_r A}{\eta \epsilon \alpha N_A m_s p \gamma \tau} \quad (64)$$

where

$$\tau = (1 - e^{-\lambda t_c})(1 - e^{-\lambda t_r})(e^{-\lambda t_t}) \quad (64a)$$

N is the number of photonuclear reactions produced in the sample per target nucleus, C is the number of net photopeak counts integrated over the count time, λ is the decay constant of the radioisotope produced, A is the atomic mass of the target element, η is the number of gamma rays of interest emitted by the radioisotope produced per disintegration, ϵ is the counting-system efficiency without self-absorption for the particular gamma ray in photopeak counts per disintegration, α is the self-absorption factor of the sample for the gamma ray, N_A is Avogadro's number, m_s is the sample mass, p is the fraction of the sample molecular weight made up by the target element [as given by Eq. (63b)], γ is the natural abundance of the target isotope, and t_c , t_r and t_t are the counting, irradiation and transit times, respectively.

Equations (64) are similar to Eq. (1) in the paper of Nath and Schulz on photoactivation ratios (9). Their photoactivation ratios are expressed in terms of activity A_∞ that would be produced in the sample by photonuclear reactions if it were irradiated indefinitely. For irradiation times much longer than the half-life of the radioisotope being produced, the activity of the sample following irradiation [as given by Eq. (55)] becomes

$$A_\infty = P_N(1 - e^{-\lambda t_r}) = P_N \quad (65)$$

because $e^{-\lambda t_r}$ approaches zero when $t_r \gg$ half-life of the radioisotope produced. Substituting $P_N = A_\infty$ in Eq. (54) yields

$$N' = A_\infty t_r \quad (66)$$

where A_∞ is the activity that would be induced in the sample following an indefinitely long irradiation (equilibrium activity). The value of N' resulting from Eq. (66) is now substituted in Eq. (62) and the activity A_∞ is divided by the number of target nuclei n_s to obtain

$$R = \frac{C\lambda A}{\eta \epsilon \alpha N_A m_s p \gamma \tau} = \frac{A_\infty}{n_s} \quad (67)$$

where R is the activity (in disintegrations per second) per target nucleus induced in the sample following an indefinitely long irradiation. The remaining variables have been previously defined. Equation (67) is identical to Nath and Schulz's Eq. (1) if it is noted that for very thin foils of pure elements, which they used as samples in their experiment, the sample self-absorption factor α and the fraction p of the sample molecular weight made up by the target element equal 1.0.

The samples used in this study consisted of chemical compounds containing the two elements in which the number of photonuclear reactions induced were of interest. The parameter used to characterize bremsstrahlung endpoint and spectral quality is the ratio of the number of photonuclear reactions per target nucleus induced in element 1 to the number of photonuclear reactions per target nucleus in element 2. The photonuclear ratio PR is defined as

$$PR = N_1/N_2 \quad (68)$$

where N_1 and N_2 are the number of photonuclear reactions produced per target nucleus in elements 1 and 2, respectively. The photonuclear ratio PR, in terms of the numbers of counts C_1 and C_2 from the radioisotopes produced in elements 1 and 2, is given by

$$PR = \frac{C_1 \lambda_1 A_1 / \eta_1 \epsilon_1 \alpha_1 P_1 \gamma_1 \tau_1}{C_2 \lambda_2 A_2 / \eta_2 \epsilon_2 \alpha_2 P_2 \gamma_2 \tau_2} = \frac{N_1}{N_2} \quad (69)$$

Equation (69) follows from the quotient of N_1/N_2 as given by Eqs. (64, 64a). The terms t_r , N_A , and m_s are constant and drop out of the ratio. Equation (69) is of a very general nature and applies to photonuclear ratio calculations in almost any experimental situation.

Equation (69) can be simplified somewhat if, as occurs in this experimental work, the energies E_γ of the gamma rays producing the counts C_1 and C_2 are equal. Under this circumstance, the detector efficiency ϵ and the sample self-absorption factor α , both of which are a function of photon energy, drop out of the ratio. The photonuclear ratios of this experiment were computed using the simplified formula

$$PR = \frac{C_1 \lambda_1 A_1 / \eta_1 P_1 \gamma_1 \tau_1}{C_2 \lambda_2 A_2 / \eta_2 P_2 \gamma_2 \tau_2} \quad (70)$$

Note that the photonuclear ratio given by Eq. (69) is algebraically equivalent to the ratio R_1/R_2 given by Eq. (67).

CHAPTER III

MATERIALS AND METHODS

Materials

Samples

Samples used for photonuclear ratio determination utilizing the method of induced activity should satisfy certain criteria:

1. Sample elements in which photonuclear reactions are to be studied must contain nuclides which produce radioactive isotopes upon irradiation. The radioactive specimen should be a gamma-emitter of large enough branching ratio that an activity measurement can be appropriately made by counting that particular gamma ray.
2. The half-life of the resultant radioisotope should be short enough to allow a fair amount of radionuclide production upon irradiation for a reasonable amount of time. The radioisotope half-life, on the other hand, should be long enough so that a sizable fraction of the radioactivity remains after the sample has been transferred from the irradiation room to the counting system.
3. The specific target isotope to be studied should have a high natural abundance.
4. The sample material should be stable and preferably in solid

form at room temperature. The sample material should be readily available and inexpensive.

In addition to the above criteria, the samples used in this study met the following conditions:

1. The sample consisted of a chemical compound containing the two elements for which the photonuclear yields were of interest. Because of this, both elements in the compound were exposed to exactly the same bremsstrahlung beam fluence, and measurement of the fluence to which the sample is exposed was unnecessary.

2. The radioisotopes produced by photonuclear reactions in each element emitted the same energy gamma ray. This condition made determination of the counting-system efficiency as a function of gamma-ray energy unnecessary. The condition further restricted the half-lives of the radioisotopes produced. The half-lives of the radioisotopes had to be sufficiently different so that the activity of each could be determined by counting the sample at two different times. The procedure for doing this is explained in detail in the Methods section of this chapter.

3. The elements in the compound had to possess photonuclear cross sections differing in threshold energy and giant resonance location such that the photonuclear yield taken as a function of bremsstrahlung endpoint energy in one element remained fairly constant while the yield in the second element changed rapidly in the same energy range.

The primary aim of determining photonuclear ratios was to obtain an index of spectral quality for bremsstrahlung in the megavoltage region and particularly in the energy range from 15 to 30 MeV, where such ratios are lacking. No one sample was found that was suitable for production of

unique photonuclear ratios as a function of bremsstrahlung endpoint energy encompassing the entire 15 to 30 MeV range. Therefore, the energy range was divided and two sets of ratios were determined requiring two different samples. In the lower half of this energy range (from approximately 15 to about 22 MeV), the sample of choice was potassium hexafluorosilicate (K_2SiF_6). The photonuclear reactions producing the ratios were the $^{39}K(\gamma,n)^{38}K$ and the $^{19}F(\gamma,n)^{18}F$ reactions. In the upper half of the range (approximately 23 to 30 MeV), the $^{12}C(\gamma,n)^{11}C$ and $^{19}F(\gamma,n)^{18}F$ reactions in polytetrafluoroethylene ($F_2C=CF_2$), or "teflon," produced the desired ratios. The relevant characteristics of these reactions are summarized in Table 1.

The K_2SiF_6 samples consisted of approximately 30.7 g of 99% purity K_2SiF_6 powder contained in a cylindrical aluminum can 3.2 cm in diameter and 4.1 cm high. The activity induced in the aluminum was extremely short-lived (6.34 sec) compared to the half-lives of the radioisotopes of interest (^{38}K - 7.63 min, ^{18}F - 109.8 min). The aluminum activity was allowed to decay before the sample was counted. The molecular weight of K_2SiF_6 is 220.25. The potassium (atomic weight 39.098) fraction of the sample molecular weight is 0.355. The fluorine (atomic weight 18.998) fraction of the sample molecular weight is 0.517. The natural abundance of ^{39}K is 93.1%, that of ^{19}F is 100%.

The teflon samples consisted of 2.5-cm-long pieces of teflon rod 1.3 cm in diameter. The weight of each sample was approximately 7.0 g. The molecular weight of teflon is 100.02. The carbon (atomic weight 12.011) fraction of the sample molecular weight is 0.24. The fluorine fraction is 0.76. The natural abundance of ^{12}C is 98.89%.

Table 1Photonuclear Reactions Used for Ratios

	$^{12}\text{C}(\gamma, n)^{11}\text{C}$	$^{19}\text{F}(\gamma, n)^{18}\text{F}$	$^{39}\text{K}(\gamma, n)^{38}\text{K}$
Threshold (MeV)	18.7	10.4	13.1
Half-life of Product (min)	20.3	109.8	7.63
Decay const. (min^{-1})	.034	.0063	.091
Gamma Energy (MeV)	.511	.511	.511
Photons per decay	1.98	1.94	1.98

The aluminum samples used to measure the $^{27}\text{Al}(\gamma, 2p)^{25}\text{Na}$ yield curve consisted of aluminum shot (~ 1.0 mm diameter) tightly encased in aluminum cans identical to those used for the K_2SiF_6 samples. The aluminum was 99.95% pure. The natural abundance of the ^{27}Al isotope is 100%. The sample mass averaged 36.5 grams with a maximum deviation from the mean of less than 0.1%. The characteristics of the $^{27}\text{Al}(\gamma, 2p)^{25}\text{Na}$ reaction are summarized in Table 2.

Sample Holders

The precise determination of yields required that samples be irradiated and counted in a very reproducible fashion. To satisfy this requirement purpose, sample holders were designed and constructed (57). The sample holder used for sample irradiation allowed rapid insertion and removal. It held the sample close to the bremsstrahlung target, thus increasing the photon beam fluence accordingly. Furthermore, it permitted very reproducible sample positioning. The sample holder used for sample counting also permitted rapid sample insertion and removal. It allowed reproducible positioning of the samples at any one of several precisely measured distances from the detector. These holders are described in the following paragraphs.

The sample holder assembly used for irradiation is shown in Figure 9a. It contained a radial collimator constructed of poured cerrobend alloy (Lipowitz alloy, attenuation properties similar to lead). The radial collimator was 7.6 cm in diameter and 13.3 cm long. The collimator channel defined a truncated cone of entrance aperture 1.46 cm in diameter and exit aperture 2.16 cm in diameter. Using a small aluminum collar, the sample was positioned flush against the exit aperture of the collimator

Table 2 $^{27}\text{Al}(\gamma, 2p)^{25}\text{Na}$ Reaction

Threshold (MeV)	24.2
^{25}Na Half- life (sec)	60.0
^{25}Na Decay Constant	.01155
Gamma Ray Energies (MeV) and Intensities	.975 (14.5%) 1.612 (9.5%)

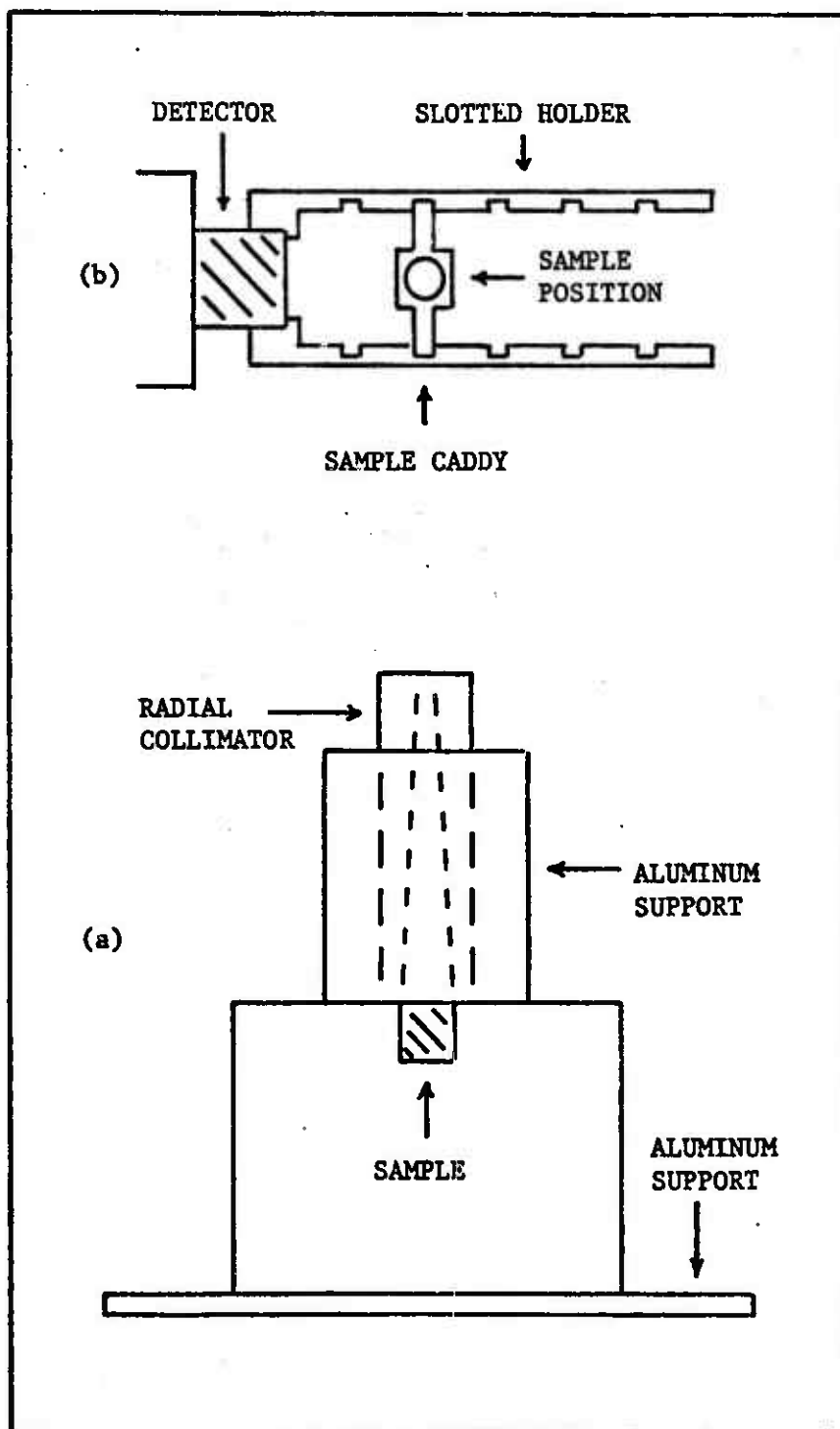


Figure 9. Sample holder assemblies,
(a) for irradiation, (b) for counting.

with its central axis coincident with that of the truncated cone defining the collimator channel. The radial collimator and sample-bearing collar were supported by means of an aluminum assembly as shown in Figure 9a. The assembly was attached to a 0.5-in-thick aluminum plate. The entire structure was then secured to the linac collimator by fitting holes in the plate over rods imbedded in the linac collimator housing. These rods were tapped so that the plate was held firmly in place by nuts screwed onto the rods. When properly positioned, the entrance aperture of the radial collimator was located 27.8 cm from the bremsstrahlung target. When in place, the entrance face of the sample was 41.1 cm from the target, and its central axis was coincident with the central axis of the bremsstrahlung beam.

Reproducible sample positioning for radioactivity counting was also imperative. This was accomplished by positioning the samples in another sample holder which was attached firmly to the detector as shown in Figure 9b. This assembly, made of plexiglas, was slotted so that a sample caddy could be inserted into these slots at some well-known distance to the detector face. The sample was placed into the sample holder so that the cylindrical sample axis was vertical and parallel to the front face of the detector. Using this apparatus the reproducibility of the sample location with respect to the detector was within less than 1 mm.

Linear Accelerator

The linear accelerator was the most important piece of equipment used in this study. The linac was the source of the bremsstrahlung beams used in this work. Operational principles of medical electron linear accelerators in general are discussed in Appendix C. This section

describes the particular accelerator used. Later, the experimental use of the accelerator will be discussed. The linac operating parameters which influence the kinetic energy achieved by the accelerated electrons are described and their appropriate values are defined.

The accelerator used to produce the bremsstrahlung beams of this study was a Sagittaire/Therac 40 electron linear accelerator manufactured by CGR-MeV of France belonging to the Radiation Therapy Department of the University of Oklahoma Health Sciences Center. In its clinical mode, the Sagittaire can deliver electron beams at nominal energies of 7, 10, 13, 16, 19, 22, 25, 28, 32, and 40 MeV. A 25 MeV bremsstrahlung beam is also available in the clinical mode. Six dose rates at the isocenter can be chosen for both the bremsstrahlung and electron beams: .5, 1, 2, 3, 4, and 10 Gy per min.

The Sagittaire/Therac 40 linac is shown schematically in Figure C1 (Appendix C). It essentially consists of three major components: 1) the microwave power supply section, 2) the electron injector and accelerator system, and 3) the gantry and treatment head component. In the modulator room, microwave power was provided by a 3,000 MHz oscillator and a klystron microwave amplifier. In the accelerator room, electrons are injected into the acceleration guides by an electron gun. There, the electrons are accelerated by the amplified 3,000 MHz microwaves, traveling through two iris-loaded cylindrical wave guides. The energy gained by the electrons is controlled primarily by the degree of phase-coupling between the traveling waves in sections 1 and 2. This task is performed by a phase shifter consisting of a quartz rod which is inserted into the rectangular wave guide feeding section 1 (see Appendix C).

Accelerated electrons exit from the second accelerator section and then enter the gantry of the accelerator which is located in the treatment room. The electron beam direction is controlled by two magnet systems located in the gantry. The first magnet system analyzes the electron beam energy by means of a bending electromagnet and an energy-defining slit. The second system consists of two magnetic beam-bending devices that redirect the electron beam to a direction perpendicular to the acceleration wave guides. The beam then enters the therapy head where removable bremsstrahlung targets may be inserted into the electron beam to produce x rays or may be removed to allow the electron beam to emerge. The radiation beam is finally collimated by a set of fixed and variable collimators, and its intensity is monitored by a system of transmission ion chambers which also serves to control the beam centering.

The accelerator could be operated in what is called the "experimental mode. Most of the bremsstrahlung beams used in this study were produced in this mode. The beams produced in this mode are termed photon II beams (in contrast to the clinical photon beam which is called photon I). Photon II beams differ from photon I beams only in the amount of filtration after bremsstrahlung production. Both beams are produced in identical 4-mm-thick tungsten targets although each has its own target. The clinical photon I beam must traverse an approximately 2.8-cm-thick (central dimension) lead flattening filter. The photon II beams, on the other hand, are filtered by a 2.7-mm-thick lead plate whose purpose is solely to increase the amount of signal available to the ionization chambers for beam steering.

A prominent parameter which describes the bremsstrahlung beam

of a linear accelerator is its endpoint energy. The bremsstrahlung endpoint energy is the maximum photon energy in the photon spectrum. It is usually taken to correspond to the mean kinetic energy of the electrons incident on the bremsstrahlung target. This section describes the accelerator operating parameters which determine the final kinetic energy of the electrons. Also discussed is the method employed in the accelerator to define and control the kinetic energy of the electrons prior to radiation.

The resultant energy of the accelerated electrons is determined by a unique set of values of the following parameters (see Appendix C): 1) the magnitude (amplitude) of the axial electric field of the radio-frequency traveling waves, 2) the relative phase-coupling between the traveling waves in the first and second acceleration sections, and 3) the field strength of the bending magnet which analyzes the energy of the electron beam. The first parameter (axial field amplitude) is controlled by the amount of radiofrequency high voltage (RFHV) applied. The second parameter (phase-coupling) is controlled by the relative position of the quartz rod inserted in the wave guide that feeds section 1. The third parameter, analyzing magnet field strength, is controlled by the current supplied to the energy-analyzing electromagnet.

The energy of the electron beam is ultimately determined by the linac energy-analysis system. This system defines the electron energy to $\pm 2\%$ of the mean energy (94). The magnetic analyzer deflects the accelerated electrons through angles determined by the electron kinetic energy. Because of the major role played by the energy-analysis system, the fundamental principles of this system require discussion.

A charged particle of velocity v entering a uniform magnetic field of magnetic induction \vec{B} experiences a force \vec{F} perpendicular to the direction of motion and to the magnetic induction. Because there is no component of this force along the particle's direction of motion, the particle speed is unchanged but the particle is forced to move in a circular path. If a particle is to move in a circular path at a constant speed, it must be subjected to a centripetal force. Thus, we have for an electron of charge e , mass m_e , and velocity v in a magnetic induction \vec{B} (58,59)

$$Bev = \frac{m_e v^2}{r} \quad (71)$$

where r is the radius of curvature of the circular path into which the electron is forced to move. Rearranging Eq. (71) and substituting an alternate expression for the momentum p (60) yields

$$Berc = (T^2 + 2m_e c^2 T)^{1/2} = pc \quad (72)$$

where T is the electron kinetic energy and c is the speed of light.

According to Eq. (72), for a given constant magnetic induction B , an electron will move in a circular path of radius r determined by the electron energy T . In the energy-analysis system of the accelerator, shown schematically in Figure 10, the degree of deflection (which depends upon r) of the electron produced by the bending-magnet induction depends on the electron energy. Only electrons of kinetic energy within 2% of an appropriate mean energy will be deflected into a radius of curvature such that they are allowed transmission by the energy-defining slit.

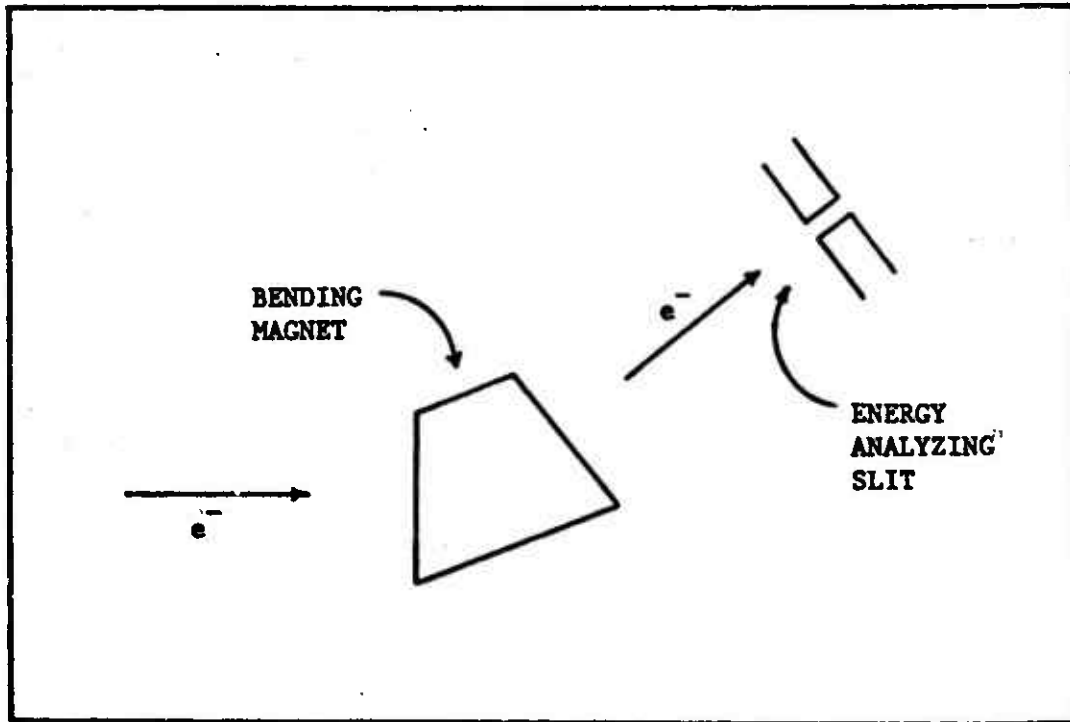


Figure 10. Electromagnetic energy analyzing system.

The appropriate mean energy T is that which satisfies the relation of Eq. (72). RF power is automatically changed if the electron energy deviates from the requested energy as determined by the magnetic induction of the bending magnet.

Electron kinetic energy selection is made possible by virtue of the fact that the degree of deflection of an electron of a certain energy in the energy-analysis system depends upon the magnitude of the magnetic induction of the bending magnet. This also follows from Eq. (72). The magnetic induction is directly proportional to the amount of current I supplied to the electromagnet. With this in mind, Eq. (72) thus can be written in the form

$$I = K(T^2 + 2m_e c^2 T)^{1/2} \quad (73)$$

where K is a function of e , r , c and of the specifics of the magnet system. It is constant as long as saturation and residual magnetization effects are negligible. The exact form of Eq. (73) can be found by measuring the energy of electrons transmitted by the energy-analysis system as a function of the current applied to the bending magnet. Once known in its exact form, the equation can then be used to select certain electron energies by choosing the appropriate current to the magnet of the energy-defining system.

Measurements of the type described above have recently been performed on the accelerator. The exact relationship between the electron kinetic energy and the current to the energy-analyzing magnet was found and published (6,57). The authors used three energy calibration points supplied by photonuclear reactions to relate magnet current to electron

energy: the 10.8 MeV $^{63}\text{Cu}(\gamma, n)^{62}\text{Cu}$ threshold, the 17.3 MeV break in the $^{16}\text{O}(\gamma, n)^{15}\text{O}$ yield curve and the 29.2 MeV $^{32}\text{S}(\gamma, 3p)^{29}\text{Al}$ threshold. They found the deviation magnet current corresponding to each of the above electron energies and a function of the form

$$I^2 = K_1 T^2 + K_2 T \quad (74)$$

K_1 and K_2 constants was fit to the experimental points by using a least-squares procedure. Note that Eq. (74) can be obtained by squaring Eq. (73) and redefining the constants. The resulting relation between magnet current and electron kinetic energy was

$$I = (37.7T^2 + 90.3T)^{1/2} \quad (75)$$

From this relation, shown in Figure 11, one can obtain the magnet current which is necessary to produce an electron beam of a desired kinetic energy.

The current to the energy-defining electromagnet is monitored by measuring the voltage drop across a sampling resistor, as shown in Figure 12. In this fashion, the reading of a digital voltmeter (DVM) serves as an index of magnet current. In the accelerator experimental mode, the current to the analyzing magnet is continuously adjustable by means of a ten-turn helipot located at a convenient point in an electronics rack which in turn is located in the modulator room. In the clinical mode, the current to the electromagnet is fixed at the value appropriate for the clinical beam to be used. The position of the switch S of Figure 12 determines whether the linac is operated in the experimental mode or in the clinical mode.

In the clinical mode, when one of the ten available energies is

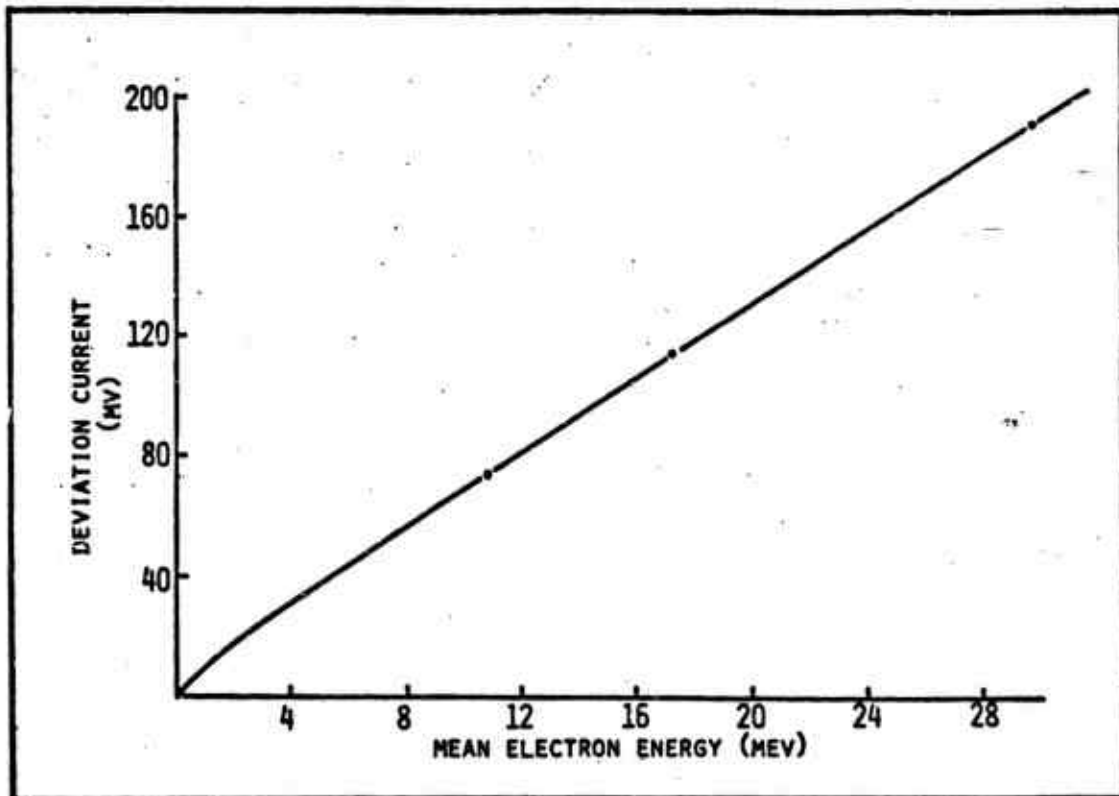


Figure 11. Relation between mean electron kinetic energy and deviation current to the bending magnets of the energy - analysis system of the Sagittaire accelerator. From Ref. (57).

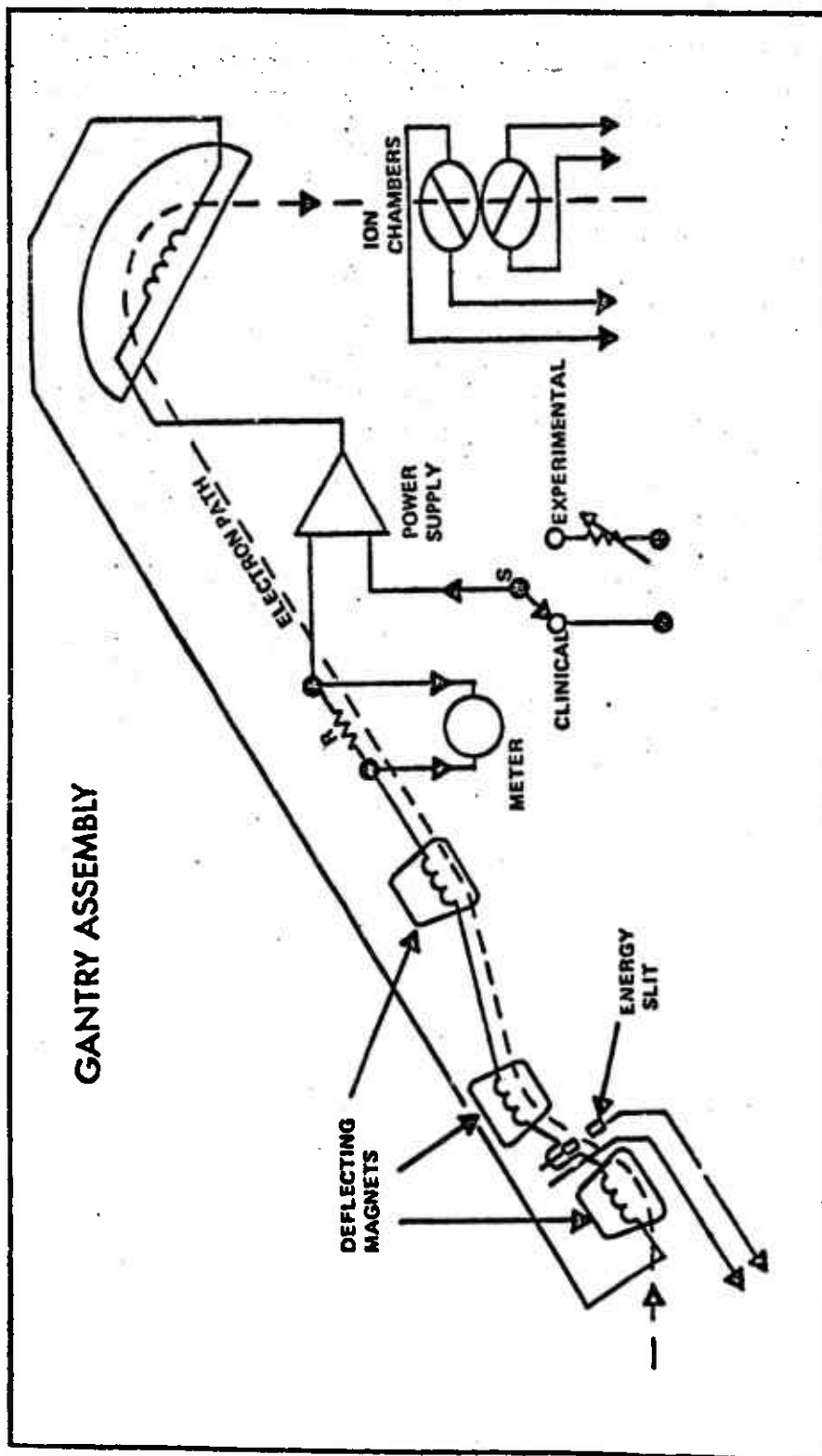


Figure 12. Linear accelerator modification.

selected, the phase-coupling and analyzing magnet current are set automatically and the RFHV is controlled by a servo mechanism. In the experimental mode, the energy selection switches are bypassed and the automatic servo mechanisms regulating the energy control parameters are disabled so that the energy-defining magnet current, phase-shifter position, and RFHV can be set and maintained manually. A bremsstrahlung beam of a desired endpoint energy is obtained by first selecting the appropriate energy-analyzing magnet current (as measured by the DVM) corresponding to the desired endpoint energy. The appropriate phase and RFHV values are then set. The proper settings had been obtained earlier (57) by keeping to a minimum the gun current required to keep the selected endpoint energy beam at a constant given intensity. The appropriate linear accelerator operating parameters as a function of bremsstrahlung beam endpoint energy are presented in Table 3.

Counting System

Sample activity was measured with a high-purity germanium (HPGe) semiconductor detector gamma-ray spectroscopy system. These systems are best known for their excellent energy resolution. This resolution enables the separation of interference peaks from the full energy (total absorption) peak. The system used in the present work for activity determination possessed an energy resolution of 0.3% FWHM at 1332.5 keV. A basic description of the principles and characteristics of semiconductor spectrometer systems is provided in Appendix D. The present section is a description of the particular system used in this study. Discussed are the specifications of each component of the system and the system performance.

Table 3Linear Accelerator Operating Parameters

T_{ave} (MeV)	I_{ave} (mV) D.V.M.	Phaae Setting D.V.M.	R.F.H.V. D.V.M.
12.0	80.7	0.172	.470
12.5	83.8	0.177	↓
13.0	86.9	0.182	
13.5	89.9	0.188	
14.0	93.0	0.194	
14.5	96.1	0.199	
15.0	99.2	0.205	
15.5	102.3	0.211	
16.0	105.3	0.218	
16.5	108.4	0.224	
17.0	111.5	0.230	
17.5	114.6	0.236	
18.0	117.6	0.243	
18.5	120.7	0.250	
19.0	123.8	0.256	
19.5	126.9	0.263	
20.0	129.9	0.271	
20.5	133.0	0.279	
21.0	136.1	0.287	
21.5	139.2	0.296	
22.0	142.2	0.304	
22.5	145.3	0.314	
23.0	148.4	0.324	
***	***	***	

Table 3 (Continued)Linear Accelerator Operating Parameters

T _{ave} (MeV)	I _{ave} (mV)	Phase Setting	R.F.H.V.
	D.V.M.	D.V.M.	D.V.M.
23.5	151.5	0.452	.446
24.0	154.5	0.446	.449
24.5	157.6	0.440	.452
25.0	160.7	0.434	.455
25.5	163.8	0.428	.459
26.0	166.8	0.423	.462
26.5	169.9	0.418	.465
27.0	173.0	0.412	.468
27.5	176.1	0.407	.471
28.0	179.1	0.402	.473
28.5	182.2	0.396	.476
29.0	185.3	0.392	.479
29.5	188.3	0.388	.481
30.0	191.4	0.384	.483
30.5	194.5	0.380	.485
31.0	197.6	0.376	.488
31.5	200.7	0.374	.490
32.0	203.7	0.372	.492
32.5	206.8	0.370	.494
33.0	209.8	0.370	.495

The detector was a closed-end coaxial type high-purity germanium detector manufactured by Princeton Gamma-Tech (PGT). It was a cylinder 4.0 cm long and 4.3 cm diameter with an entrance window of aluminum 0.1 cm thick (61). The detector was used with a 2100-volt positive bias from a high-voltage power supply and was cooled to 77°K. A copper cold finger, one end touching the detector and the other immersed in liquid nitrogen, provided the conduction path for heat flow. Detector cooling was necessary to reduce thermal noise. The detector was shielded with 10.2 cm lead to reduce the background radiation contribution.

The detector output charge pulse, which is proportional to the number of electron-hole pairs produced by a photon interaction in the detector, was fed into a PGT model RG-11 preamplifier. The preamplifier was located directly adjacent to the germanium detector to minimize pick-up of stray fields. The preamplifier amplified the charge pulse amplitude by a factor of 25,000. The output voltage-pulse of the preamplifier was shaped to have an approximately 10 nsec rise time and 50 usec decay time (61).

The preamplifier output pulse was processed by a Canberra Model 1413 amplifier. This amplifier not only increased the amplitude of the signal pulse but also modified the pulse to a Gaussian shape, thereby increasing the signal-to-noise ratio and making the output pulse compatible with the analog-to-digital converter (ADC) of the multichannel analyzer. The spectroscopic amplifier also had baseline-restorer circuits to minimize the effects of baseline fluctuations.

The amplitude of the pulse from the amplifier, which was proportional to the amplitude of the detector original charge pulse, was digi-

tized by the ADC of a Canberra Model 4100 multichannel analyzer (MCA). The 50 MHz digitizing rate was under crystal clock control. The digitized value of the pulse amplitude determined the location of the analyzer memory to be incremented. Thus, the address of the channel in the array of the MCA memory locations was directly proportional to the radiation energy absorbed in the detector (see Appendix D).

The relationship between the channel number, which corresponds to a given pulse-height interval, and the energy deposited in the detector by a photon interaction event was found by energy-calibrating the pulse-height scale with 11 gamma-ray emitters having a total of 24 gamma rays of known energies (Table 4). The energy calibration was performed so that a 2.5 MeV energy range spanned the MCA's 1024 channels. A straight line was fit to the data of Table 4 using linear regression to obtain the relation between photon energy and channel number.

$$E = (2.47)C + 9.74 \quad (76)$$

where E is the photon energy in keV and C is the channel number. The energy-channel relation was indeed linear with a coefficient of correlation of $r^2 = 1.00$.

The counting-system efficiency as a function of photon energy was investigated using gamma-ray emitters calibrated by the National Bureau of Standards (NBS). The NBS-calibrated sources effectively were point sources (minute quantities of isotope deposited on thin plastic tape). The characteristics of these NBS-calibrated sources are presented in Table 5. Intensities shown in the table are source intensities at the time of calibration.

Table 4Sources used in Counting System Energy Scale Calibration

Sources	Gamma ray Energy (keV)	Channel Number
Eu-152	121.8	46
	344.3	135
	778.9	311
	964.0	386
	1112.1	446
	1408.0	566
Ba-133	276.4	108
	302.8	118
	356.0	141
	383.8	151
Hg-203	279.2	109
Sb-125	427.0	169
	463.0	184
	599.0	239
Cs-137	661.6	264
Kr-85	514.0	204
Bi-207	569.6	227
	1063.4	427
	1769.7	713
Co-58	810.7	324
Mn-54	834.8	334
Co-60	1173.2	471
	1332.5	536
Na-22	1274.6	512

Table 5NBS Sources used in Counting System Efficiency Calibration

Point Sources	Gamma ray Energy (keV)	Intensity (r's per sec)
Bi-207	569.6	(7.786) 10^4
	1063.4	(5.992) 10^4
	1769.7	(5.642) 10^3
Kr-85	514.0	(4.381) 10^4
Ba-133	276.4	(1.106) 10^4
	302.9	(2.985) 10^4
	356.0	(1.014) 10^5
	383.9	(1.503) 10^4
Co-60 / Cs-137	661.6	(3.429) 10^3
	1173.2	(5.356) 10^3
	1332.5	(5.361) 10^3

The point sources of Table 5 were counted at 2.1 cm and 8.2 cm from the detector face. The photopeak efficiency as a function of gamma-ray energy was calculated by dividing the net photopeak count rate (in counts per aec) by the rate of gamma rays of appropriate energy emitted by the source (in gamma rays per sec). Net photopeak counts were obtained by adding the total number of counts in the pulse-height analyzer channels encompassing the entire photopeak and then subtracting the background contribution. Background counts were determined by first averaging the counts in the channels where the photopeak blends into the background continuum and then multiplying the resultant average background counts per channel times the total number of channels in the photopeak. The gamma-ray emission rates of the sources were computed from the source activities as given by the NBS certificates of calibration. Barium-133 gamma-ray intensities were corrected for coincidence-summing effects (62).

The counting-system point-source efficiencies, at 2.1 and 8.2 cm, are presented in Table 6 and Figure 13 as a function of photon energy. Efficiency has been defined as the ratio of the net total photopeak count rate to the gamma-ray emission rate. The efficiency, hence, is in units of counts per second per gamma ray emitted per sec.

The smooth curves of Figure 13 were hand-drawn through the experimental points. The curve shapes are in good agreement with typical efficiency curves for this type detector (63).

Timing Control Apparatus

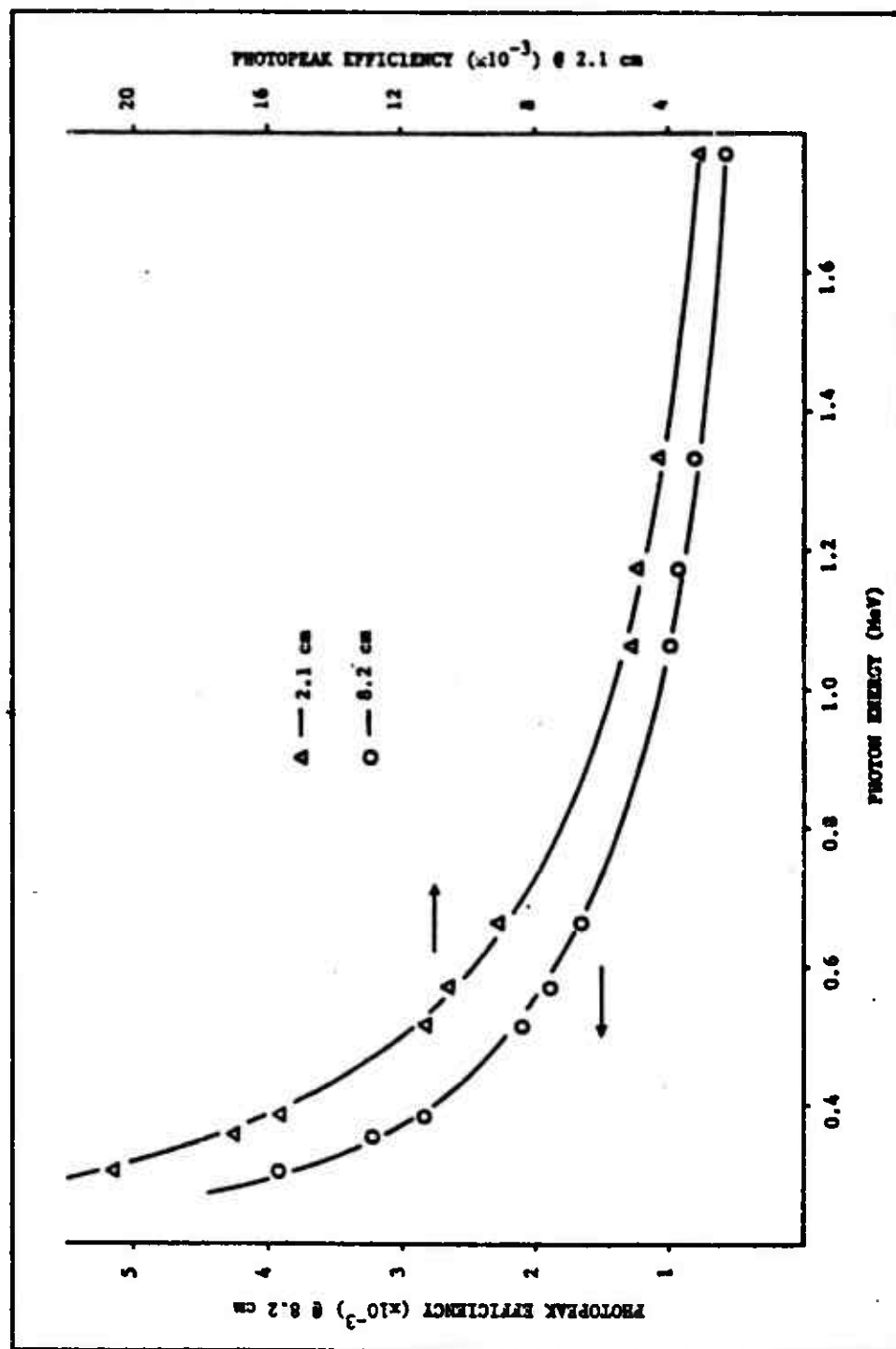
The amount of radioactivity produced by photonuclear reactions in the sample and subsequently measured in the counting system depended very critically on three separate time intervals which had to be fixed

Table 6Counting System Photopeak Efficiency

Energy (keV)	Source	* Photopeak Efficiency ($\times 10^{-3}$)	
		at 2.1 cm	at 8.2 cm
276.4	Ba-133	23.7	4.48
302.9	Ba-133	20.6	3.92
356.0	Ba-133	16.9	3.22
383.9	Ba-133	15.6	2.82
514.0	Kr-85	11.2	2.08
569.6	Bi-207	10.6	1.89
661.6	Cs-137	9.2	1.67
1063.4	Bi-207	5.0	0.98
1173.2	Co-60	4.9	0.94
1332.5	Co-60	4.5	0.82
1769.7	Bi-207	3.0	0.55

* Photopeak efficiency is defined here as net total photopeak count rate (cps) per gamma ray emission rate (γ 's ps)

Figure 13. Intrinsic germanium photopeak efficiency.



precisely. These were the irradiation time, the time required for the transfer of the sample from the linear accelerator to the counter, and the counting time. The counting time was controlled by the present live-time counter in the multichannel analyzer. The irradiation and transfer times were controlled by a timing control apparatus described in the next paragraph.

The timing control apparatus consisted of a module containing two precision electrical clocks which could be preset. The timer module was interfaced with the linac controls and with a start-count gate on the MCA. The irradiation time was set on timer 1 and the sample transfer time was set on timer 2. When the linac was turned on, timer 1 was activated and the irradiation commenced. When the time set on clock 1 ran out, the linac was automatically shut off and a relay started timer 2 which ran while the sample was transferred from the linac to the detector. When timer 2 shut off, a signal pulse was sent to the MCA which started the counting period. This continued until the MCA live-time indicator reached the preset value. With these time-controlling devices, all times were set prior to irradiation and all phases of the experiment advanced automatically.

P-2 Ionization Chamber

Normalized yield determination required measurements of the energy fluence of the bremsstrahlung beam traversing the sample. This was accomplished with an NRS type P-2 ionization chamber, described in detail elsewhere (56), which was located approximately 2.4 meters from the sample. The activity induced in the sample was divided by the response of this ionization chamber to compute the normalized yield.

The experimental arrangement of the ionization chamber and its associated components is shown schematically in Figure 14. The ionization chamber (I) collecting potential was 1200 volts and was supplied by a DC high-voltage power supply (HV). The output current of the chamber was integrated on a high-quality 10.096 μF polystyrene capacitor (C). A variable resistor (R) was introduced in the circuit so that the RC constant was inversely proportional to the decay constant of the radioactive species being produced (see Measurement of Yield section in Chapter II). The potential across the capacitor was measured with a Cary model 401 vibrating reed electrometer (E), which was located in the modulator room of the accelerator. A Varian model 401 preamplifier (P) provided initial amplification and impedance-matching.

The response of the ionization chamber to bremsstrahlung energy fluence was nearly independent of bremsstrahlung endpoint energy. Calibration of the chamber showed a response of approximately 2.4 micro-coulombs per joule of incident energy of $\pm 0.9\%$ from 15 to 35 MeV (56). The measurement system was checked for leakage current, possible recombination losses, and contributions to the ionization current from scattered radiation (57). All effects were found to be negligible under the experimental conditions of this work. System reproducibility was checked at the beginning of each data-collection session by measuring the charge collected when a 30 mg ^{226}Ra source was placed at a specific location on the P-2 chamber. These measurements showed a variability of about 1.2% (standard error) over the course of the entire experiment thus indicating good stability.

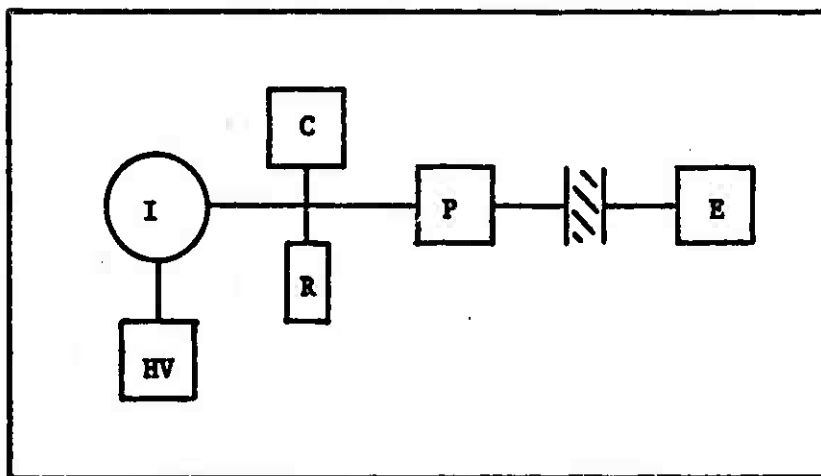


Figure 14. Radiation monitor system arrangement.
I - Ionization Chamber. HV - High Voltage Supply.
C - Capacitor. R - Resistor. P - Preamplifier.
E - Electrometer.

Methods

Photonuclear Ratios

This section describes the procedures followed to acquire and analyze the experimental data used to determine the photonuclear ratios. In general the experimental method consisted of irradiating the K_2SiF_6 and teflon samples previously described with bremsstrahlung of a certain endpoint energy, counting the samples, and then computing the ratios as a function of endpoint energy. This procedure was repeated several times so that a mean ratio with a minimum amount of uncertainty at each endpoint energy could be reported. Because two sets of ratios were determined using two different sample types, the experimental method for each differed slightly. Each method is described separately in the following after a general description of the irradiation and the radioactivity determination procedures which were common to both sets.

The samples were irradiated, in the geometry shown in Figure 15, with the Sagittaire linear accelerator operating in the photon II, or experimental mode. The operation and characteristics of the linac experimental mode have been set forth in the description of the Sagittaire in the Materials section of this chapter. The K_2SiF_6 samples were exposed to bremsstrahlung of endpoint energies from 13 to 23 MeV at integral MeV intervals. The teflon samples were exposed to x-ray beams of endpoint energies ranging from 20 to 32 MeV, also at integral-MeV intervals.

Prior to sample irradiation, the bremsstrahlung beam endpoint energy was chosen at random. Continuous selection of endpoint energies was made possible by the linac modification previously described. The deviation magnet current corresponding to the chosen endpoint energy was

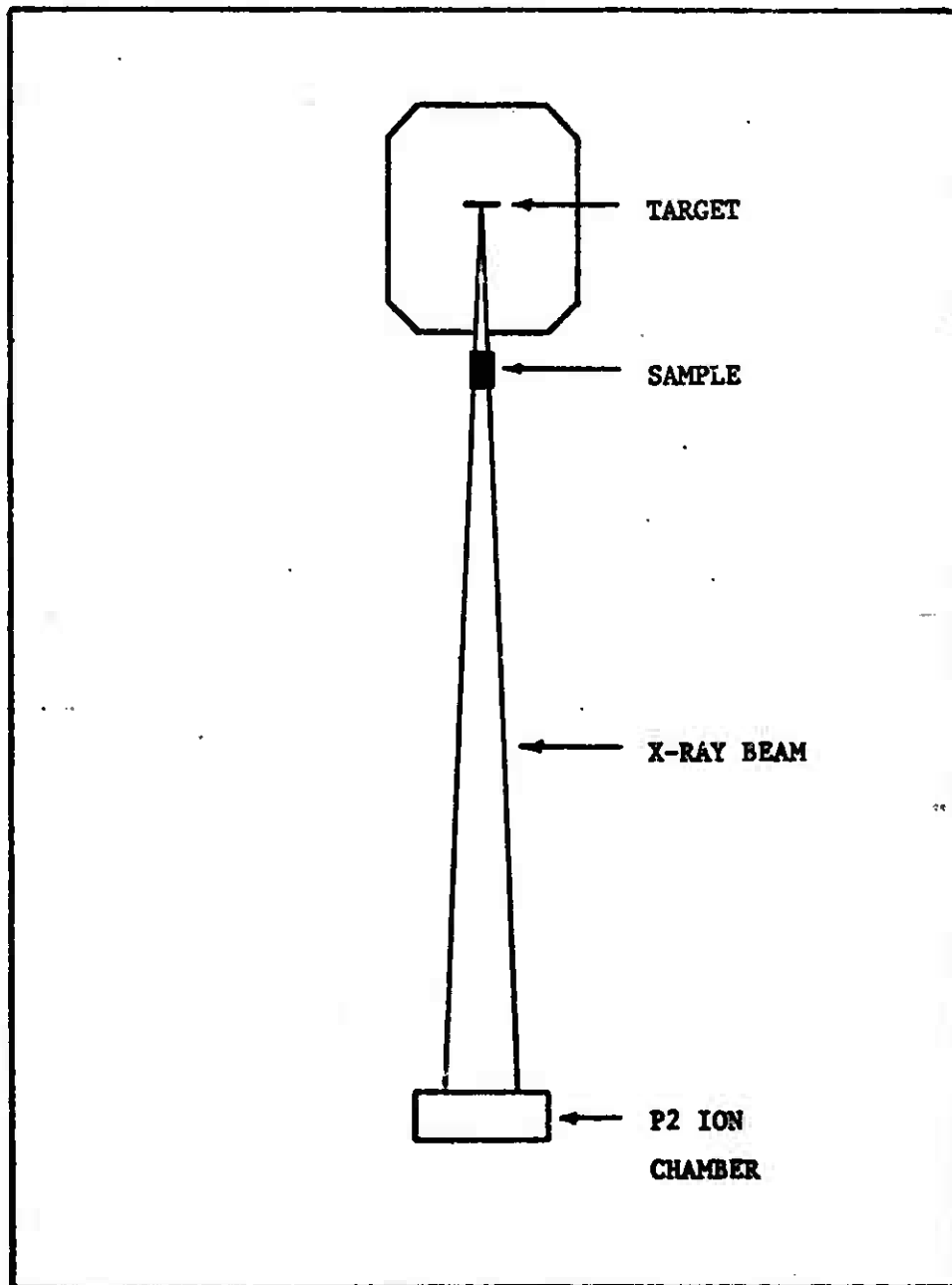


Figure 15. Sample irradiation geometry.

set. This setting established the accelerated electron beam energy. The optimum phase-shifter position, gun current and RF high voltage (RFHV) corresponding to the chosen endpoint energy (Table 3) were also set. In addition, the irradiation and transfer times were set on the timing control module. The sample was then inserted in the linac sample holder. The linac was started and irradiation commenced.

At the end of the irradiation, the monitor units utilized were noted and recorded. The sample was then transferred to the counting room and was inserted in the sample holder near the germanium detector. After expiration of the transfer, or transit, time which was set on timer 2 of the timing control module, the sample was counted. The background-corrected counts were then used to compute the photonuclear ratio at the selected endpoint energy.

The photonuclear ratio (FR) has been defined as the number of photonuclear reactions per target nucleus induced in element 1 of the sample compound divided by the number of photonuclear reactions per target nucleus induced in element 2 of the compound. To determine the number of photonuclear reactions, the activity of the samples was measured.

In both target elements of both samples, the radioisotopes of interest decayed by positron emission with the subsequent emission of 0.511 MeV annihilation gamma rays. It was the 0.511 MeV gamma ray that were counted to determine the amount of radioisotope produced. Since the half-lives of both of the radioisotopes produced in the compound differed significantly (7.63 min ^{38}K vs. 109.8 min ^{18}F in K_2SiF_6 and 20.3 min ^{11}C vs. 109.8 min ^{18}F in teflon), the sample was counted twice to enable determination of the activity of each radioisotope.

The first count contained contributions from both the short-lived and the long-lived radioisotopes. The second count was delayed in time until the shorter-lived radioisotope had decayed very nearly completely (ten half-lives of the shorter-lived isotope). The second count, therefore, was due almost exclusively to the longer-lived radioisotope. Based on the second count, utilizing appropriate decay factors, the contribution of the longer-lived isotope to the first count was calculated. This value was then subtracted from the number of counts measured in the first count to obtain the contribution due to the decay of the shorter-lived isotope.

The procedure described above for determining the activity of each isotope of interest in the sample was followed with both the K_2SiF_6 and the teflon samples. In the K_2SiF_6 experiment the first count was due to the activity of both ^{38}K and ^{18}F , and the second count, obtained after ^{38}K decay, was due almost entirely to the ^{18}F activity. In the teflon experiment, the first measured count contained contributions from both the ^{11}C and ^{18}F activities while the second count, obtained after the ^{11}C had decayed, was due almost entirely to the ^{18}F activity.

The counts mentioned in the foregoing were obtained from the total absorption peak or photopeak. The gross counts in the photopeak were corrected for background to yield net photopeak counts in a manner outlined below. The number of counts in all channels encompassing the photopeak were summed. Background counts were determined by first noting the number of counts in the channels bordering the photopeak where the peak blended into the background continuum. The counts in these channels were then averaged and multiplied by the number of channels in the photopeak to yield the background count. The background count was then sub-

tracted from the sum of the total photopeak counts to yield the net photopeak counts.

The K_2SiF_6 samples were irradiated to bremsstrahlung of endpoint energy ranging from 13 to 23 MeV. One by one, each sample was positioned in the linac sample holder and was irradiated, as described previously, for 2 minutes at a certain endpoint energy. The sample was then transferred to the counting system and allowed to stand for 10 minutes. The delay provided for the decay of any interfering short-lived positron activity such as 6.34 sec ^{26}Al , 4.14 sec ^{27}Si , .93 sec ^{38m}K . The 10-min wait also served to reduce the amount of detector dead time. After the 10-min wait the sample was counted for 1 minute. The counts in the 0.511 MeV photopeak, due to the activity of both ^{38}K and ^{18}F , were then recorded. The sample was then recounted for 1 min 90 minutes after the conclusion of its irradiation and again the 0.511 MeV photopeak counts were recorded. It was assumed that the 90-min delayed count contained only ^{18}F counts since 11.8 ^{38}K half-lives had passed leaving only .03% of the original activity. The entire procedure, which constitutes what is termed a "run," was then repeated for another sample at another endpoint energy.

The K_2SiF_6 photonuclear ratio at a given endpoint energy obtained in a given run is calculated as described below. The net ^{18}F count 10 minutes after irradiation is calculated from the 90-min count through the relation

$$FC_{10} = FC_{90} e^{-\lambda(10)} / e^{-\lambda(90)} \quad (77)$$

where FC_{10} and FC_{90} are the 10-min and 90-min counts corresponding to the ^{18}F activity at 10 min and 90 min respectively. λ is the ^{18}F decay con-

stant ($.00631 \text{ min}^{-1}$). The net 10-min ^{38}K count is obtained by subtracting the net ^{18}F count at 10 min from the measured (^{38}K plus ^{18}F) 10-min count. The net ^{38}K and net ^{18}F counts are then substituted into Eq. (70) to obtain the appropriate photonuclear ratio.

The teflon samples were irradiated with bremsstrahlung of endpoint energy ranging from 20 MeV to 32 MeV. Each sample was positioned, one by one, in the linac sample holder and was irradiated for 3 min at a selected endpoint energy. The sample was then transferred to the counting system and allowed to stand for 10 min to reduce the amount of detector dead time. After the 10-min wait the sample was counted for 1.67 min (100 sec). The counts in the 0.511 MeV photopeak, due to the decay of both ^{11}C and ^{18}F , were then recorded. The sample was recounted for 100 sec 200 minutes after the conclusion of its irradiation and again the 0.511 MeV photopeak counts were recorded. The 200-min count contained almost exclusively ^{18}F counts since 9.85 ^{11}C half-lives had transpired leaving only .11% of the original activity. The entire procedure, or run, was then repeated for another sample at another endpoint energy.

For a given run, the teflon photonuclear ratio at a given endpoint energy was calculated in a fashion similar to that used to calculate the K_2SiF_6 ratios. The net ^{18}F count 10 min after irradiation was calculated from the 200-min count by

$$FC_{10} = FC_{200} e^{-\lambda(10)} / e^{-\lambda(200)} \quad (78)$$

where FC_{10} and FC_{200} are the 10-min and 200-min counts due to ^{18}F activity at 10 min and 200 min respectively. Again λ is the ^{18}F decay constant ($.00631 \text{ min}^{-1}$). The net ^{11}C 10-min count is obtained by subtracting the

net ^{18}F 10-min count from the measured (^{11}C plus ^{18}F) 10-min count. The net ^{11}C and net ^{18}F counts are then substituted into Eq. (70) to obtain the appropriate photonuclear ratio.

The Bremsstrahlung Spectrum

This section describes the numerical analysis method which was used to obtain a functional form for the bremsstrahlung spectra produced by the Sagittaire accelerator. The computational procedure consisted essentially of the following (refer to Fig. 16): 1) the target (thickness D) was divided into n slabs of thickness Δd ; 2) an intrinsic spectrum was assumed for each slab; 3) the photons radiated were attenuated by remaining slabs; 4) the electron energy in the i^{th} slab, T_i , was degraded by interactions in preceding slabs; 5) the number of electrons reaching subsequent slabs was decreased; 6) contributions from each slab were added to form a composite spectrum.

The Sagittaire accelerator target, 7.72 g/cm^2 of tungsten, was divided into 200 slabs, each of thickness 0.0386 g/cm^2 (approximately 0.006 radiation lengths). The bremsstrahlung cross section used to compute the intrinsic spectrum from each slab was Schiff's cross section differential in photon emission angle and energy [Eq. (36)]. The formula employed was in the notation of Hisdal (54) in the rewritten form of Lent and Dickinson (52). For each slab, the intrinsic spectrum was integrated over photon emission angles up to that determined by electron multiple scattering in the slab (54).

The reason for choosing this form of intrinsic spectrum had to do with the chosen slab thickness in combination with the solid angle

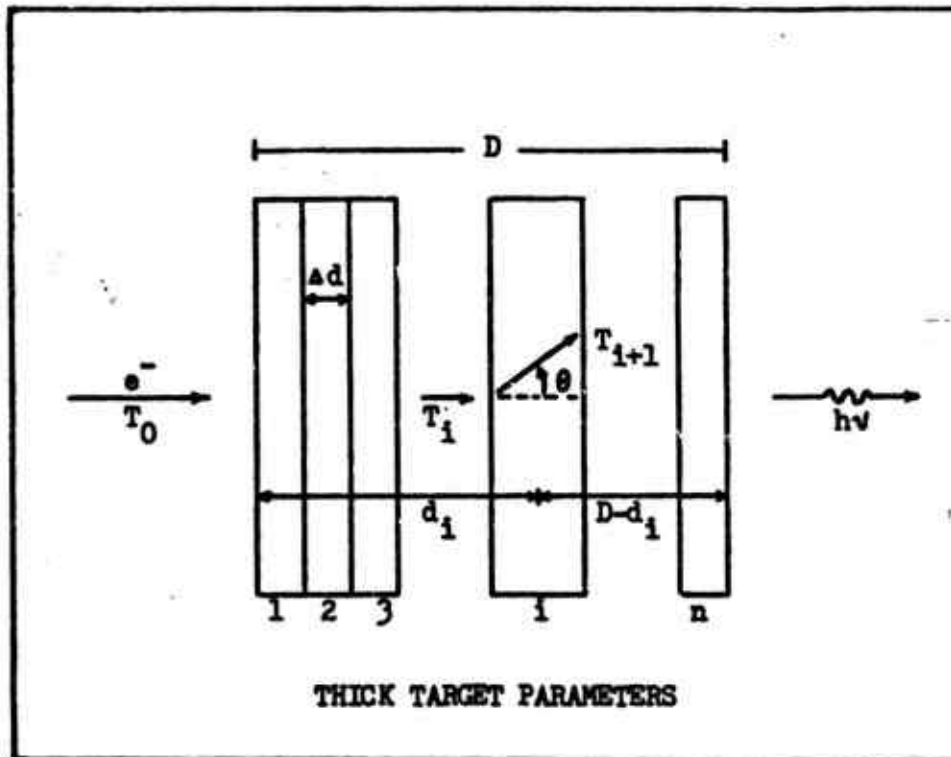


Figure 16. Thick target parameters used in the bremsstrahlung computer program.

subtended by the sample irradiated. The slab thickness had been chosen such that the electron was multiple-scattered prior to radiation. The solid angle subtended by the sample was such that the actual spectrum seen by the sample contained photons emitted at angles up to those determined by multiple-scattering. Under these circumstances, the differential spectrum integrated over photon emission angles up to the multiple-scattering angle represented an appropriate approximation to the actual spectrum to which the sample was exposed (19,54,64,65).

The radiated photons were attenuated by remaining slabs. A factor of the form

$$\alpha_1(h\nu) = \exp[-\mu_1(h\nu)(D - d_1)] \quad (79)$$

was used for this purpose. In Eq. (79), $\alpha_1(h\nu)$ is the photon attenuation factor as a function of photon energy for slab 1, D is the total target thickness and d_1 is the depth of the present slab. $\mu_1(h\nu)$, the total attenuation coefficient of tungsten as a function of photon energy $h\nu$, was obtained by fitting simple quadratic expressions to the total attenuation coefficient for tungsten given by Storm and Israel (66).

The average electron kinetic energy in each slab T_i was determined by energy losses in previous slabs

$$T_i = T_0 - \frac{\Delta d}{2} \left(\frac{dT}{ds} \right)_{T_0} ; i = 1 \quad (80a)$$

$$T_i = T_{i-1} - \frac{\Delta d}{\cos\theta} \left(\frac{dT}{ds} \right)_{T_{i-1}} ; i = 2, 3, \dots, n. \quad (80b)$$

In Eqs. (80), T_i is the average electron kinetic energy in the present

slab, T_{i-1} is the electron kinetic energy in the previous slab, T_0 is the incident electron kinetic energy (endpoint energy), Δd is the slab thickness, and dT/ds is the total mass stopping power of electrons in tungsten. The total mass stopping power was obtained by fitting simple quadratic expressions to the mass stopping power data of Berger and Seltzer (67). The angle Θ is the r.m.e. angle of multiple-scattering according to the Moliere theory (55). The angle of multiple-scattering was calculated using Bichsel's expression (68)

$$\Theta_1^2 = \frac{(.157)(Z^2 + Z)(B - 5.01)\Delta d}{A(T_1^2 + 2m_e c^2 T_1)} \quad (81a)$$

In Eqs. (81), Z and A are the atomic number and atomic mass of the target, respectively, T_1 is the electron kinetic energy in the i^{th} slab (Eqs. 80), m_e is the rest energy of the electron in MeV, Δd is the slab thickness, and B is the Moliere B (68). The value of 5.01 was determined in an experiment (described later in this chapter) in which the angular distribution of the bremsstrahlung beam of the Sagittaire was investigated to estimate the electron multiple-scattering distribution in the target.

In a slab, the actual angle into which an electron is multiple-scattered depends also on the multiple-scattering angle of the previous slab (53). Thus, for a slab i , the angle of multiple-scattering Θ was obtained from the relation

$$\Theta^2 = \Theta_{i-1}^2 + \Theta_i^2 \quad (81b)$$

where Θ_i^2 is given by Eq. (81a) and Θ_{i-1}^2 is the square of the angle of multiple-scattering of the previous slab. The angles were summed in quadrature because they essentially represent measures of dispersion.

In latter slabs of the target, the electrons undergo a diffusion process in which the electron angular distribution remains approximately $\cos^2\theta$ for which $\theta^2 = 0.5388$ radians (69). In these slabs, θ [as given by Eq. (81b)] was limited to 0.734 radians (53).

The fraction of the incident electron flux which reached the i^{th} slab was calculated with the following formulas due to Ebert (70).

$$\tau_i = \exp[-a(\Delta d/R)^b] \quad (82)$$

$$e = (1 - 1/b)^{1-b} \quad (82a)$$

$$b = [387T_0/1.000075ZT_0^2]^{.25} \quad (82b)$$

$$R = .565 \left(\frac{125}{Z + 112} \right) T_0 - .423 \left(\frac{175}{Z + 162} \right) \quad (82c)$$

In Eqs. (82), τ_i is the fraction of the incident electron flux that reaches the i^{th} slab and R is the extrapolated range. All remaining variables have been defined previously. These equations resulted from curves fit to experimental data for monoenergetic electrons up to 12 MeV in foils of select elements up to uranium (70). The assumption was made here that these relations hold up to about 30 MeV.

The final photon spectrum was obtained by summing the photon contributions from each slab.

$$N(h\nu) = \sum_{i=1}^n N_i(h\nu)\tau_i \quad (83)$$

In Eq. (83), $N(h\nu)$ is the total number of photons of energy $h\nu$ in the

spectrum. The summation is over all slabs. τ_i is the transmission factor of the i^{th} slab [Eqs. (82)], and $N_i(h\nu)$ is the number of photons of energy $h\nu$ contributed by the i^{th} slab

$$N_i(h\nu) = d\sigma(h\nu)n_i\alpha_i(h\nu). \quad (83a)$$

In Eq. (83a), $d\sigma(h\nu)$ is the bremsstrahlung cross section in cm^2 [Eqs. (36)], $\alpha_i(h\nu)$ is the photon attenuation factor as a function of photon energy for the i^{th} slab [Eq. (79)], and n_i is the number of target nuclei per cm^2 in the i^{th} slab

$$n_i = \frac{N_A}{A} \rho \frac{\Delta d}{\cos\Theta_i} \quad (83b)$$

where N_A is Avogadro's number, A is the atomic mass of the target, ρ is the density of the target, Δd is the slab thickness, and Θ_i is the r.m.s. angle of multiple-scattering [Eqs. (81)].

In most linear accelerators, the electrons producing bremsstrahlung possess a finite distribution of energies centered about a mean electron energy. In the case of the Sagittaire accelerator, electrons of energies within $\pm 2\%$ of a mean electron energy are transmitted by the energy-defining slit (94). The bremsstrahlung computer program was modified to account for this fact. At any given endpoint energy T_0 , the spectrum was assumed to consist of photons produced by electrons of initial energy T_0 , $T_0 - 2\%T_0$, and $T_0 + 2\%T_0$. The endpoint energy distribution was assumed to be a Gaussian of $4\%T_0$ full-width-half-maximum. Relative weights of .25, .50, and .25 thus were given to the spectra produced by electrons of energy $T_0 - 2\%$, T_0 , and $T_0 + 2\%$, respectively.

A computer program, written in Fortran and incorporating the above expressions, was used to produce the bremsstrahlung spectra approximations required for this study. A listing of this program is provided in Appendix E.

Electron Multiple-Scattering

High-energy bremsstrahlung is emitted at small angles with respect to the direction of the incident electron. An order of magnitude estimate of this angle is (19)

$$\phi = u/E_0 \text{ radians} \quad (84)$$

where ϕ is the angle between the direction of the radiation photon and the initial direction of the radiating electron, u is the rest energy of the electron, and E_0 is the total electron energy. For a bremsstrahlung beam of 25 MeV endpoint, ϕ is of the order of 0.02 radians. In an experiment where the angular distribution of high-energy bremsstrahlung intensity is measured, the electron multiple-scattering distribution can be estimated if the assumption is made that bremsstrahlung is emitted at angles small compared to the angles of electron scattering. Such an experiment was performed to examine the ability of Eqs. (81) of appropriately estimating the angle of multiple-scattering.

Eleven teflon samples were placed in a straight line on a plane parallel to and 75 cm from the bremsstrahlung target. The samples were spaced 2 cm apart with the central sample located on the central axis of the bremsstrahlung beam. The samples were exposed to a 25 MeV photon II beam for 5 min and were counted for 60 sec with the germanium detector. The same procedure used in the photonuclear ratios experiment for esti-

measuring the ^{11}C activity was followed. The ^{11}C decay factor was applied to each count to calculate the ^{11}C activity of each sample at the time the irradiation stopped. The activity of each sample was divided by the sample weight to yield a "specific activity" for each. This activity was then plotted as a function of the sample relative position during irradiation and a Gaussian curve was fitted to the plot using a non-linear regression technique (71). Thus, a distribution of the intensity of photons possessing energies between 18.7 MeV [$^{12}\text{C}(\gamma, n)^{11}\text{C}$ reaction threshold] and 25 MeV as a function of distance from central axis (and hence angle from the initial electron direction) was obtained.

A weighted effective angle of multiple-scattering was calculated from the bremsstrahlung computer program for the target slabs contributing photons of energy greater than 18.7 MeV. The weights were obtained from the electron energy in the slab [Eqs. (80)] and from the relative ^{11}C yield as a function of energy measured in the photonuclear ratio experiment. This weighted effective angle was then compared to the standard deviation of the Gaussian distribution obtained from the regression fit and a normalization factor F_n was calculated

$$F_n = \frac{\phi_{\text{eff}}}{\phi_{\text{meas}}} \quad (85)$$

where ϕ_{eff} is the weighted effective angle of multiple-scattering (1/e width of the distribution) and ϕ_{meas} is the standard deviation of the Gaussian fit. The (B - X) factor of Eq. (81a) was then modified in a manner similar to that of Hanson (72).

The $^{27}\text{Al}(\gamma, 2p)^{25}\text{Na}$ Cross Section

The aluminum samples described in the Materials section of this chapter were used to obtain the $^{27}\text{Al}(\gamma, 2p)^{25}\text{Na}$ yields as a function of bremsstrahlung endpoint energy. Yields were measured at endpoint energies from 25 to 33 MeV in 0.25 MeV increments. Thus, a yield curve consisted of 33 yield points. A total of five yield curves was obtained and mean yields were computed. This section describes the experimental procedure followed to obtain the $^{27}\text{Al}(\gamma, 2p)^{25}\text{Na}$ yield curve and the method of determining the reaction cross section.

Prior to the start of this experiment, the resistance value of the variable resistor of the RC circuit of the radiation monitor system was set such that the time constant (RC) was inversely proportional to the ^{25}Na decay constant. For a capacitance of 10.096 μF and a decay constant of 0.01155 sec^{-1} , the required resistance was 8.57 $\text{M}\Omega$. The behavior of the RC system was checked initially and at the beginning of each experimental session. The capacitor was charged to a certain value and the decay of charge was observed as a function of time to determine whether the potential was decreasing with rate constant $RC = 1/\lambda$. The potential drop half-time was measured with a stopwatch. After the initial setting of the resistance value, no further adjustments were required as the measured potential drop half-times were consistently reproducible to within 1%.

Before the irradiation of the aluminum samples, the capacitor of the radiation monitor system was shorted to remove any potential. The samples were irradiated in the irradiation geometry shown in Figure 15. The bremsstrahlung endpoint energy was chosen at random and the approp-

riate irradiation parameters (Table 3) were set on the linac. Sample irradiation time was 2 min. Immediately following irradiation, the voltage reading on the electrometer was noted and recorded and the sample was retrieved from the irradiation room. After a delay of 55 sec, the samples were counted for 195 sec with the germanium detector spectrometer system. The counts in the photopeaks corresponding to the 0.975 and 1.612 MeV gamma rays were computed as described in the Photonuclear Ratios section of this chapter. Another endpoint energy was chosen and the procedure was repeated until a complete yield curve was obtained. Five yield curves were measured in this manner.

At each endpoint energy in a yield curve, a normalized yield (number of reactions per volt) was calculated using Eq. (53). The constant K of Eq. (53) was obtained from the calibration of the germanium detector, from the decay characteristics of ^{25}Na , and from an $e^{-\mu r}$ (r = sample radius) estimate of sample self-absorption. C is the net number of photopeak counts due to a particular gamma ray. A mean $Y_n(T)$ was calculated based on the two estimates of yield made corresponding to each of the gamma rays counted.

A total yield in the entire energy range of each yield curve was determined by summing the individual normalized yields

$$Y_T = \sum_{i=1}^n \hat{Y}_n(T_i) \quad (86)$$

where Y_T is the total yield, $\hat{Y}_n(T_i)$ is the normalized yield at endpoint energy T_i , and n is the number of points on the yield curve. For each of the five yield curves, a total yield Y_T was obtained. A mean total yield,

\bar{Y}_T , was then calculated from all the yield curves

$$\bar{Y}_T = \frac{1}{m} \sum_{j=1}^m Y_{Tj} \quad (87)$$

where Y_{Tj} is total yield of the j^{th} yield curve and m is the total number of yield curves. A normalization factor, Y_{fj} , was calculated for each yield curve by dividing its total yield into the mean total yield

$$Y_{fj} = \bar{Y}_T / Y_{Tj} \quad (88)$$

where Y_{fj} and Y_{Tj} are the normalization factor and total yield, respectively, of the j^{th} yield curve. Each normalized yield point of a given yield curve was then multiplied by its corresponding normalization factor

$$Y_{nj}(T_1) = Y_{fj} \hat{Y}_{nj}(T_1) \quad (89)$$

where $Y_{nj}(T_1)$ is the corrected normalized yield point at endpoint energy T_1 in the yield curve j , Y_{fj} is the normalization factor of the yield curve j , and $\hat{Y}_{nj}(T_1)$ is the uncorrected yield point at endpoint energy T_1 in the yield curve j . Note that this normalization procedure preserves the shape of the yield curve while correcting it for any possible variations in experimental conditions from one experiment session to the next. The final yield curve was obtained by averaging the corrected yields at each endpoint energy over all yield curves

$$\bar{Y}_n(T_1) = \frac{1}{m} \sum_{j=1}^m Y_{nj}(T_1) \quad (90)$$

where $\bar{Y}_n(T_1)$ is the mean normalized yield at endpoint energy T_1 .

In order to determine the cross section of the $^{27}\text{Al}(\gamma, 2p)^{25}\text{Na}$ reaction, reduced yields were calculated from the mean normalized yields. These reduced yields were calculated using Eqs. (13) and (15). The total energy in the bremsstrahlung spectrum $E(T)$ was obtained from the bremsstrahlung computer program. The sample transmission factor $f_t(T)$ was experimentally determined and the monitor response $R(T)$ was obtained from Reference 56. The $^{27}\text{Al}(\gamma, 2p)^{25}\text{Na}$ reaction cross section was obtained with the Cook (34) Least Structure computer program from the calculated reduced yields and from the bremsstrahlung spectra obtained with the bremsstrahlung computer program (Appendix E).

CHAPTER IV

RESULTS

Photonuclear Ratios

The production of unique photonuclear yield ratios as a function of bremsstrahlung endpoint energy in a simple manner required that the yield of photonuclear reactions induced in element 1 of the sample remain fairly constant over a certain energy range while the yield of photonuclear reactions induced in element 2 of the sample increase over the same energy range. This requirement was fulfilled by the K_2SiF_6 and teflon samples as shown in Figure 17. The yield curves of the figure have been normalized so that all could be presented on the same graph. As seen in Figure 17, the $^{19}F(\gamma,n)^{18}F$ reaction yield remains fairly constant while the $^{39}K(\gamma,n)^{38}K$ and $^{12}C(\gamma,n)^{11}C$ reaction yields increase. The shape of the yield curves and their relative placement on the endpoint energy axis follows from shape and location on the photon energy axis of the cross sections for the photonuclear reactions contributing to the ratios. These are shown in Figure 18 (40,73-77). The $^{19}F(\gamma,n)^{18}F$ reaction threshold is 10.4 MeV (78); the cross section peaks at approximately 4 mb at about 12 MeV (73). The $^{39}K(\gamma,n)^{38}K$ reaction threshold is 13.1 MeV (78); the cross section peaks at about 10 mb around 20 MeV (74-76). The $^{12}C(\gamma,n)^{11}C$ reaction threshold is 18.7 MeV (78); the cross section peaks at about 9 mb

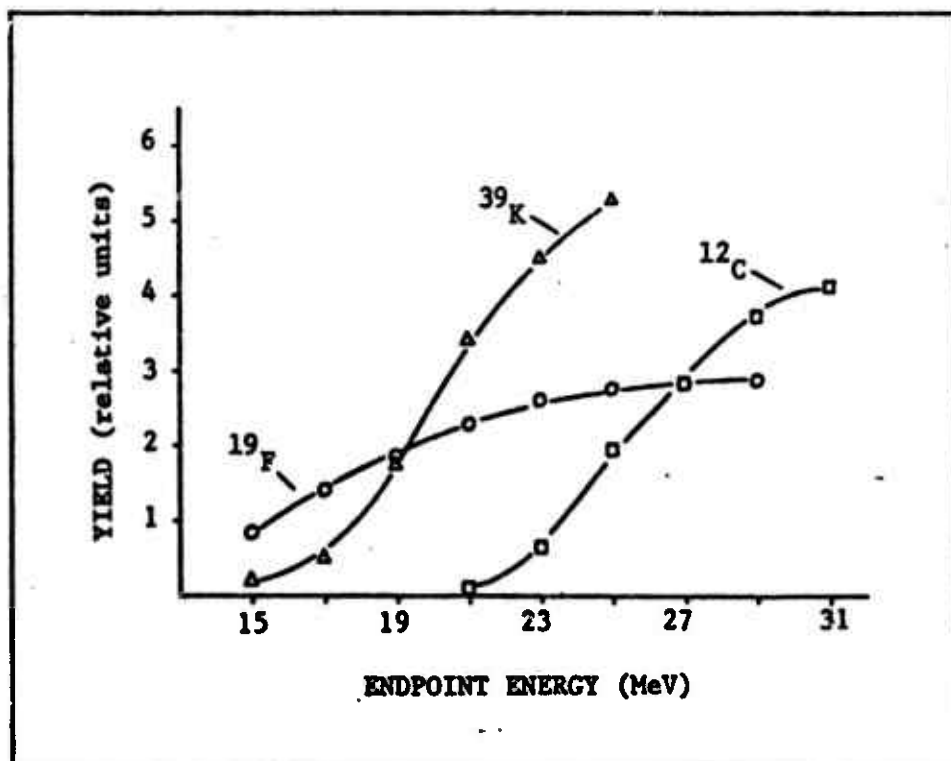


Figure 17. Relative yields of the (γ, n) reaction in the ^{19}F , ^{39}K , and ^{12}C isotopes.

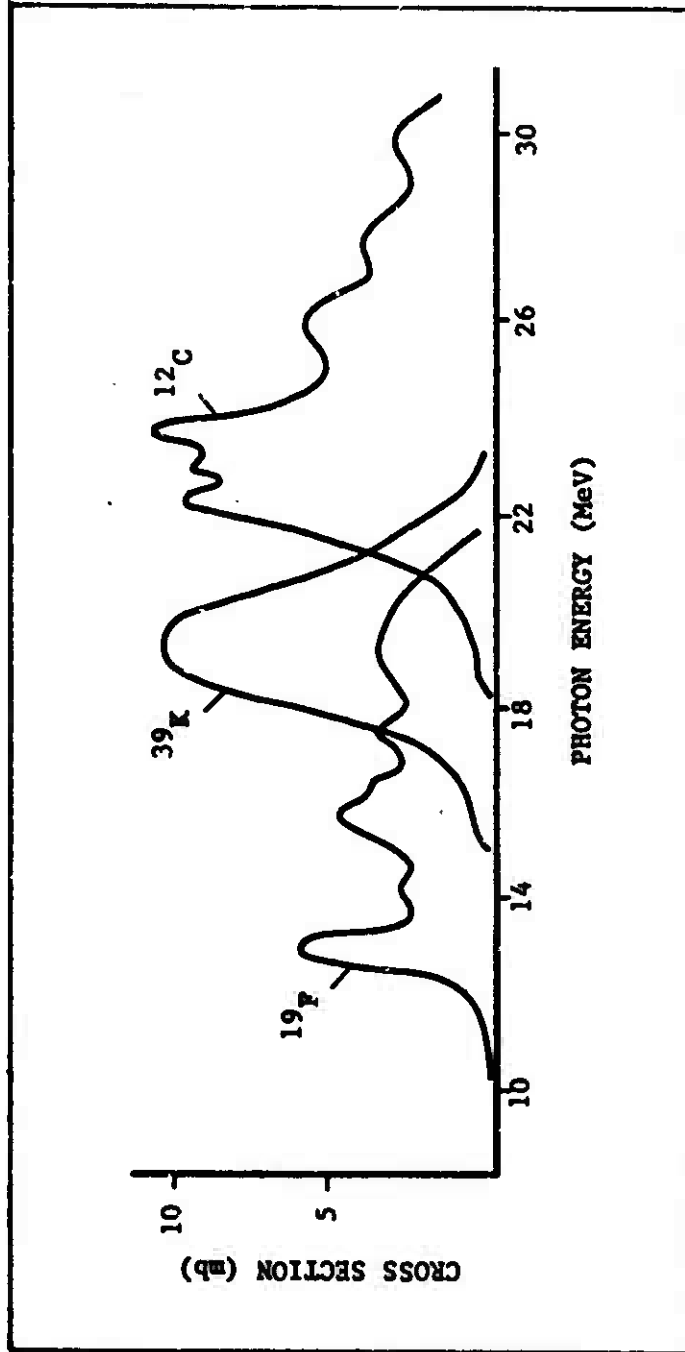


Figure 18. The (r,n) cross sections in ^{19}F , ^{39}K , and ^{12}C .

around 24 MeV (40,77).

Photonuclear yield ratios were computed using Eq. (70). Potassium and fluorine counts used to compute the K_2SiF_6 ratios typically ranged from about 4,000 to 11,000 counts. Figure 19 shows the decay over time of a K_2SiF_6 sample exposed to 20 MeV bremsstrahlung. The presence of the shorter-lived ^{38}K radioisotope and the longer-lived ^{18}F radioisotope is evident. Carbon and fluorine counts used to compute the teflon ratios typically ranged from about 15,000 to 30,000 counts. The decay over time of a teflon sample exposed to 25 MeV bremsstrahlung is shown in Figure 20. The presence of the shorter-lived ^{11}C and the longer-lived ^{18}F is also apparent.

Mean photonuclear yield ratios were computed by averaging the ratios obtained in experimental runs performed at the same endpoint energy. Table 7 shows a breakdown of the number of runs contributing to the mean ratio at each endpoint energy. Runs were repeated a greater number of times at endpoint energies in the region where the ratios were changing most rapidly. Fewer runs were performed at energies where the ratios were slowly changing.

The photonuclear yield ratios obtained as a function of bremsstrahlung endpoint energy are presented in Tables 8 and 9 and are shown graphically in Figures 21 and 22. Evident in Figures 21 and 22 is the sensitivity (percent change of ratio per MeV) of the photonuclear yield ratios to endpoint energy change. The maximum sensitivity of the K_2SiF_6 ratios is 43% per MeV at 19 MeV. The maximum sensitivity of the teflon ratios is 41% per MeV at 24 MeV. Thus, for a given accelerator target and amount of filtration, the photonuclear yield ratios are quite good

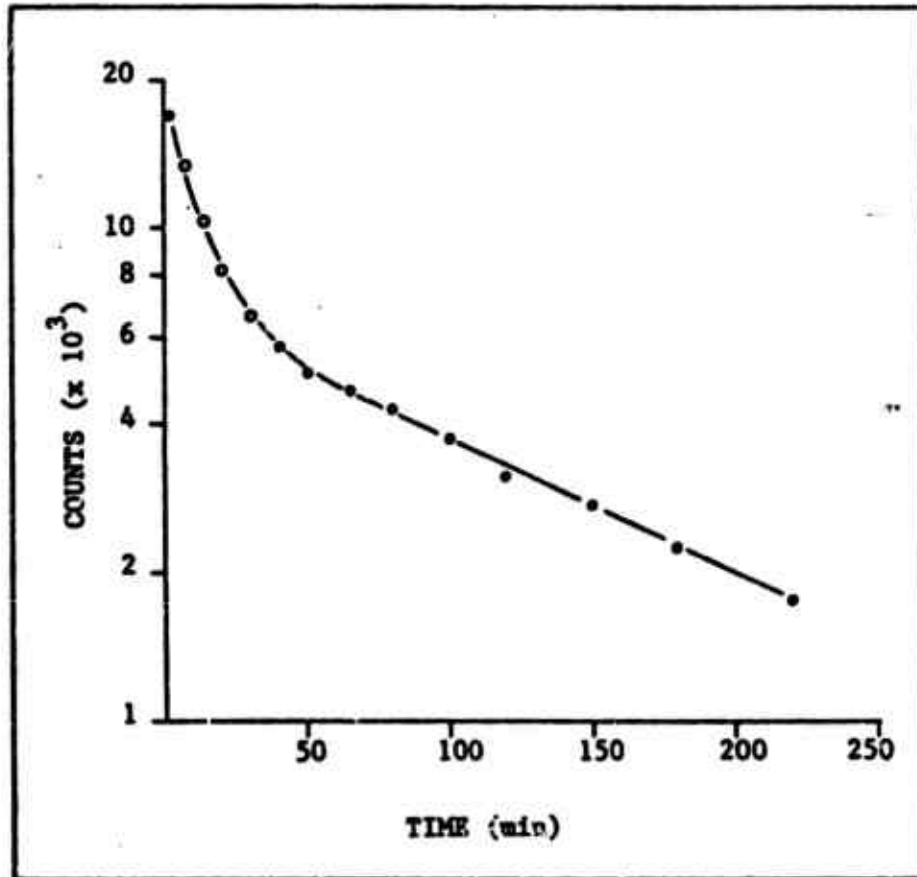


Figure 19. K_2SiF_6 sample decay.

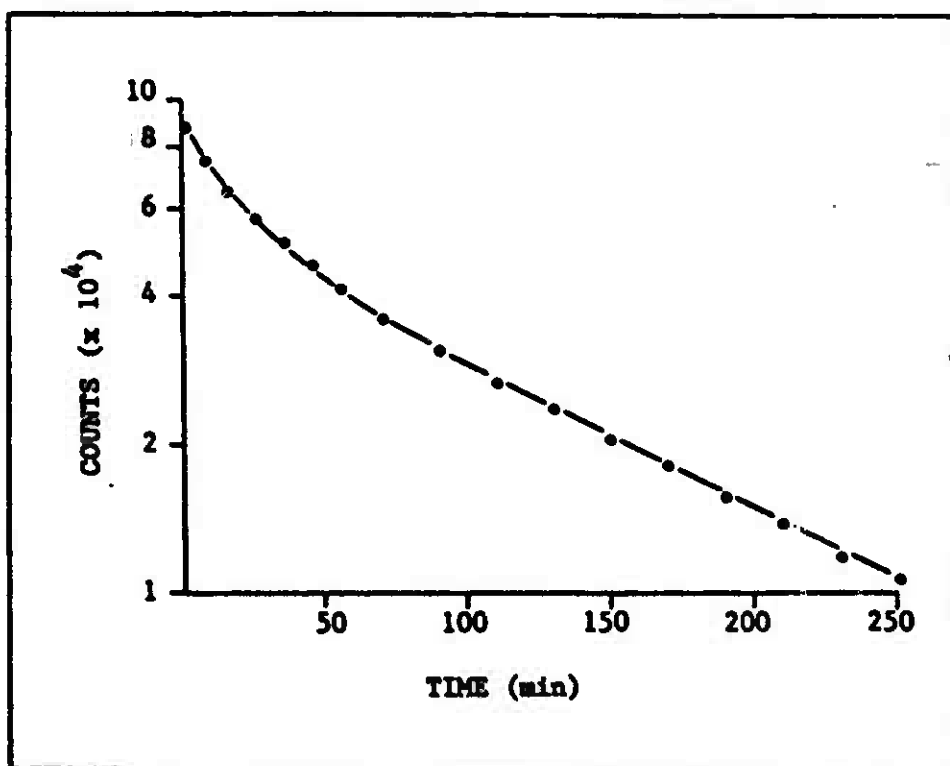


Figure 20. Teflon sample decay.

Table 7Experimental runs used to compute photonuclear ratios

K_2SiF_6 Ratios		Teflon Ratios	
Energy (MeV)	# Runs	Energy (MeV)	# Runs
13	1	20	2
14	5	21	3
15	5	22	3
16	5	23	4
17	7	24	4
18	6	25	4
19	6	26	3
20	5	27	5
21	5	28	4
22	4	29	3
23	3	30	4
		31	3
		32	3

Table 8K₂SiF₆ Ratios *

Endpoint (MeV)	Photon II Ratio
13	0
14	.029 (.019)
15	.074 (.006)
16	.093 (.010)
17	.151 (.016)
18	.235 (.016)
19	.306 (.029)
20	.438 (.013)
21	.515 (.016)
22	.641 (.032)
23	.641 (.016)

*Ratios are mean values, numbers in parentheses are standard errors of the means.

Table 9Teflon Ratios *

Endpoint (MeV)	Photon II Ratio
20	0
21	.002 (.002)
22	.032 (.004)
23	.093 (.006)
24	.172 (.006)
25	.243 (.004)
26	.302 (.002)
27	.354 (.006)
28	.393 (.008)
29	.460 (.004)
30	.484 (.006)
31	.514 (.008)
32	.516 (.010)

*Ratios are mean values, numbers in parentheses are standard errors of the means.

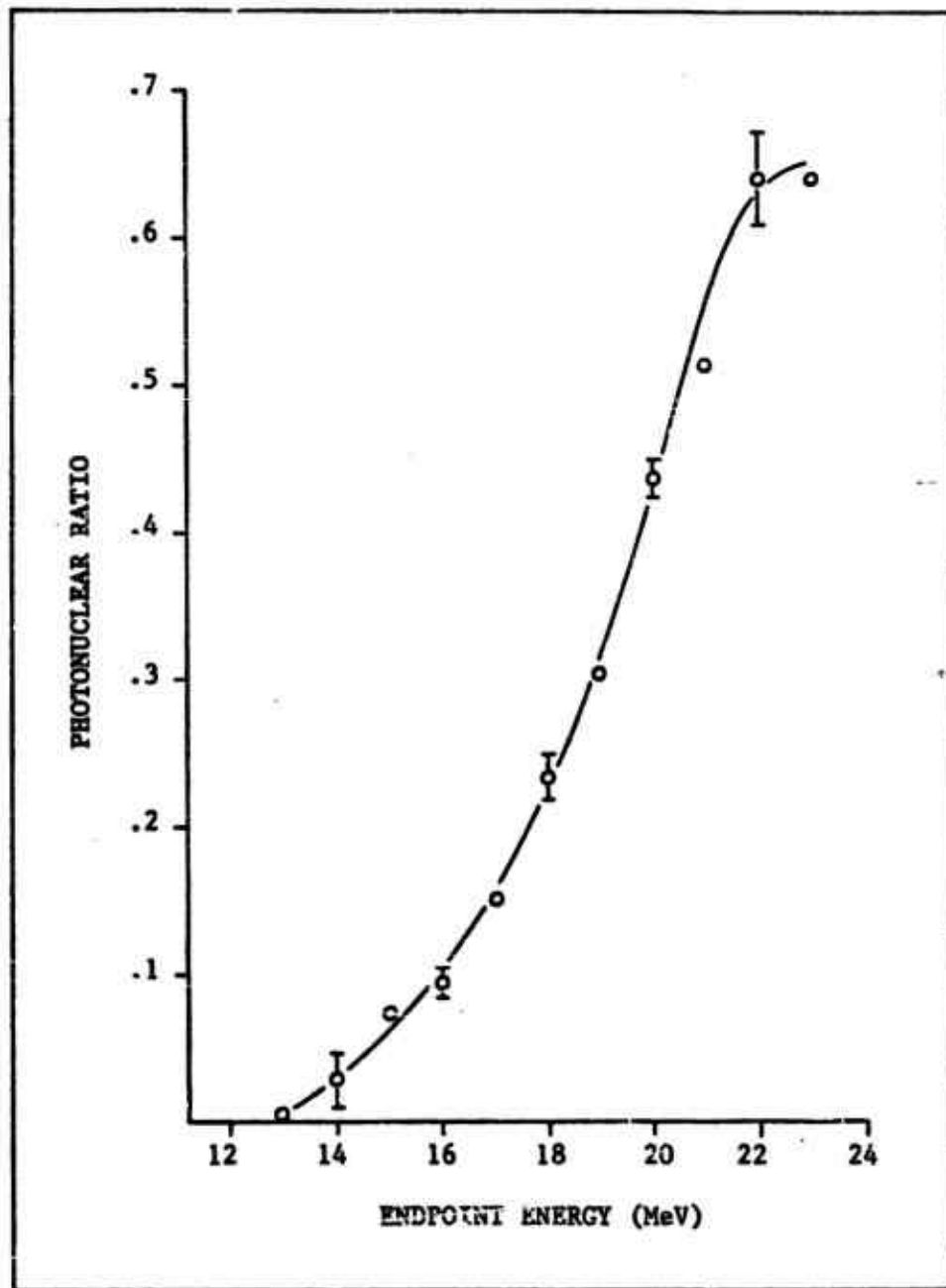


Figure 21. K_2SiF_6 photonuclear ratios.

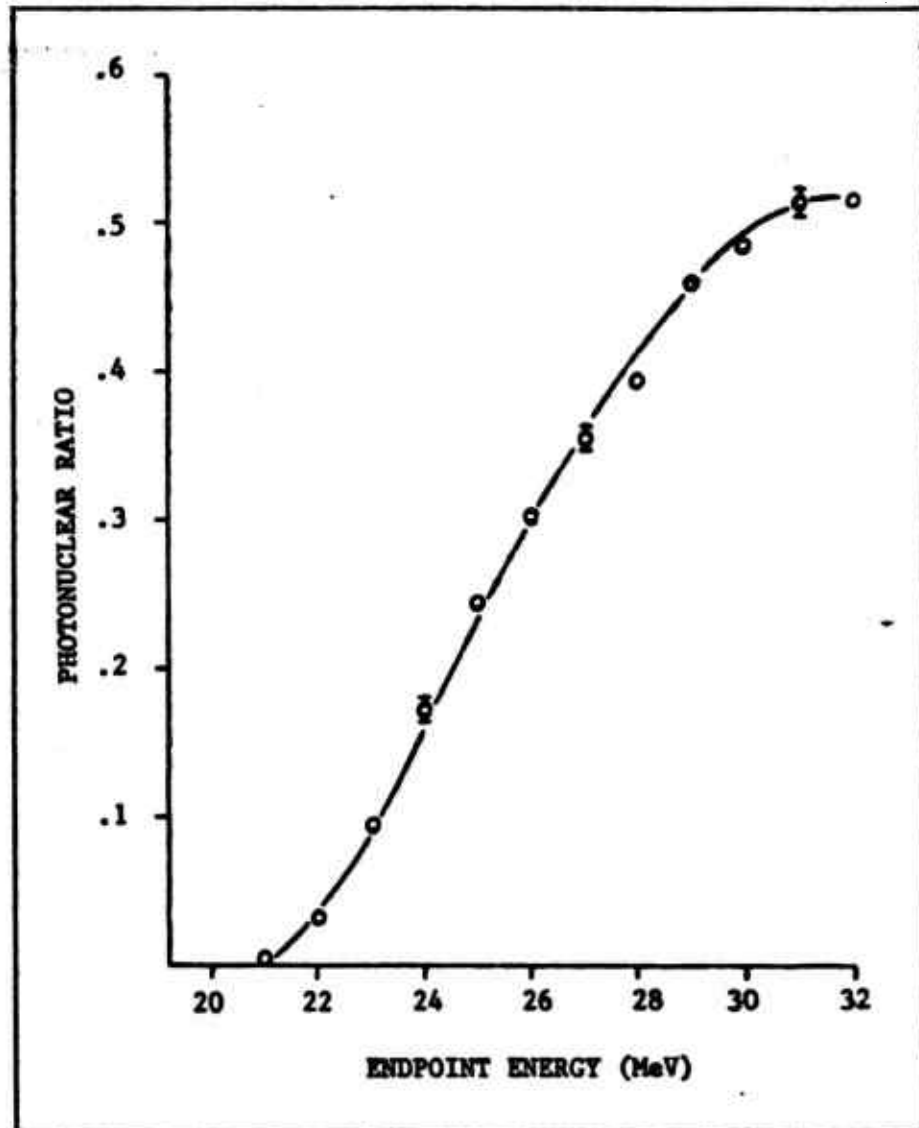


Figure 22. Teflon photonuclear ratios.

indicators of bremsstrahlung endpoint and hence accelerator energy.

The photonuclear yield ratios were found to be sensitive to the amount of filtration in the bremsstrahlung beam. When the lead flattening filter (2.8 cm thick at center) was inserted in the beam, the ratios were found to decrease as shown in Table 10. As seen in this table, the percent reduction increases with increasing endpoint energy. This phenomenon has to do with the relative proportion of higher- and lower-energy photons in the bremsstrahlung spectrum. It is a well-known fact that lead filtration softens high-energy x-ray beams (14). The increase in the relative number of lower-energy photons increases the relative ^{18}F yield. The decreased number of higher-energy photons decreases the relative ^{38}K and ^{11}C yields. These result in decreased ratios. In the lower portion of the energy range of the K_2SiF_6 and teflon ratio curves, ratios are practically unaffected by the addition of the flattening filter. This may follow from the fact that in the lower energy range there is very little contribution from the relative ^{38}K and ^{11}C yields. This would seem to indicate that the decrease of ratios with increasing filtration is due more to the decrease of higher-energy photon availability than to the relative increase of lower-energy photons. This can be substantiated since the fluorine threshold is well above the energy for the minimum μ for Pb.

The influence of sample size on the teflon photonuclear ratio was also investigated. Samples of teflon rod 0.5, 0.75, and 1.0 inch in diameter were exposed to 25 MeV bremsstrahlung and ratios were computed. The resultant ratios were not statistically different (standard deviations overlapped) although the larger (1.0-inch-diameter) sample exhibited a

Table 10

Effect of Filtration
on Photonuclear Ratios

Endpoint Energy	Reduction of K_2SiF_6 ratio	Reduction of teflon ratio
17	2%	
19	5.6%	
21	9.6%	
23		10.7%
25		14.0%
27		15.3%
29		15.4%

slightly lower (by 4%) ratio. It is very possible that larger sample sizes may in fact result in different ratios. Thick-target bremsstrahlung beams contain relatively fewer high-energy photons at larger angles from the incident electron direction (51). The limited increased angle sampled in this experiment by the larger teflon rod was not sufficient to establish this possible cause, however.

The presence of possible interference peaks in the vicinity of the 0.511 MeV photopeaks used for ratio determination was not observed. Thus, photonuclear ratios could be measured with confidence using a NaI(Tl) detector. Possible interference from the β^+ decay of ^{62}Cu and ^{64}Cu which may be produced in the copper present in the aluminum can of the K_2SiF_6 samples was not noted. The 1.173 and 1.346 MeV gamma rays of ^{62}Cu and ^{64}Cu , respectively, could not be seen in the spectra.

The Bremsstrahlung Spectrum

The accuracy of the thick-target bremsstrahlung calculation in predicting spectral shape is best illustrated by comparing the results of the calculation to experimentally-measured spectra. Unfortunately, very few experimental determinations of bremsstrahlung spectra produced by electrons of energies from about 20 to 35 MeV have been reported in the literature. The calculations performed in this work were compared to the 21 MeV thick-target spectrum measured by O'Dell (79). The present calculations also are compared to other calculations (51,53) which attempted to simulate the O'Dell spectrum. O'Dell measured the spectra produced in a composite 0.490 g/cm^2 tungsten - 0.245 g/cm^2 gold radiator by electrons with energies between 5 and 21 MeV. His experimental method consisted of measuring the time of flight of neutrons produced by the ${}^2\text{H}(\gamma, n){}^1\text{H}$ reaction

in a heavy-water target (79). The highest-energy spectrum was chosen for comparison purposes because it was closest to the bremsstrahlung endpoint energies of interest in this work.

Figure 23 compares the result of the monoenergetic endpoint calculations of this work, indicated by the solid line, to that of Berger and Seltzer (51), indicated by the squares. The agreement is quite good although the computational procedure of Berger and Seltzer is quite different from the calculation performed here. Berger and Seltzer's computation was basically a Monte Carlo simulation. They used the intrinsic bremsstrahlung cross section of Olsen and Maximon at small values of screening parameter and the cross section of Seuter at large values of screening parameter (51; see also 46). The computation of this work was a numerical analysis calculation; the Schiff cross section, differential in photon emission angle and energy (20), was used regardless of the value of screening parameter (the Schiff cross section assumes full screening).

Figure 24 compares the monoenergetic endpoint calculation performed here (solid line) to the calculation of Ferdinande (53), shown by the circles. Agreement is good except at the spectrum tip. Ferdinande's intrinsic cross section was the extreme relativistic Bethe-Heitler cross section integrated over photon emission angle. He approximated the angle of photon emission with a Gaussian fit to the calculation of bremsstrahlung mean square angles performed by Stearns (80). The increased number of photons in the tip of the Ferdinande spectrum may be due to his choice of intrinsic cross section. The extreme relativistic Bethe-Heitler cross section, with screening and Coulomb corrections, contains a larger number of photons in the tip than does the Schiff cross section (81). In the

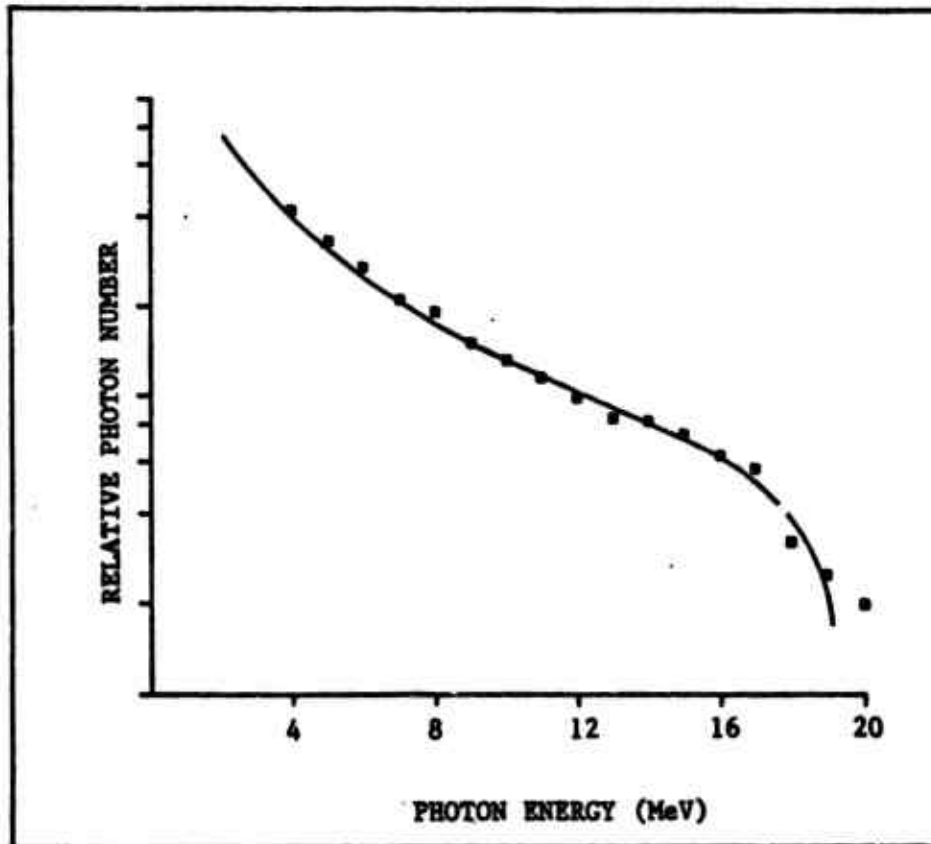


Figure 23. Comparison of the O'Dell spectrum calculated in this work (solid line) with the spectrum of Berger and Seltzer (51). Spectra have been normalized at mid-spectrum.

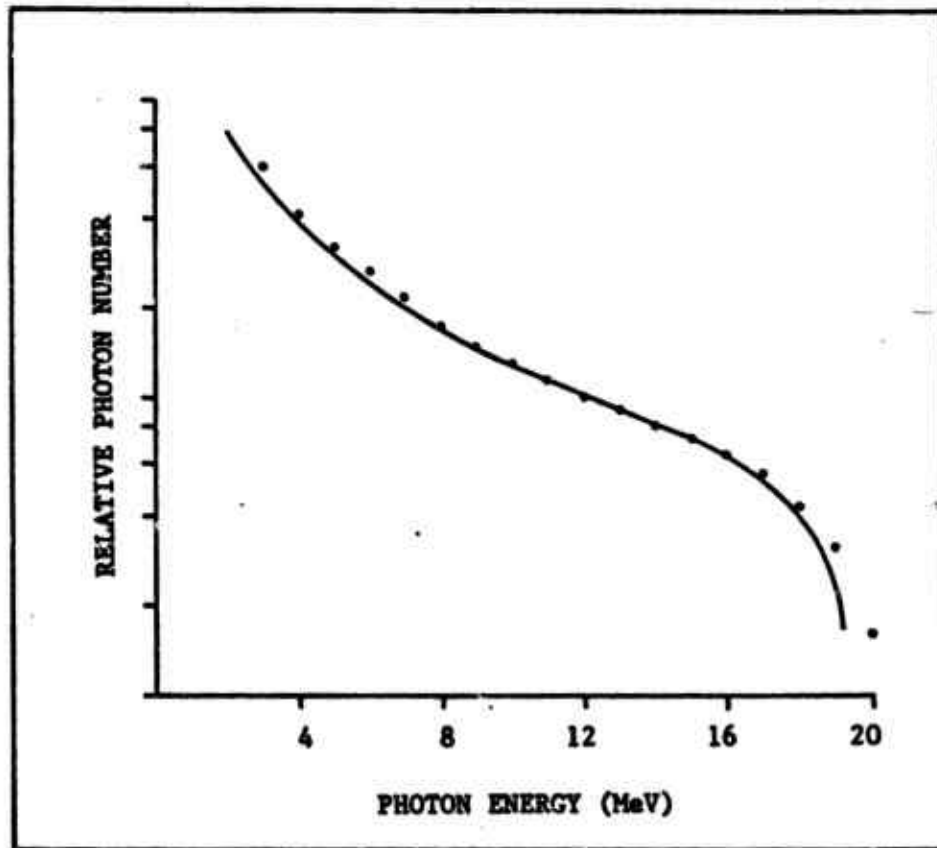


Figure 24. Comparison of the O'Dell spectrum calculated in this work (solid line) with the spectrum of Ferdinande (53). Spectra have been normalized at mid-spectrum.

case of Ferdinande's work it is not clear, however, why an extreme relativistic cross section, assumed valid at very large endpoint energies, would be used in the energy range from 5 to 21 MeV. Also unclear is the reason for using an integrated-over-angle cross section and an approximated angle of photon emission based on calculations performed for 50 to 300 MeV bremsstrahlung (the Stearns' calculations).

The spectrum resulting from the calculations performed in this work are, finally, compared to the experimental data of O'Dell (79) in Figure 25. The solid line represents the monoenergetic endpoint calculation, the dotted line represents the calculation with a $\pm 3\%$ energy spread (79), and the triangles represent the experimental data of O'Dell. The points were obtained at integral MeV photon energies from the smooth curve drawn by the authors through their experimental points. The error bars shown on selected points were obtained from the same curve. Although the present calculation appears to underestimate the mean number of photons in the tip, the calculated spectrum is within the error bars of the experimental points. The $\pm 3\%$ correction shows a marked improvement over the uncorrected calculation. It should be noted that Ferdinande's calculation comes closest to estimating the shape of O'Dell's experimental spectrum. However, recall that Ferdinande assumes an extreme relativistic cross section containing more photons in the tip than does the Schiff cross section, used here.

Figure 26 shows the shapes of the flattened (photon I) and unflattened (photon II) 25 MeV bremsstrahlung beams of the Sagittaire linear accelerator as predicted by the thick-target bremsstrahlung calculations of this work. The effect of the lead flattening filter (photon I) is

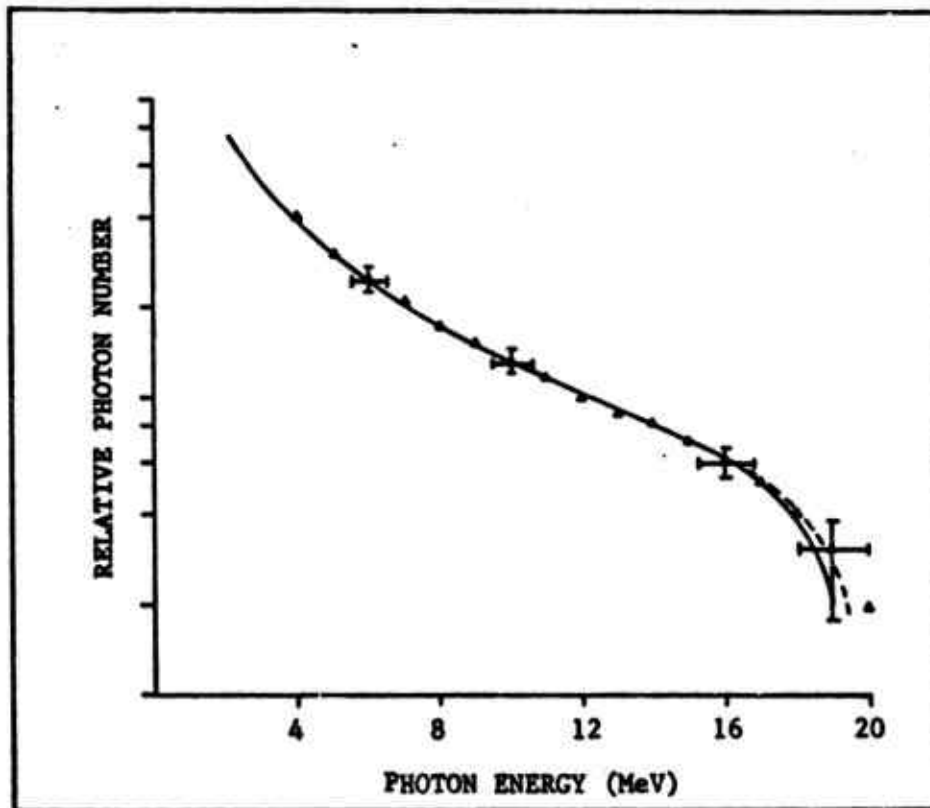


Figure 25. Comparison of the O'Dell spectrum calculated in this work (solid line) with the experimental data of O'Dell (79). Spectra have been normalized at mid-spectrum. The dotted line shows the effect of electron-energy spread.

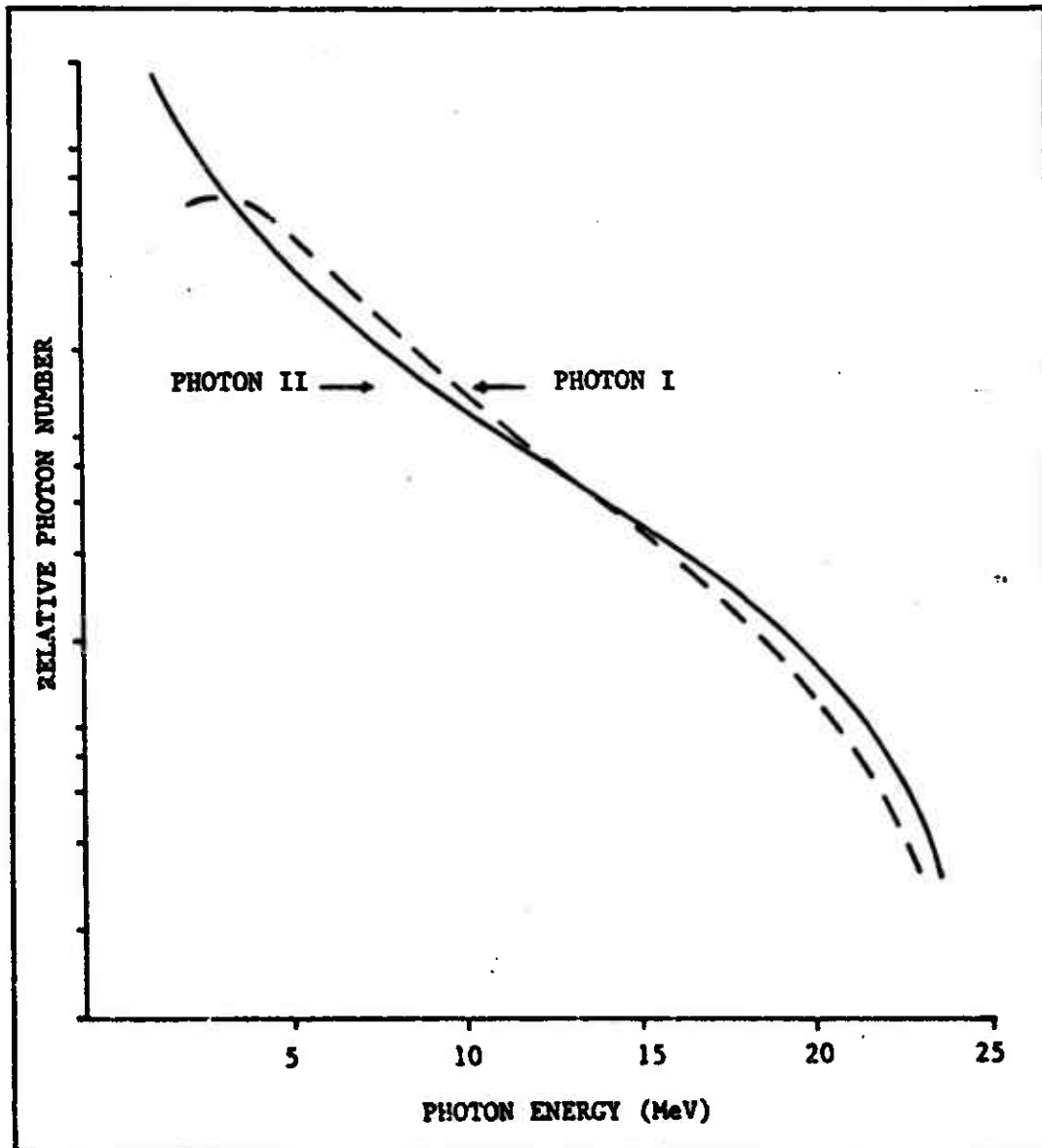


Figure 26. Sagittaire - photon I (flattened) and photon II - 25 MeV spectra (normalized at mid-spectrum).

clearly shown. The flattened beam has a lower relative number of high-energy photons and a higher relative number of lower-energy photons than does the unflattened beam. It is this "beam softening" effect that is the suggested cause of the reduction of photonuclear ratios discussed in the previous section.

Appendix F contains selected calculations of thick-target bremsstrahlung spectra. The endpoint energies for which the calculated photon and energy fluences are shown correspond to the nominal energies of commercially available high-energy accelerators. These energies are 25, 24, 22, 20, 18, and 15 MeV. For each energy, both a "monoenergetic endpoint spectrum" and a spectrum produced by electrons having a $\pm 2\%$ energy spread are shown.

Electron Multiple-Scattering

The calculation of thick-target bremsstrahlung spectra required prior knowledge of the angular distribution of electrons scattered by multiple collisions in the slabs of the target. A frequently used approximation to the electron multiple-scattering distribution is obtained from the theory of Molière (55). The first term of Molière's formulation is a Gaussian function for which the RMS angle of multiple-scattering is given by Eq. (81a). Hanson (72) measured the angular distribution of electrons scattered in thin foils and found that a renormalization of Molière's first term resulting in a Gaussian with reduced width represented a better approximation to his experimental data. Hanson's renormalization consisted of subtracting the number 1.2 from the Molière parameter "B" [see Eq. (81a)]. Similar renormalizations have been performed (82). The results of the measurement of the angular distribution of electron multiple scat-

tering in the target of the Sagittaire accelerator demonstrated that renormalization of Molière's first term into a Gaussian with reduced width also was required in this experiment.

The results of the investigation into the multiple-scattering distribution of electrons in the Sagittaire target are shown in Figure 27. The open triangles represent relative number of ^{11}C counts as a function of angle from the bremsstrahlung beam central axis. The smooth curve is the Gaussian fit to the experimental points. The standard deviation of the Gaussian curve [θ_{meas} of Eq. (85)] was 4.27 degrees. The effective angle of multiple-scattering obtained from the bremsstrahlung computer program [θ_{eff} of Eq. (85)] was 7.57 degrees resulting in a normalization factor F_n of 1.773.

The Molière B is a function of slab thickness. For a slab thickness of $.0386 \text{ g/cm}^2$ (slab thickness used in the computer program), $B = 7.35$ (67). The RMS angle of multiple-scattering is a function of the square root of E. Because the normalization factor was obtained from a measurement of angle, it was squared first and then divided into $B = 7.35$ to yield a corrected (renormalized) B of 2.34. Thus B was decreased by subtracting 5.01 from the tabulated value (67). It should be pointed out that, although this renormalization amounts to a substantial correction to the Molière B factor, the renormalization procedure was found to have a practically negligible effect on the shape of the bremsstrahlung spectra produced in the computer program. The correction was still incorporated, however, for the sake of simulating actual experimental conditions as closely as possible.

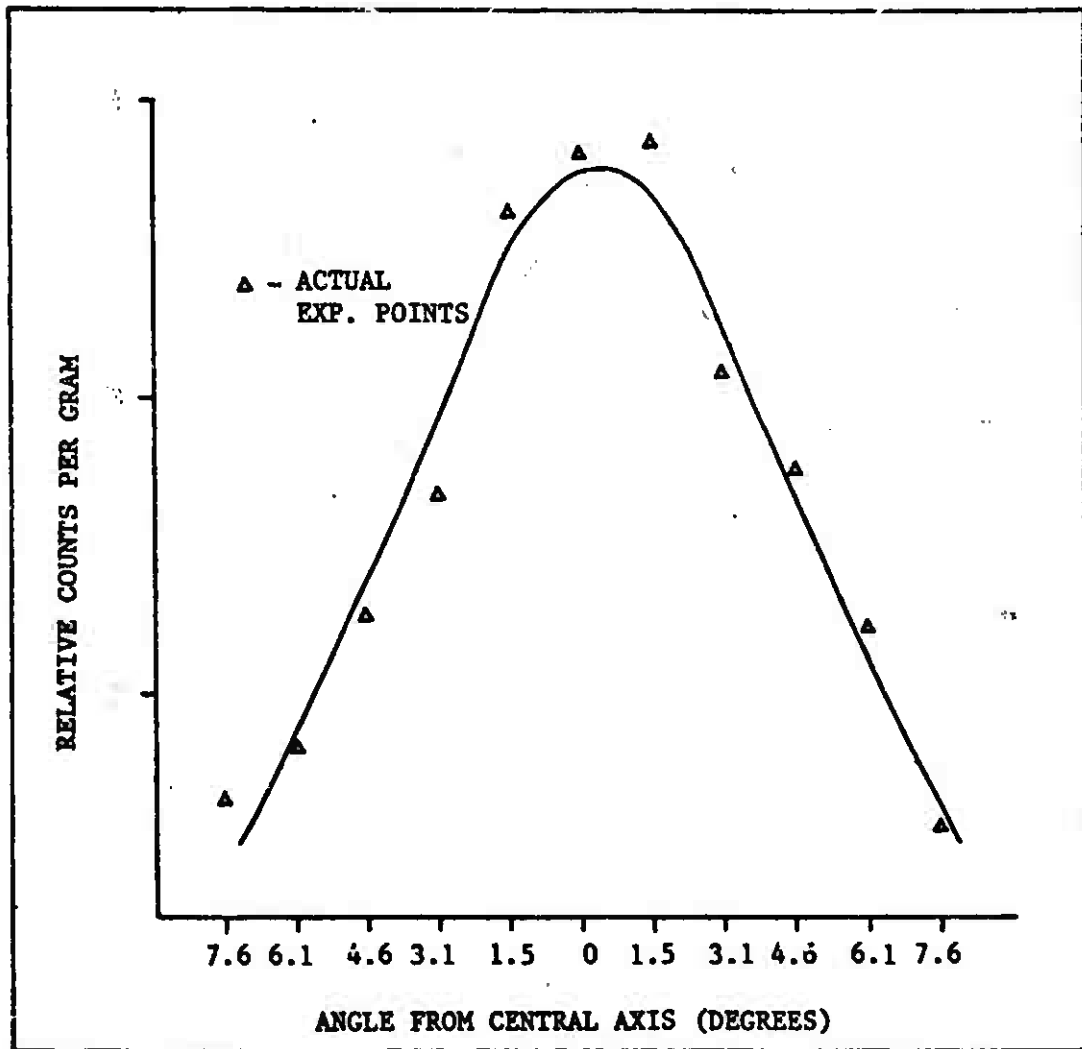


Figure 27. Gaussian fit to the experimental points of the measurement of electron multiple scattering angle.

The $^{27}\text{Al}(\gamma, 2p)^{25}\text{Na}$ Cross Section

The measured normalized yield of $^{27}\text{Al}(\gamma, 2p)^{25}\text{Na}$ reactions as a function of bremsstrahlung endpoint energy from 25 to 33 MeV is shown in Figure 28. The units on the ordinate are number of reactions per unit response of the radiation monitor system in volts. The standard errors of the data points are less than the size of the points. The data below 27 MeV show significant scatter because of the absence of ^{25}Na counts in that region resulting in poor counting statistics. Above 27 MeV the yield increases continuously. Several "breaks," changes in the rate of climb of yield as a function of increasing endpoint energy, are apparent in the yield curve between 27 and about 31 MeV. These breaks occur at approximately 27.3 and 30.3 MeV. Some of these breaks have been observed previously (7,57), but a determination of cross section has never been made to verify if in fact the breaks corresponded to resonances in the cross section.

In order to determine the cross section of the $^{27}\text{Al}(\gamma, 2p)^{25}\text{Na}$ reaction, the normalized yield data of Figure 28 were converted to reduced yield (number of reactions per target nucleus per cm^2 of sample). This was accomplished using Eq. (15). The factor $E(T)$ of Eq. (13) is the total energy in the bremsstrahlung spectrum as a function of endpoint energy. Because, for comparison purposes, the reaction cross section was obtained using both Schiff integrated-over-angle and thick-target bremsstrahlung spectra, both spectra were integrated as a function of endpoint energy and simple analytical expressions were fit to the integration results. The total energy curves for Schiff and thick-target spectra as a function of endpoint energy between 15 and 35 MeV are shown in Figure 29. The

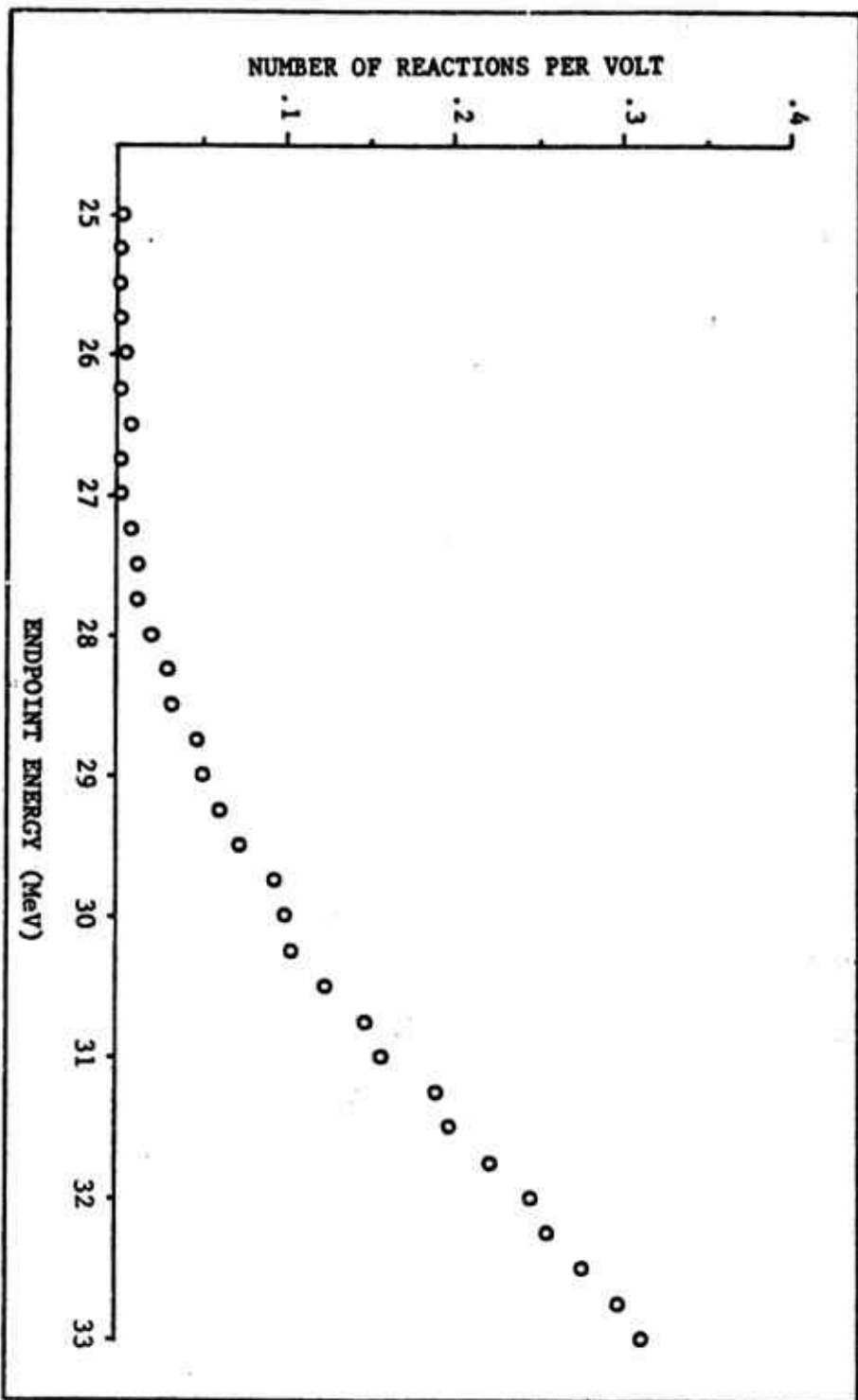


Figure 28. Normalized yield of $^{27}\text{Al}(r,2p)^{25}\text{Na}$ reactions.

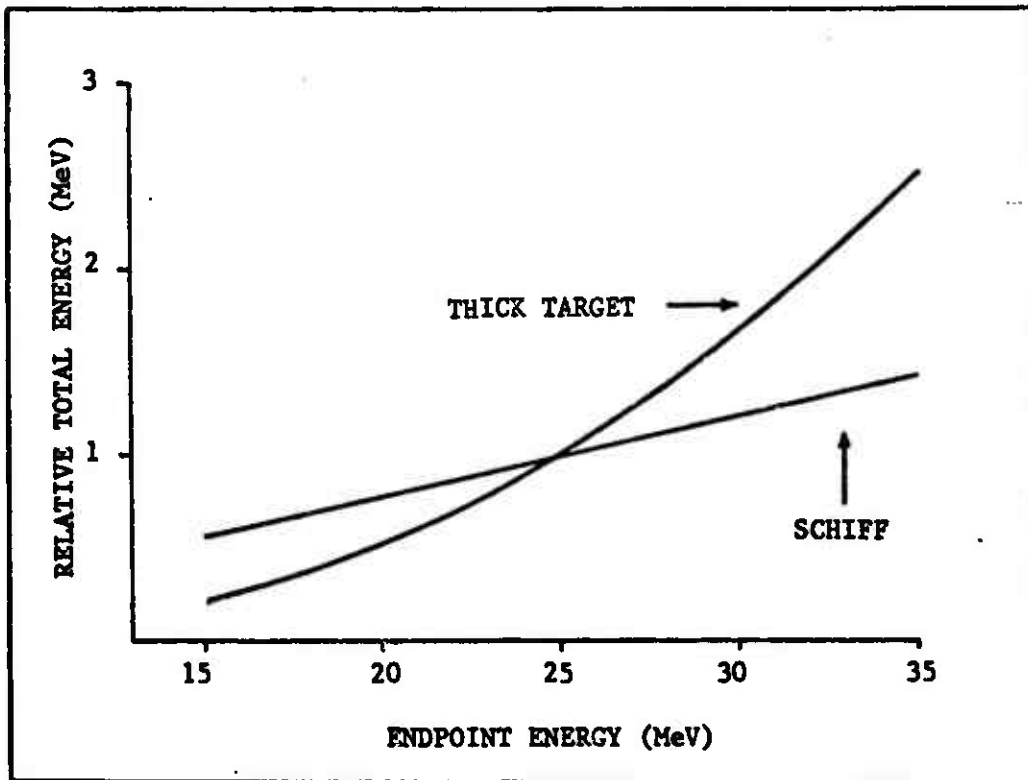


Figure 29. Comparison of the total energy in Schiff and thick-target spectra.

curves were normalized at 25 MeV. As expected, because of the greater number of lower-energy photons in the thick-target spectra and their relatively large contribution to the total spectral energy, the thick-target total energy curve increases more rapidly with increasing endpoint energy than does the Schiff total energy curve. The reduced yield curve obtained using thick-target total energy thus increased more rapidly with increasing endpoint energy than did the reduced yield curve obtained with Schiff spectral total energy. This is shown in Figure 30 where the Schiff reduced yield is represented by circles and the thick-target reduced yield is represented by triangles. The reduced yields of Figure 30 were normalized at 29 MeV. Only data points at half-MeV intervals are shown.

The $^{27}\text{Al}(\gamma,2p)^{25}\text{Na}$ cross section as a function of endpoint energy obtained with the Lesst Structure computer program (36) using thick-target bremsstrahlung spectra corrected for the $\pm 2\%$ endpoint energy spread is shown in Figure 31. The χ^2 (amount of smoothing) applied to the cross section from 27 to 33 MeV was 99 when the Lagrangian multiplier (λ) was $(1.0)10^{-8}$ (see the Analysis and Solution of Photonuclear Yields section of Chapter II). Evident from Figure 31 is the structure in the cross section expected from the breaks seen in the normalized yield curve (Fig. 28). Figure 31 shows cross section resonances at about 27.3 and 30.3 MeV. Relative resonance magnitudes are directly related to relative changes in slope of the yield curve. The undershoot below 27.0 MeV is due most probably to statistical fluctuations produced by the scatter of measured yields in that energy range.

The absolute magnitude of the cross section was obtained by normalizing the integrated cross section to that of Aull and Whitehead (21).

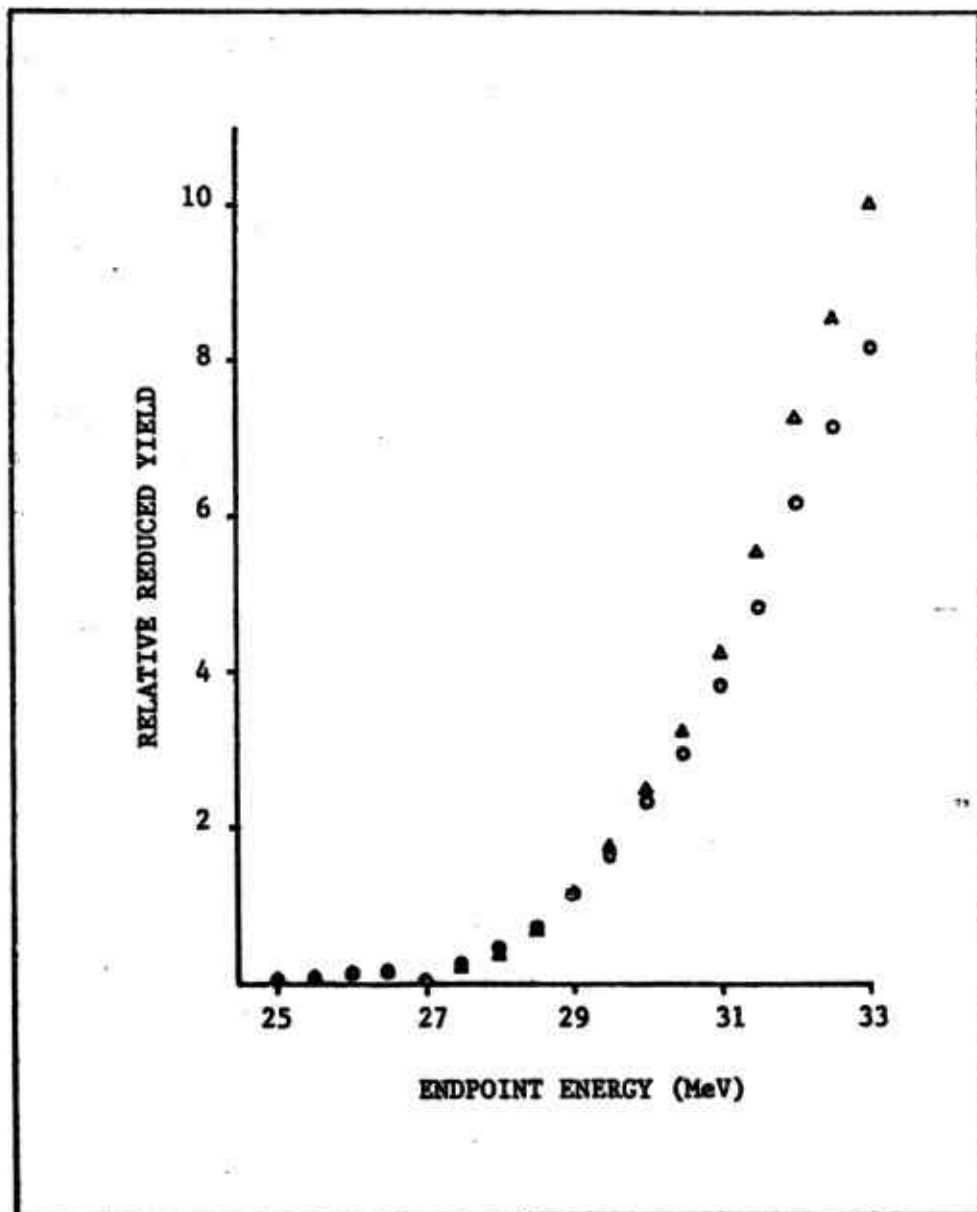


Figure 30. Schiff (\circ) and thick target (\blacktriangle) reduced yields (normalized at 29 MeV).

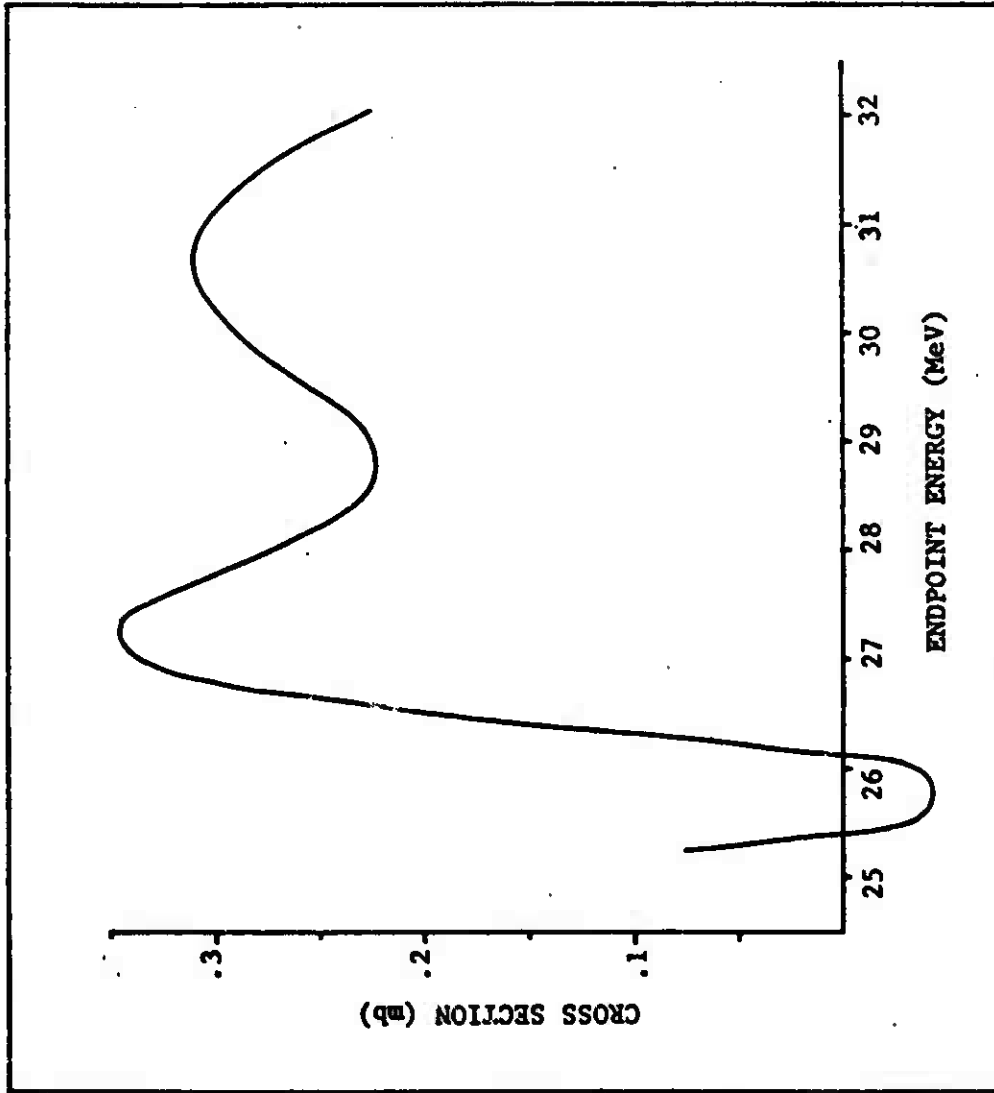


Figure 31. The $^{27}\text{Al}(r,2p)^{25}\text{Na}$ cross section obtained with thick-target bremsstrahlung spectra.

The integrated cross section reported by the above authors agreed with previous measurements (83). After normalization, the integrated cross section from 25 to 32 MeV was 1.6 MeV-mb, and the peak cross section was .35 mb at 27.3 MeV. The magnitude of the cross section resonance at 30.3 MeV was .31 mb.

There are differences between the $^{27}\text{Al}(\gamma,2p)^{25}\text{Na}$ cross section obtained here using thick-target bremsstrahlung spectra and the published $^{27}\text{Al}(\gamma,2p)^{25}\text{Na}$ cross section of Aull and Whitehead (21), which is shown in Figure 32. One difference is the lack of structure in the Aull and Whitehead cross section. The above authors made measurements of yield in 1.0 MeV intervals from 25 to 36 MeV and in 2.0 MeV intervals from 36 to 65 MeV. In addition, they smoothed the yield curve before analyzing it for cross section determination. Finally, the cross section itself was smoothed, as illustrated in Figure 32 by the difference between the smooth curve and the points. The smoothing procedures, in combination with the lack of resolution resulting from yield measurements at only integral MeV values from 25 to 36 MeV, may account for the lack of structure in that energy range. In the present work, yield measurements were made in 0.25 MeV increments and no smoothing was applied to the yield curve. The increased resolution of the present measurements and the use of Least Structure to analyze the data (requiring no yield smoothing) permitted a more detailed examination of possible structure in the cross section.

Other differences between the cross section reported here and that of Aull and Whitehead are the location of the peak cross section and the cross section trend with increasing endpoint energy. The above authors' cross section increased constantly with increasing endpoint

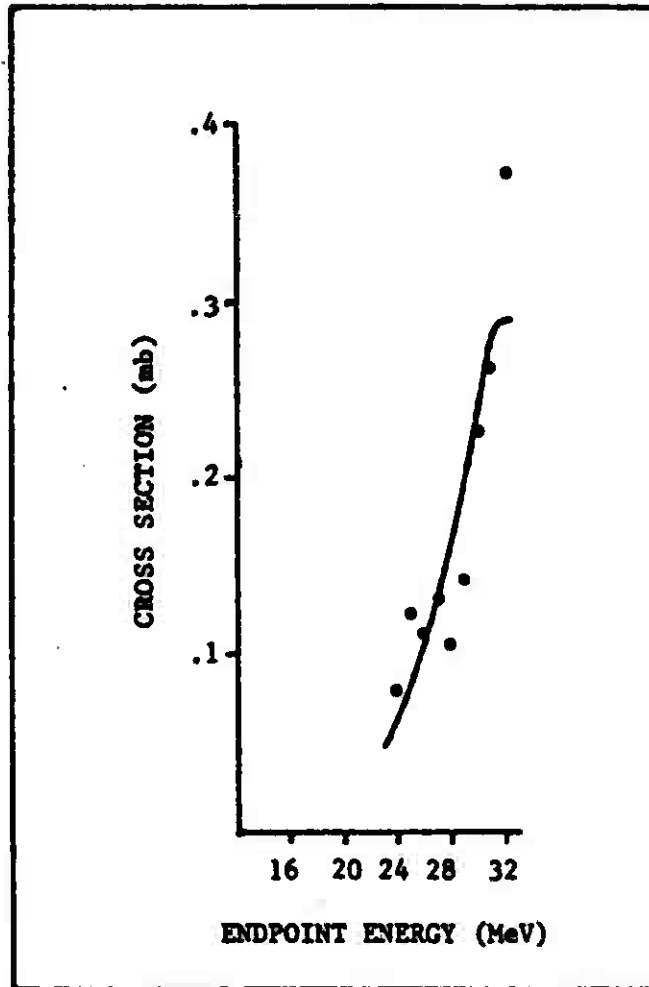


Figure 32. The $^{27}\text{Al}(\gamma, 2p)^{25}\text{Na}$ cross section reported by Aull and Whitehead.

energy and peaked at 32.0 MeV (21). The cross section reported here peaked at about 27.3 MeV, contained a resonance at 30.3 MeV, and thereon had an essentially downward trend with increasing endpoint energy. It is suspected that the difference in peak cross section location is due to the different bremsstrahlung spectra used for cross section determination. Aull and Whitehead analyzed their data using Penfold and Leiss matrices (34) which were obtained from thin-target (Schiff) bremsstrahlung spectra even though they report a target thickness of $.98 \text{ g/cm}^2$ tungsten. The cross section reported here was obtained using thick-target bremsstrahlung spectra. The $^{27}\text{Al}(\gamma, 2p)^{25}\text{Na}$ yield curve measured in this work was also analyzed using Schiff spectra to demonstrate the dramatic effect of bremsstrahlung spectral shape on the resultant cross section.

The cross section as a function of endpoint energy obtained by analyzing the $^{27}\text{Al}(\gamma, 2p)^{25}\text{Na}$ yield curve measured in this study utilizing Schiff spectra is shown in Figure 33. The χ^2 applied to the cross section from 27 to 33 MeV was 58 when $\lambda = (1.0)10^{-12}$. The cross section now peaked around 32.5 MeV. This result is in agreement with that of Aull and Whitehead (21), who obtained a peak cross section at 32.0 MeV. The differences in the two cross sections obtained from the same yield data using both thin- and thick-target bremsstrahlung spectra can be due only to differences in thin- and thick-target spectral shapes.

Figure 34 shows the Schiff and thick-target 30 MeV spectra used in the Least Structure program to produce the $^{27}\text{Al}(\gamma, 2p)^{25}\text{Na}$ thin- (Schiff) and thick-target cross sections. The curves have been normalized at 27.375 MeV. Note the much larger proportion of lower-energy photons in the thick-target spectrum as compared to the relatively constant number of low-energy

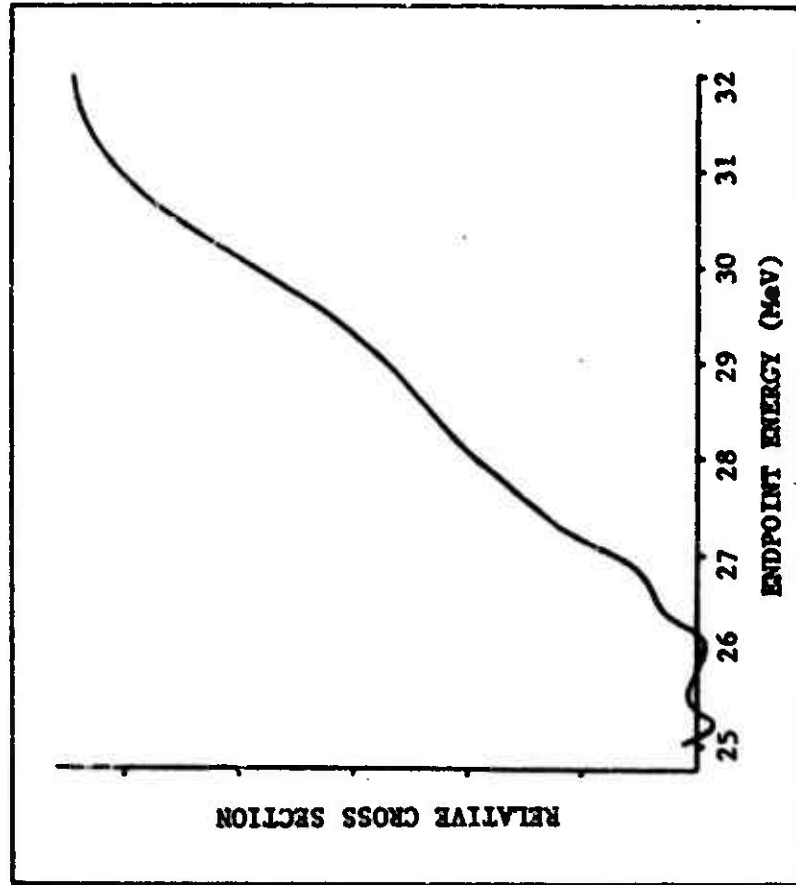


Figure 33. The $^{27}\text{Al}(j,2p)^{25}\text{Na}$ cross section obtained with Schiff bremsstrahlung spectra.

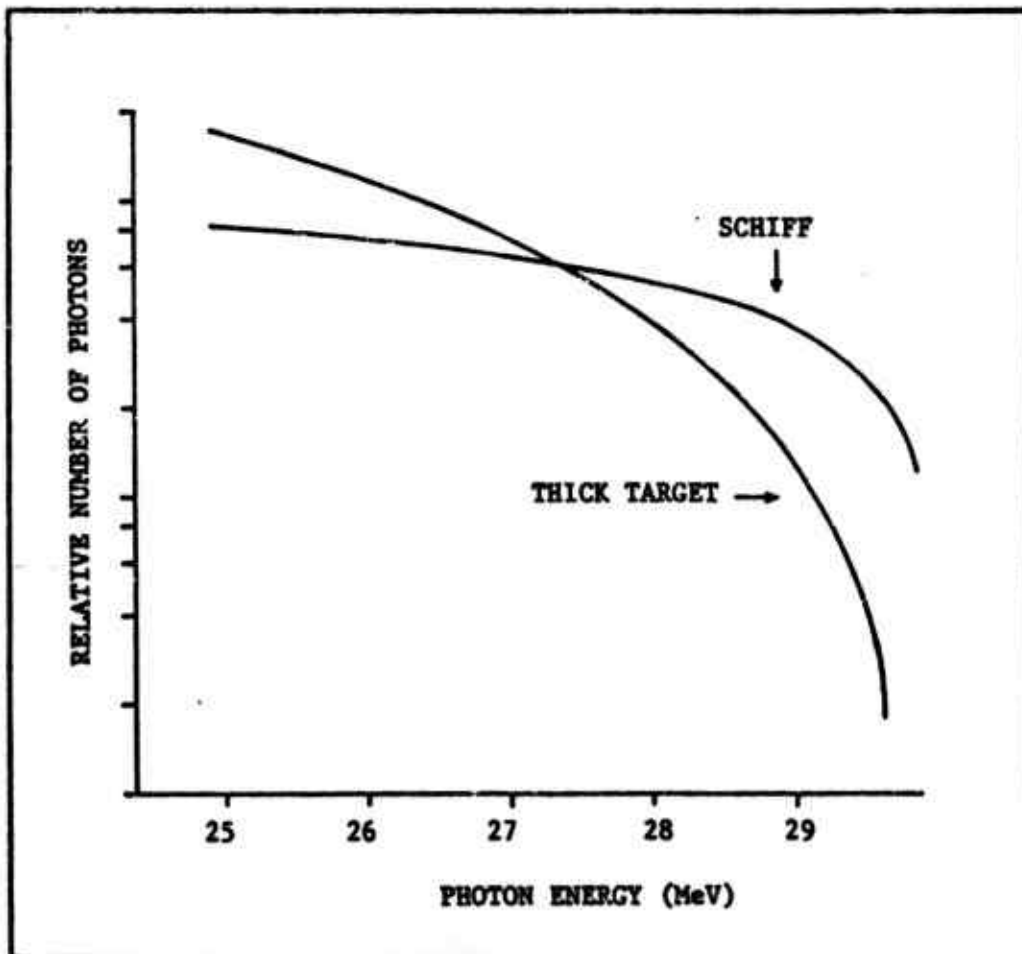


Figure 34. 30 MeV Schiff and thick-target spectra used in the cross section analyses.

photons in the Schiff spectrum. In an analysis of photonuclear yield to produce a cross section, this characteristic shape of the thick-target spectrum will have a profound effect on the resultant cross section. At a given endpoint energy, the number of photonuclear reactions induced in a sample are produced by all photons in the spectrum of energy exceeding the threshold energy of the reaction. In the case of thick-target bremsstrahlung, because of the large proportion of lower-energy photons, more reactions are produced by photons in the lower energy range than are produced by photons near the tip of the spectrum (assuming the cross section does not change appreciably over the same energy range). This fact was verified by examining the resolution function of the thick-target $^{27}\text{Al}(\gamma, 2p)^{25}\text{Na}$ cross section and noting the influence of lower energies on cross sections at higher energies. Thus, for a given photonuclear reaction, yields produced by thick-target bremsstrahlung increase more rapidly with increasing endpoint energy than will yields produced by thin-target (Schiff) bremsstrahlung. If a yield curve produced with thick-target bremsstrahlung is analyzed for cross section using Schiff spectra, the resultant cross section will show a continuous increase with increasing endpoint energy. This is due to the combined effect of: 1) an increased availability of photons possessing energies that exceed the threshold energy of the reaction thus resulting in a more rapidly increasing yield, and 2) the lack of a proportionately larger number of low-energy photons in the bremsstrahlung spectrum used to analyze the yield.

The aforementioned effect is responsible for the cross section shown in Figure 33. The cross section continuously increases because of the increased yields produced by lower-energy photons in the thick-target

bremstrahlung used to produce the yields. The good agreement between the thin-target cross section obtained here and the Aull and Whitehead cross section seems to suggest that the above authors may have made an unfortunate choice of bremstrahlung spectrum in their analysis. Aull and Whitehead irradiated their aluminum samples with bremstrahlung produced in a 0.98 g/cm^2 tungsten target (21) and analyzed their yield curve using Schiff spectra. The choice seems inappropriate, particularly in view of the relatively good agreement of the thick-target calculations performed in this work with the data of O'Dell (79) which was obtained with a target of less thickness (0.735 g/cm^2).

CHAPTER V

CONCLUSIONS

Photonuclear Ratios

Photonuclear reactions are particularly well-suited for the study of high-energy bremsstrahlung spectra. Their aptness as a research tool for this type investigation is afforded by virtue of the dependence of photonuclear-reaction cross sections on photon energy. Photonuclear-reaction thresholds and cross-section resonances have been used in the energy calibration of linear accelerators (6-8) and in the determination of thin-target x-ray spectra (5). Ratios of photonuclear yields in select materials have been used as indices of thin-target x-ray quality (9,10). The research reported here utilized photonuclear reactions to study the distribution in energy of photons in thick-target x-ray spectra and the effect of spectral shape on photonuclear yield measurements and cross section determinations.

Photonuclear yield ratios in K_2SiF_6 and in teflon have been obtained which serve as indices of thick-target bremsstrahlung quality in the energy range from about 14 to 30 MeV. Many commercially available linear accelerators possess nominal energies in this range, with endpoint energies of 15, 18, 20, 22, 24, and 25 MeV being most common. Photonuclear

ratios published previously (9,10) were obtained from essentially thin-target x rays and failed to provide unique indices from 15 to 25 MeV. Ratios in K_2SiF_6 demonstrated a sensitivity (percent change of ratio per MeV) of about 26% at 15, 31% at 18, and 17% at 20 MeV. Ratios in teflon had sensitivities of about 75% at 22, 41% at 24, and 27% at 25 MeV.

The ratios obtained here, and hence the reported sensitivities as a function of endpoint energy changes, apply in a strict sense only to lightly-filtered (2.7 mm Pb) thick-target (4 mm W) bremsstrahlung produced by electrons possessing an energy spread of $\pm 2\%$ of the mean kinetic energy. The insertion of a thicker flattening filter (2.8 cm Pb), on the other hand, reduced the ratios by only approximately 15% in the worst case (29 MeV teflon ratio). The effect of different target thicknesses on ratio sensitivity could not be investigated. Nath and Schulz (9), however, report only a 10% decrease of their $^{65}Cu/^{89}Y$ ratio at 30 MeV when the target thickness was increased from about .35 to 2.2 radiation lengths. Different initial electron energy distributions also could affect the reported magnitudes and sensitivities of the ratios. The result of electron-energy spread on the bremsstrahlung spectrum seems to be a net increase in the number of photons comprising the spectrum tip. Thus, it is suspected that an increased electron-energy spread may increase the magnitude of the ratio at the mean endpoint energy. On the other hand, ratio sensitivity should not be appreciably affected.

Because ratios in K_2SiF_6 and teflon are independent of the mass of the sample, the flux of photons and the efficiency of the counting system, they should be extremely useful to medical physicists seeking to augment their accelerator quality control program with a simple yet sen-

sitive index of x-ray quality. The absence of strong lines in the vicinity of the .511 MeV photopeak suggests that a NaI(Tl) counting system could be used in lieu of a semiconductor system, provided that background corrections are made in a careful and reproducible manner.

The Bremsstrahlung Spectrum

The review of the photonuclear literature which was conducted in preparation for this work conveyed the fact that thick-target bremsstrahlung spectra had never before been utilized in the analysis of photonuclear yields for cross-section determination. To this purpose a computer program was developed which consisted of a numerical-analysis calculation of thick-target bremsstrahlung spectra. The computer program was capable of calculating spectra at any endpoint energy from 10 to 35 MeV from targets of essentially any thickness and atomic number. Provisions were made to include the effects of endpoint-energy spread. Electron-energy spread has never been incorporated before into calculations of this type. The program was checked by comparing the results of a simulation made of the 21 MeV thick-target spectrum of O'Dell (79) with his experimental measurements and with the results of other calculations (51,53). In general, the results of the simulation compared quite favorably with the published measurements and calculations, particularly when electron-energy spread was considered. The largest discrepancies occurred at the high-energy end (tip) of the spectrum. The reasons for the discrepancies are: the inability of Born approximation calculations to characterize the spectrum tip, the unavailability of calculations appropriate for spectra of energies less than about 30-50 MeV that do not incorporate the Born approximation, and the extreme experimental difficulties of measuring precisely the tip

of bremsstrahlung spectra. Even to this day, further theoretical and experimental research is needed badly in this area.

The $^{27}\text{Al}(\gamma, 2p)^{25}\text{Na}$ Cross Section

The $^{27}\text{Al}(\gamma, 2p)^{25}\text{Na}$ cross section reported here was obtained from measurements of yield made at 0.25 MeV increments from 25 to 33 MeV. This cross section had never been calculated with such energy resolution. The increased resolution of this experiment allowed inspection of possible structure in the cross section. The cross section of Figure 31 shows two resonances, one at 27.3 MeV and one at 30.3 MeV. This structure is unique, possibly indicating the existence of states at these high energies. Absorption by two single-particle-like transitions from deep-lying shells may be responsible for the cross section at these energies (43). Transitions from 1p and 1s shell states may be important in the absorption of photons above 20 MeV in nuclei such as ^{27}Al .

LIST OF REFERENCES

1. Bennet G.W., Dobert R., Meltzer J., Archambeau B.E., and Archambeau J.O.: *Brit. J. Radiol.* 54, 53-56 (1981).
2. Mayneord W.V., Martin J.H., and Layne D.A.: *Nature* 164, 728-730 (1949).
3. McNeil K.G.: *Phys. Today* 27, No. 4, 75-83 (1974).
4. Engelman C.: *Proc. Int. Conf. on Photonuclear Reactions and Applications*, CONF-730301, 1137-1153 (1973).
5. Nath R. and Schulz R.J.: *Med. Phys.* 3, 133-141 (1976).
6. St. George F. and Anderson D.W.: *Med. Phys.* 9, 414-418 (1982).
7. St. George F. and Anderson D.W.: *Phys. Med. Biol.* 27, 1475-1482 (1982).
8. Anderson D.W. and Swift S.C.: *Phys. Med. Biol.* 15, 349-354 (1970).
9. Nath R. and Schulz R.J.: *Med. Phys.* 4, 36-41 (1977).
10. Schulz R.J. and Nath R.: *Med. Phys.* 4, 42-45 (1977).
11. Piltingsrud H.V.: *Med. Phys.* 10, 147-154 (1983).
12. Piltingsrud H.V.: *Med. Phys.* 9, 514-520 (1982).
13. International Commission of Radiological Units and Measurements (ICRU): Physical Aspects of Irradiation, NBS Handbook 85, 69-86 (1964).
14. Nath R. and Schulz R.J.: *Med. Phys.* 4, 132-133 (1977).
15. Johns H.E. and Cunningham J.R.: The Physics of Radiology. Charles C. Thomas, 766-767 (1974).
16. Hospital Physicists Association: *Brit. J. Radiol. Suppl.* 11, 77-82 (1972).

17. Nordic Association of Clinical Physics: *Acta Radiol. Ther. Phys. Biol.* 11, 603-623 (1972).
18. Strauch K.: *Ann. Rev. Nucl. Sci.* 2, 105-128 (1953).
19. Bogdankevich O.V. and Nikolaev F.A.: *Methods in Bremsstrahlung Research*. Academic Press, 1-25, 107-161 (1966).
20. Schiff L.I.: *Phys. Rev.* 83, 252-253 (1951).
21. Aull L.B. and Whitehead W.D.: *Phys. Rev.* 110, 1113-1115 (1958).
22. Levinger J.S. and Bethe H.A.: *Phys. Rev.* 78, 115-129 (1950).
23. Levinger J.S.: *Ann. Rev. Nucl. Sci.* 4, 13-32 (1954).
24. Wilkinson D.H.: *Physica* 22, 1039-1061 (1956).
25. Wilkinson D.H.: *Ann. Rev. Nucl. Sci.* 9, 1-28 (1959).
26. Hayward E.: *Rev. Mod. Phys.* 35, 324-331 (1963).
27. Enge H.A.: *Introduction to Nuclear Physics*. Addison-Wesley, 431-436 (1966).
28. Levinger J.S.: *Nuclear Photodisintegration*. Oxford University Press, 1-36 (1960).
29. Griffin J.E. and Hammer C.L.: USAEC Report IS-676, 5-21 (1963).
30. Elliott J.P. and Flowers B.H.: *Proc. Roy. Soc.* A242, 57-80 (1957).
31. Brown G.E. and Bolsterli M.: *Phys. Rev. Letters* 3, 472-476 (1959).
32. Brown G.E., Castillejo L. and Evans J.A.: *Nucl. Phys.* 22, 1-13 (1961).
33. Brink D.: *Nucl. Phys.* 4, 215-220 (1957).
34. Penfold A.S. and Leiss J.E.: *Phys. Rev.* 114, 1332-1337 (1959).
35. Katz L. and Cameron A.G.W.: *Canad. J. Phys.* 29, 518-545 (1951).
36. Cook B.C.: *Nucl. Inst. Meth.* 24, 256-268 (1963).
37. Cook B.C., Baglin J.E., Bradford J.N. and Griffin J.E.: *Phys. Rev.* 143, 712-723 (1966).
38. Sokolnikoff I.S. and Redheffer R.M.: *Mathematics of Physics and Modern Engineering*. McGraw-Hill, 249-257 (1958).

39. Anderson D.W., Bureau A.J., Cook B.G., Griffin J.E., McConnell J.R. and Nybo K.H.: *Phys. Rev. Letters* 10, 250-253 (1963).
40. Cook B.G., Baglin J.E., Bradford J.N. and Griffin J.E.: *Phys. Rev.* 143, 724-729 (1966).
41. Anderson D.W. and Swift S.G.: *Nucl. Phys.* A150, 625-630 (1970).
42. Anderson D.W., Petry R.F. and Fischbeck H.J.: *Phys. Rev.* G9, 1919-1923 (1974).
43. Anderson D.W., Petry R.F. and Fischbeck H.J.: *Nucl. Phys.* A262, 91-95 (1976).
44. Matthews J.L. and Owens R.D.: *Nucl. Inst. Meth.* 111, 157-168 (1973).
45. Bethe H.A. and Maximon L.C.: *Phys. Rev.* 93, 768-784 (1954).
46. Koch H.W. and Motz J.W.: *Rev. Mod. Phys.* 31, 920-955 (1959).
47. Bethe H.A. and Heitler W.: *Proc. Roy. Soc.* A146, 83-112 (1934).
48. Heitler W.: The Quantum Theory of Radiation. Oxford University Press, 161-177 (1936).
49. Olsen H. and Maximon L.C.: *Phys. Rev.* 114, 887-904 (1959).
50. Starfelt N. and Koch H.W.: *Phys. Rev.* 102, 1598-1612 (1956).
51. Berger M.J. and Seltzer S.M.: *Phys. Rev.* C2, 621-631 (1970).
52. Lent E.M. and Dickinson W.C.: UCRL Report 50442 (1968).
53. Ferdinande H., Knuyt G., Van de Vijver R. and Jacobs R.: *Nucl. Inst. Meth.* 91, 135-140 (1971).
54. Hisdal E.: *Phys. Rev.* 105, 1821-1826 (1957).
55. Molière G.: *Z. Naturforsch.* 3a, 78-97 (1948).
56. Pruitt J.S. and Domen S.R.: NBS Monograph 48 (1962).
57. St. George F.J.: Ph.D. Dissertation. University of Oklahoma (1980).
58. McCormick W.W.: Fundamentals of University Physics. Macmillan, 507-508 (1970).
59. Siegbahn K.: Beta and Gamma Ray Spectroscopy. North-Holland, 52-58 (1955).
60. Evans R.D.: The Atomic Nucleus. McGraw-Hill, 692 (1955).

61. Princeton Gamma-Tech, Inc.: Intrinsic Germanium Detector SN 297 Specifications (1976).
62. Gehrke R.J., Helmer R.G. and Greenwood R.C.: Nucl. Inst. Meth. 147, 405-423 (1977).
63. Knoll G.F.: Radiation Detection and Measurement. John Wiley & Sons, 359-413, 492-502, 711-732 (1979).
64. Sagane R.: Phys. Rev. 85, 1065 (1952).
65. Motz J.W., Miller M. and Wycoff H.O.: Phys. Rev. 89, 968-971 (1953).
66. Storm E. and Israel H.I.: Nucl. Dat. Tables A-7, 565-681 (1970).
67. Berger M.J. and Seltzer S.M.: NASA SP-3012 (1964).
68. Bichsel H.: American Institute of Physics Handbook, 2nd Ed. (D.E. Gray, Ed.), 20-47 (1963).
69. Frank H.: Z. Naturforsch. 14a, 247-261 (1959).
70. Ebert P.J., Lauzon A.F. and Lent E.M.: Phys. Rev. 183, 422-430 (1969).
71. Statistical Analysis System Institute: SAS User's Guide, 317-329 (1979).
72. Hanson A.O., Lanzl L.H., Lyman E.M. and Scott M.B.: Phys. Rev. 84, 634-637 (1951).
73. King J.D., Haslam R.N.H. and McDonald W.J.: Canad. J. Phys. 38, 1069-1076 (1960).
74. Kayser K., Collin W., Filss P., Guldbakke S., Nolte G., Reich H., Trier J.O. and Witschel W.: Z. Physik 239, 447-460 (1970).
75. Goldman D., Piza A.F.T. and Silva E.: Il Nuovo Cimento 25, 41-47 (1962).
76. Costa S., Ferrero F., Ferroni S. and Pasqualini L.: Nucl. Phys. 72, 158-166 (1965).
77. Miller J., Schuhl G., Tamas G. and Tzara C.: J. de Physique 27, 8-12 (1966).
78. Fuller E.G., Gerstenberg H.M., Van der Mollen H. and Dunn T.C.: Photonuclear Reaction Data, 1973; NBS Special Publication 380 (1973).
79. O'Dell A.A., Sandifer C.W., Knowlen R.B. and George W.D.: Nucl. Inst. Meth. 61, 340-346 (1968).

80. Stearns M.: Phys. Rev. 76, 836-838 (1949).
81. Matthews J.L. and Owens R.O.: Nucl. Inst. Meth. 111, 157-168 (1973).
82. Scott W.T.: Rev. Mod. Phys. 35, 231-313 (1963).
83. Edwards L.S. and MacMillan F.A.: Phys. Rev. 87, 377 (1952).
84. Arya A.P.: Fundamentals of Nuclear Physics. Allyn & Bacon, 354-368, 613-622 (1966).
85. Meyerhoff W.E.: Elements of Nuclear Physics. McGraw-Hill, 12-32, 46-64 (1967).
86. Evans R.D.: The Atomic Nucleus. McGraw-Hill, 358-365, 860-866 (1955).
87. Beiser A.: Perspectives of Modern Physics. McGraw-Hill, 195-219 (1969).
88. Mayer M.G. and Jensen J.H.D.: Elementary Theory of Nuclear Shell Structure. John Wiley & Sons, 50-60 (1955).
89. Saxon D.S.: Elementary Quantum Mechanics. Holden Day, 189-201, 208-219, 279-286 (1968).
90. Schiff L.I.: Quantum Mechanics. McGraw-Hill, 76-78 (1955).
91. Stehle P.: Quantum Mechanics. Holden Day, 82-84 (1966).
92. Kaplan I.: Nuclear Physics. Addison-Wesley, 428-433 (1962).
93. Blatt J.M. and Weisskopf V.F.: Theoretical Nuclear Physics. John Wiley & Sons, 623-629 (1952).
94. Atomic Energy of Canada, Limited: Specifications THERAC 40/Sagittaire Medical Linear Accelerator, No. GS 3100 (1975).
95. Karzmark C.J. and Pering N.C.: Phys. Med. Biol. 18, 321-354 (1973).
96. Livingston M.S. and Blewett J.P.: Particle Accelerators. McGraw-Hill, 310-328 (1962).
97. Smith L.: Linear Accelerators. In Encyclopedia of Physics, Vol. 44, 341-388 (1959).
98. Hoffer P.B., Beck R.N. and Gottschalk A.: The Role of Semiconductor Detectors in the Future of Nuclear Medicine. Society of Nuclear Medicine, 1-36 (1971).
99. Hine G.J.: Instrumentation in Nuclear Medicine, Volume I. Academic Press, 119-142 (1967).

100. National Council on Radiation Protection and Measurements (NCRP): A Handbook of Radioactivity Measurements Procedures, NCRP Report No. 58, 131-141 (1978).
101. Chase R.L.: Nuclear Pulse Spectrometry. McGraw-Hill, 75-98 (1961).
102. Ouseph P.J.: Introduction to Nuclear Radiation Detectors. Plenum Press, 129-167 (1975).
103. Price W.J.: Nuclear Radiation Detection. McGraw-Hill, 212-266 (1964).

APPENDIX A

The Shell Model of Nuclear Structure

The starting point in the understanding of nuclear structure is the Schrodinger equation which is (84,85)

$$\frac{-\hbar^2}{2m} \nabla^2 \Psi + V\Psi = i\hbar \frac{\partial \Psi}{\partial t} \quad (A1)$$

where

$\hbar = h/2\pi$; $h = \text{Planck's constant}$

$m = \text{rest mass of particle}$

$$\nabla^2 = \frac{\partial^2}{\partial x^2} + \frac{\partial^2}{\partial y^2} + \frac{\partial^2}{\partial z^2}$$

$\Psi = \text{wave function of particle}$

$V = \text{potential energy of particle}$

$$i = (-1)^{1/2} .$$

If the potential energy is independent of time, we can separate space and time variables. (a technique for solving certain differential equations which is used frequently) by setting

$$\Psi = \psi(x,y,z)\zeta(t) \quad (A2)$$

where $\psi(x,y,z)$ and $\zeta(t)$ are functions exclusively of space and of time variables, respectively. Substituting Eq. (A2) into Eq. (A1) and dividing by $\psi\zeta$ yields

$$\frac{-\hbar^2}{2m} \frac{\nabla^2 \psi}{\psi} + V = \frac{i\hbar}{\zeta} \frac{d\zeta}{dt} . \quad (A3)$$

Since the left-hand side of this equation depends only on space variables and the right-hand side only on time, the equation cannot be satisfied for all points in space at all times unless each side is equal to the same constant. Call this "separation constant" the total energy of the

system, E . The right-hand side of Eq. (A3) is readily solvable yielding solutions

$$\zeta = \exp[-i(E/\hbar)\tau] \quad (\text{A4})$$

where, for convenience, the constant of integration has been set equal to unity. The left-hand side of Eq. (A3) can be written (after rearranging) as

$$\frac{-\hbar^2}{2m} \nabla^2 \psi + V\psi = E\psi. \quad (\text{A5})$$

This equation is the time-independent Schrodinger equation, an equation which will be referred to often in this section.

The basic assumption for any shell model is that despite the strong overall interaction between nucleons which provides the binding energy of the nucleus, the motion of each nucleon is practically independent of that of any other nucleon. Each nucleon is then assumed to move in and under the influence of the same potential. Under this assumption, the model is known as the single-particle or independent-particle shell model. In the simplest case, the potential is assumed to be spherically symmetric in nature. Under this condition, Schrodinger's time-independent equation, Eq. (A5), may be expressed in spherical coordinates (Fig. A1) r, θ, ϕ , as (86,87)

$$\begin{aligned} \frac{1}{r^2} \frac{\partial}{\partial r} \left(r^2 \frac{\partial \psi}{\partial r} \right) + \frac{1}{r^2 \sin \theta} \frac{\partial}{\partial \theta} \left(\sin \theta \frac{\partial \psi}{\partial \theta} \right) \\ + \frac{1}{r^2 \sin^2 \theta} \frac{\partial^2 \psi}{\partial \phi^2} + \frac{2m}{\hbar^2} (E - V(r))\psi = 0 \end{aligned} \quad (\text{A6})$$

where now $\psi = \psi(r, \theta, \phi)$ and the potential $V(r)$ is a function of r exclusively.

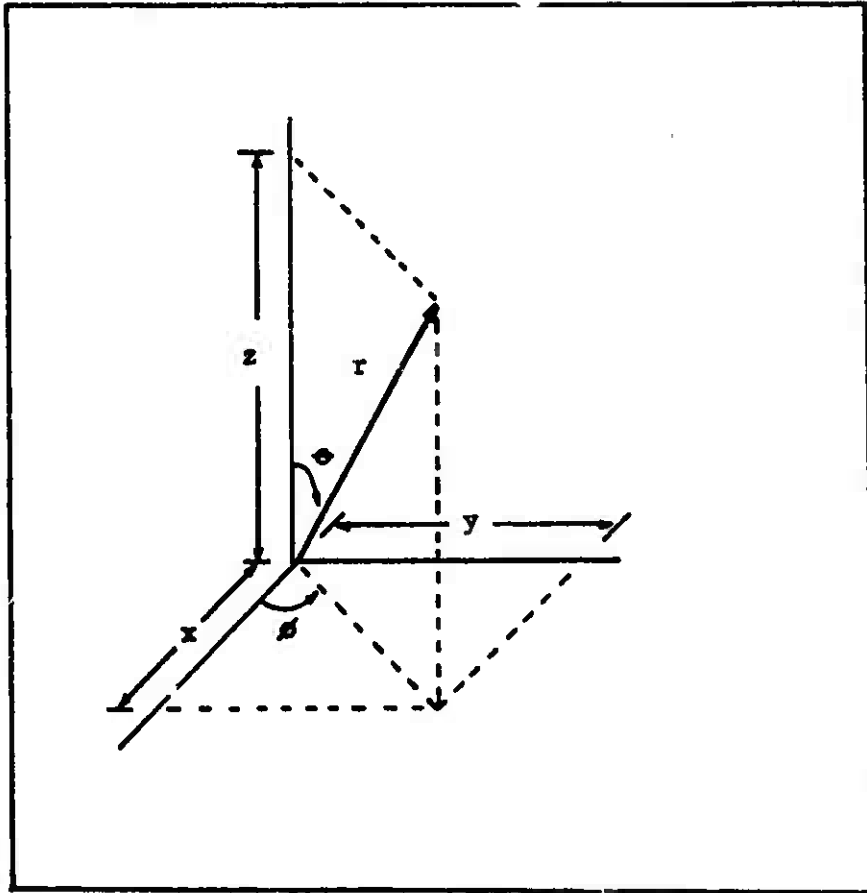


Figure A1. Spherical coordinates.

Equation (A6) may be readily separated into three independent equations, each involving only one coordinate

$$\psi(r, \theta, \phi) = R(r)\Theta(\theta)\Phi(\phi) \quad (\text{A7})$$

where R , Θ , and Φ depend only on r , θ , and ϕ respectively. Carrying out the separation and defining separation constants m_ℓ^2 , $\ell(\ell + 1)$, where m_ℓ and ℓ are to be defined shortly, yields three differential equations each a function of a single variable (87)

$$\frac{d^2\Phi}{d\phi^2} + m_\ell^2\Phi = 0 \quad (\text{A8})$$

$$\frac{1}{\sin\theta} \frac{d}{d\theta} \left(\sin\theta \frac{d\Theta}{d\theta} \right) + \left[\frac{\ell(\ell+1) - m_\ell^2}{\sin^2\theta} \right] \Theta = 0 \quad (\text{A9})$$

$$\frac{1}{r^2} \frac{d}{dr} \left(r^2 \frac{dR}{dr} \right) + \left[\frac{2m}{\hbar^2} (E - V(r)) - \frac{\ell(\ell+1)}{r^2} \right] R = 0 \quad (\text{A10})$$

The solution of Eq. (A8) along with the condition that Φ must be single-valued at a given point in space results in the condition that m_ℓ be either 0 or a negative or positive integer. Equation (A9) has a rather complicated solution in terms of associated Legendre functions which exist only when the constant ℓ is an integer equal to or greater than the absolute value of m_ℓ . The above requirements can be expressed as conditions on m_ℓ such that

$$m_\ell = -\ell, -\ell + 1, \dots, 0, \dots, \ell - 1, \ell \quad (\text{A11})$$

and on ℓ such that

$$\ell = 0, 1, 2, 3, \dots \quad (\text{A12})$$

The constants m_ℓ and ℓ are known as the magnetic quantum number and the orbital quantum number, respectively. Quantum numbers describe the "state" of a nucleon. Similarly to atomic physics, for $\ell = 0, 1, 2, 3, 4, 5$ the spectroscopic notation s, p, d, f, g, h is used. From Eq. (A11) it is evident that for a given orbital quantum number ℓ , the magnetic quantum number, m_ℓ , may take on one of the $2\ell + 1$ values. These values correspond to the $2\ell + 1$ possible orientations of the angular momentum vector of a nucleon when in the presence of a magnetic field. A p-state ($\ell = 1$) nucleon, for example, may have any one of three magnetic sublevels: $m_\ell = -1, 0, \text{ or } 1$. A third quantum number, commonly denoted by m_s or s , has been called the intrinsic spin. It describes the direction of the nucleon's spin and may take on the values $m_s = \frac{1}{2}$ or $m_s = -\frac{1}{2}$.

The radial wave equation, Eq. (A10), can be transformed into a form which is analogous to a simple one-dimensional wave equation (86). To accomplish this, the so-called modified radial wave function, $\chi(r)$, defined by

$$\chi(r) = rR(r) \quad (\text{A13})$$

is substituted into Eq. (A10). The radial wave equation then becomes simply (after rearranging)

$$\left[\frac{-\hbar^2}{2m} \frac{d^2}{dr^2} - V(r) + \frac{\ell(\ell + 1)\hbar^2}{2mr^2} \right] \chi = E\chi \quad (\text{A14})$$

Solution of this equation requires knowledge of the exact shape of the potential function $V(r)$.

The radial shape of the nuclear field is well-known from scattering experiments, but its use in Eq. (A14) makes the solution of the

Schrodinger wave equation extremely complicated. Therefore, simpler forms of the potential, $V(r)$, commonly are used. The choice of the potential form is restricted by two rather stringent conditions (88):

1. Since $V(r)$ represents the actions of the other nucleons and the nucleon density at the point $r = 0$ is not essentially different from that at any other place inside the nucleus, $V(r)$ at $r = 0$ is not expected to be singular. Furthermore, since $V(r)$ is spherically symmetric,

$$\left[\frac{dV(r)}{dr} \right]_{r=0} = 0 \quad (\text{A15})$$

2. The potential must go to zero rather abruptly at the nuclear surface, that is when r approaches the nuclear radius

$$\left[\frac{dV(r)}{dr} \right] > \left| \frac{V}{r} \right| \text{ for } r \rightarrow R. \quad - (\text{A16})$$

There are two well-known potentials that satisfy those conditions: the square well and the harmonic oscillator potentials.

The square well potential has the form

$$V(r) = \begin{cases} -V_0 & r \leq R \\ 0 & r > R \end{cases} \quad (\text{A17})$$

The shape of the square well potential is presented in Figure A2a. A solution to Eq. (A14) when $V(r)$ is given by Eq. (A17) is sought; that is,

$$\left[\frac{-\hbar^2}{2m} \frac{d^2}{dr^2} - V_0 + \frac{\ell(\ell+1)\hbar^2}{2mr^2} \right] \chi = E\chi \quad (\text{A18})$$

When $\ell = 0$ (s states), the problem reduces to that of a particle in a box

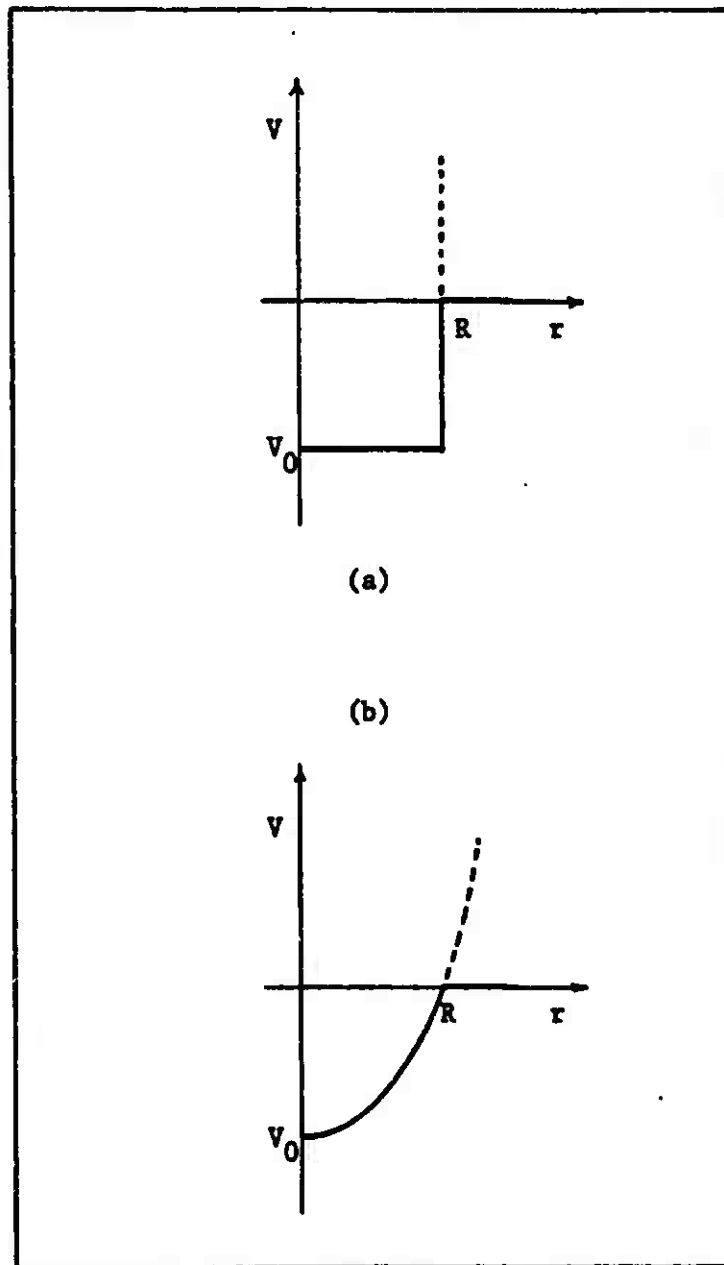


Figure A2. The square well (a) and harmonic oscillator (b) potentials.

of sides R and potential within of $-V_0$. The energy eigenvalues which result are given by

$$E_{n\ell} = -V_0 + \frac{n^2 \pi^2 \hbar^2}{2mR^2} \quad (\text{A19})$$

where n , the radial quantum number, is the number of nodes of Eq. (A13). When $\ell > 0$, the situation is more complicated. Solutions are given by a set of functions known as spherical Bessel functions of order ℓ (89,90)

$$J_\ell(kr) = (-1)^\ell \left(\frac{r}{k}\right)^\ell \left(\frac{1}{r} \frac{d}{dr}\right)^\ell \frac{\sin kr}{kr} \quad (\text{A20})$$

where the $J_\ell(kr)$ are the spherical Bessel functions of order ℓ and the constant k is given by

$$k^2 = 2nE/\hbar^2 \quad (\text{A21})$$

The energy levels resulting from Eqs. (A19-A21) are shown in Figure A3a. Each level is $2(2\ell + 1)$ orientationally degenerate. The numbers in parentheses above each energy level of Figure A3a correspond to the accumulated total of nucleons resulting in subshell closures up to that level. These are 2, 8, 18, 20, 34, 40, 58, etc. and, with the exception of 2, 8, and 20, do not correspond to the experimentally obtained "magic numbers" 2, 8, 20, 28, 50, 82, and 126, corresponding to the number of protons or neutrons in the nuclei of particularly stable elements.

The harmonic oscillator potential has the form

$$V(r) = \begin{cases} -V_0 [1 - (r/R)^2] & r \leq R \\ 0 & r > R \end{cases} \quad (\text{A22})$$

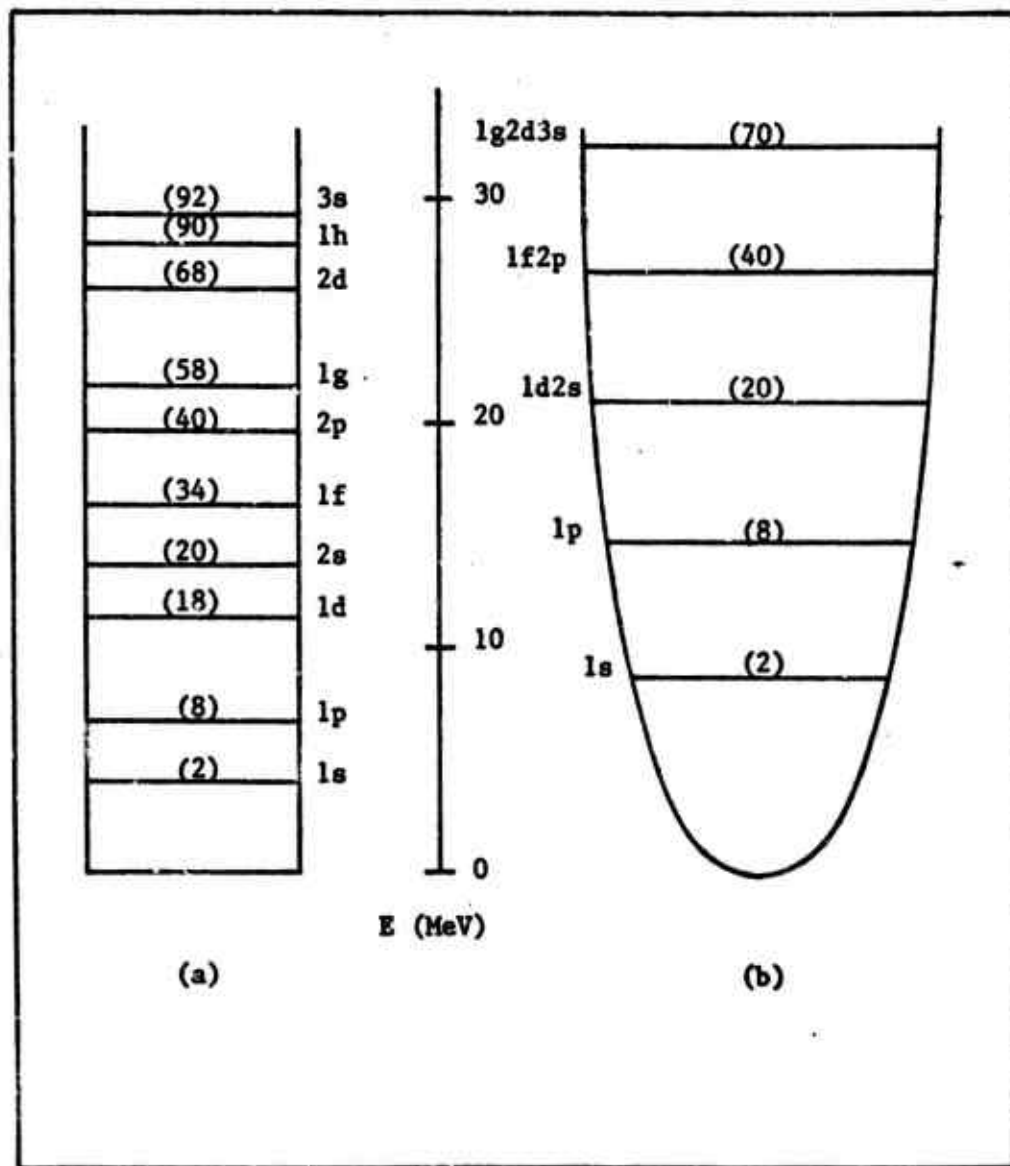


Figure A3. Energy levels due to an infinite square well (a) and a harmonic oscillator (b) potential.

The shape of the harmonic oscillator potential is shown in Figure A2b. Solutions (91) of the radial wave equation [Eq. (A14)], when the potential is given by Eq. (A22)

$$\left[\frac{-\hbar^2}{2m} \frac{d^2}{dr^2} - V_0 \left(1 - \frac{r^2}{R^2}\right) + \frac{\ell(\ell+1)}{2mr^2} \right] \chi = E\chi \quad (\text{A23})$$

result in energy eigenvalues given by (88)

$$E_{n\ell} = [2(n-1) + \ell]\hbar\omega + \frac{3\hbar\omega}{2} - V_0 \quad (\text{A24})$$

where

$$\omega = (2V_0/mr^2)^{1/2} \quad (\text{A25})$$

The energy levels resulting from Eqs. (A24-A25) are depicted in Figure A3b. Note that in addition to the $2(2\ell+1)$ orientational degeneracy, except for the first two levels, this level scheme has "accidental" degeneracy between levels of different n and ℓ . Note also that after the first two levels, each subsequent oscillator shell begins with ℓ larger by one unit and contains all ℓ values of the same parity (a symmetry operator having to do with wave function evenness/oddness) down to the lowest one. As in Figure A3a, the numbers in parentheses (2, 8, 20, 40, 70, 112) represent the total occupation number of all lower levels up to the one under consideration (inclusive). With the exception of the first three occupation numbers (2, 8, 20), again the magic numbers (2, 8, 20, 28, 50, 82, 126) are not reproduced.

So far the classification of levels has been based only on the orbital momentum quantum number ℓ , under the assumption that spin-orbit

interactions play only an unimportant role. This is so in the atomic case, where this interaction causes only a slight splitting of the levels $j = \ell \pm \frac{1}{2}$ which is small compared to the distance between levels of different ℓ . In the nuclear realm, however, experimental evidence has revealed the presence of a strong interaction between orbital angular momentum and intrinsic spin angular momentum which may cause a rather large splitting of energy levels that may no longer be insignificant when compared to the distances between levels of different ℓ .

A spin-orbit coupling model has been suggested in which there is a strong spin-orbit interaction, proportional to $L \cdot S$, in addition to the potential $V(r)$, acting on a nucleon in the nucleus. The magnitude of this spin-orbit interaction depends on, in addition to the magnitude of the orbital angular momentum vector, the relative orientation of the spin and the orbital angular momentum vectors. The spin-orbit interaction in this case (in contrast to the atomic case) is inverted, which means that a nucleon in a $j = \ell + \frac{1}{2}$ state has less energy than a nucleon in a $j = \ell - \frac{1}{2}$ state. Since the energy of a level depends strongly on the alignment of spin and orbit, it is no longer justifiable to characterize a level simply by its ℓ value. The total angular momentum j must be specified also.

The level sequence, a harmonic oscillator potential [Eq. (A22)] modified by strong spin-orbit coupling, is shown in Figure A4 (88). Owing to the spin-orbit coupling, the nuclear shells are not the same as the oscillator shells. It is seen that in the three lowest oscillator levels groups (1s, 1p, 2ald) the grouping is not appreciably changed. Hence, the lower shell occupation numbers (2, 8, 20) are not affected by

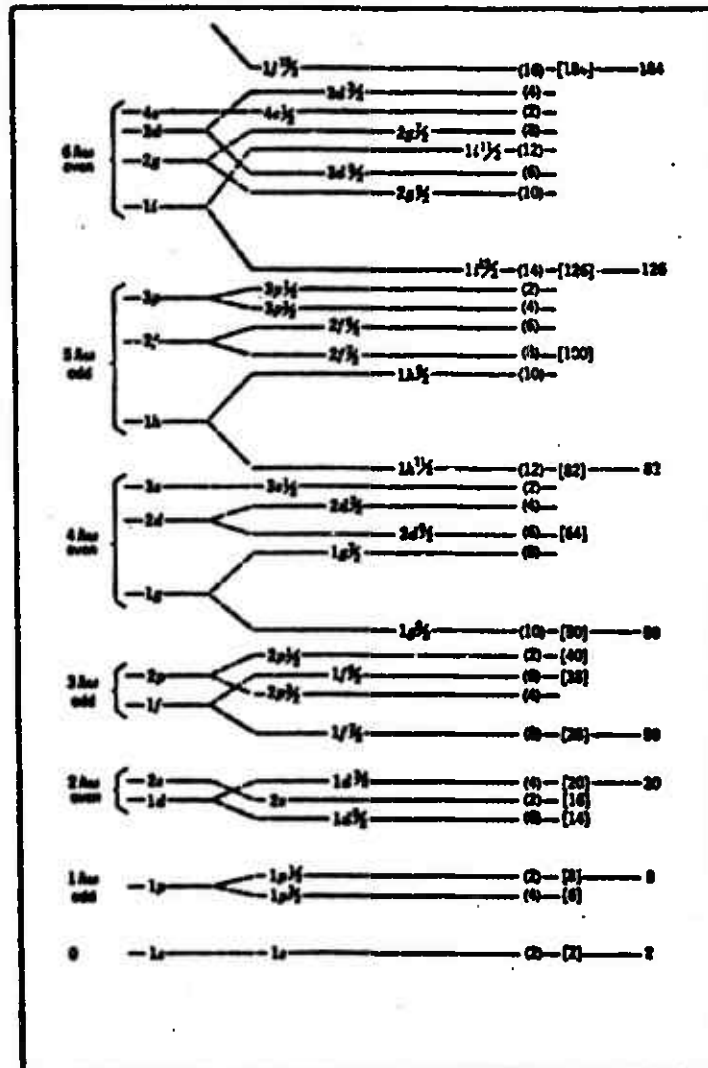


Figure A4. Harmonic oscillator energy levels with spin-orbit coupling. Ref. (88).

the spin-orbit splitting. However, the level $1f_{7/2}$ of the next oscillator level group is appreciably lowered and is brought into isolation from the other levels which indicates shell closure at occupation number 28. Still more drastically, the $1g_{9/2}$ level from the $4\hbar\omega$ oscillator group is brought down close to the preceding oscillator group producing a wide gap after occupation number 50. Here the spin-orbit splitting clearly becomes the dominant feature in the level arrangement. Thus, the spin-orbit coupling reproduces all magic numbers exactly as can be evidenced from Figure A4.

Although the spin-orbit shell model of nuclear structure provides a sound explanation for many nuclear phenomena which are experimentally observed, the simple model given above is not sufficient. For example, the model cannot explain why any even number of identical nucleons couples to zero ground state spin. Evidently there must be a nucleon-nucleon interaction which favors the pairing of nucleons with opposing angular momenta. An attractive interaction between nucleons must therefore be added to the single-nucleon spin-orbit interaction, which gives rise to a pairing energy. From theoretical considerations, it appears likely that the magnitude of the pairing energy increases with the ℓ value of the pair and that for this reason the high-spin states predicted by the spin-orbit model are not found in odd- A ground state spins (85).

Another feature not included in the simple shell model is the distorting effect of the outermost nucleons on the other nucleons in a nucleus. Suppose a single nucleon is added to a closed shell nucleus. This nucleon will usually have a high ℓ value and therefore its wave function will peak close to the nuclear radius. In terms of a classical

picture the nucleon circles around a closed shell nuclear core. The attraction between the nucleon and the core distorts the core. If more nucleons are added outside of the core, a point will be reached when it is permanently deformed with an accompanying effect on the orbits. The deformation may result in a nucleus of ellipsoidal shape. A quantum-mechanical body which has an axis of symmetry such as an ellipsoid of revolution can undergo rotations about an axis perpendicular to the symmetry axis. The energy spectrum of such a "rotator" is quite characteristic (85). There are many cases of even-even nuclei in which this spectrum has been found. This leads to the conclusion that deformed nuclei indeed exist.

In any finite potential well there are bound energy levels, corresponding to states of energy $E < 0$ [assuming $V(r \rightarrow \infty) = 0$], and unbound or virtual levels of states of energy $E > 0$. Virtual states result from the fact that the deBroglie wave of a nucleon is reflected at the edge of the potential well even though its total energy may exceed the potential energy in the well. Thus, approximately-standing waves are formed within the potential well, the amplitude of the wave function can be very large within the well, and a virtual state occurs. A nucleon may vacate a virtual state after some mean life τ , causing it to have a width for particle emission Γ given by

$$\Gamma = \hbar/\tau \quad (\text{A26})$$

A virtual state may also decay to a lower state by gamma-ray emission. Bound levels, on the other hand, may decay only by gamma emission.

According to the single particle shell model, a given nucleus

(Z,N) consists of Z protons and N neutrons each placed into bound levels of increasing energy in accordance with the Pauli exclusion principle. In the ground state of the nucleus, all nucleons are in their lowest energy states. The simplest excited states of the nucleus are formed by raising the outermost nucleon to a higher state. The corresponding excitation spectrum of the nucleus is called the single particle level spectrum with levels as shown in Figure A4. However, upon inspection of actual level spectra, many more levels than expected from the single-particle spectrum are observed. Present theories indicate that the single-particle spectrum is actually "dissolved" among many levels each of which consists of complicated excitations of more than one particle (85).

APPENDIX B

Transitions Between Quantum Mechanical States

In the quantum mechanical treatment used to explain nuclear structure (Appendix A), the simplifying assumption that the potential energy term, V , of the Schrodinger equation was constant in time was made. This assumption was necessary to allow separation of the complete equation into time-dependent and time-independent equations. Use was made of the time-independent equation, Eq. (A5), and time-invariant expressions for nuclear potentials to obtain energy states that were necessarily constant in time. No explanations concerning transitions of any kind from one state to another were provided. In order to describe transitions and allowed states, quantum mechanical perturbation theory is employed.

The cases in which the Schrodinger equation, Eq. (A1), can be solved exactly are extremely rare. Perturbation theory is the most important method for obtaining approximate solutions to Schrodinger's equation. The method is applicable to any situation in which the Hamiltonian H (see below) describing the system under consideration is not much different from the Hamiltonian H_0 , describing some similar system simple enough so that solutions to the Schrodinger equation are known exactly (89).

The Hamiltonian, or total energy operator, H given by

$$H = \frac{-\hbar^2}{2m} \nabla^2 + V \quad (B1)$$

is simply the operator on the left-hand side of Eq. (A1). When a system is perturbed (such as in the emission or absorption of electromagnetic radiation), its total Hamiltonian, H , is affected and

$$H = H_0 + H' \quad (B2)$$

where H_0 is that part of the Hamiltonian that permits calculation of the

properties of the allowed states of the system and H' is the effect of the perturbation on the Hamiltonian.

The operator H' may be thought of as "inducing transitions from one allowed state to another" (84). If the initial state of the system (prior to transition) is labeled ψ_i and the final state of the system (after the transition) is labeled ψ_f , then a measure of how much the wave function $H'\psi_i$ is like the wave function ψ_f is given by the overlap integral

$$M = \langle \psi_f | H' \psi_i \rangle = \int \psi_f^* H' \psi_i d\tau \quad (B3)$$

where $d\tau$ is an element of volume and the integral is over all space. The quantity M is called the "transition matrix element." The matrix element is an important quantity since its square is proportional to the probability that the perturbation will transform the state described by ψ_i to the state described by ψ_f . The matrix element contains the wave functions of the states between which the transition occurs. It is therefore the quantity that determines the effect of the spins, parities, and detailed structures of the two states on the transition probability.

To calculate the probability for a transition, an expression for H' is needed. H' is the energy of the interaction between the electric and magnetic fields associated with the incoming photon and those associated with the target nucleus. These electric and magnetic fields may be expressed as an expansion in terms of their component electric and magnetic multipoles. This expansion may be better illustrated by reference to Figure B1. The electrostatic potential V at the point P due to a proton of charge e at the point (r, θ) is (84)

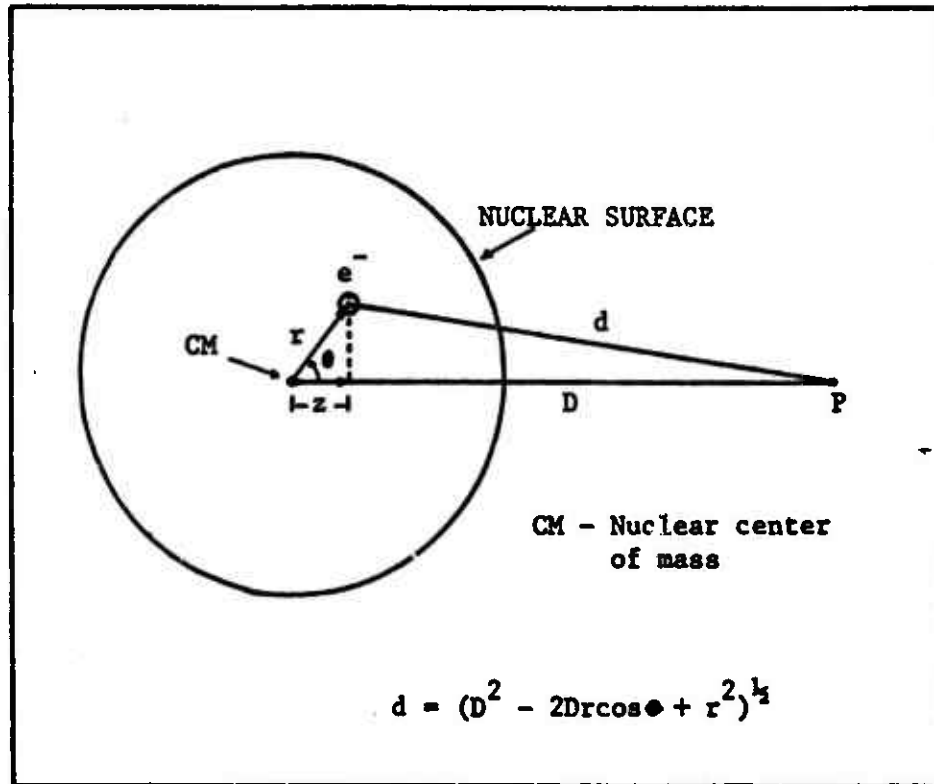


Figure B1. Definition of quantities relevant to the discussion of nuclear electric multipoles.

$$V = \frac{1}{4\pi\epsilon_0} e / \left[D \left[1 - (2r/d)\cos\theta + r^2/D^2 \right]^{1/2} \right]. \quad (\text{B4})$$

This equation is usually expressed in terms of the Legendre polynomials $P_n(\cos\theta)$ using the identity

$$\sum_{n=0}^{\infty} \left(\frac{r}{d} \right)^n P_n(\cos\theta) = 1 / \left[1 - (2r/D)\cos\theta + r^2/D^2 \right]^{1/2} \quad (\text{B5})$$

in which case the expression for V becomes

$$V = \frac{1}{4\pi\epsilon_0} \frac{e}{D} \left[\sum_{n=0}^{\infty} \left(\frac{r}{D} \right)^n P_n(\cos\theta) \right]. \quad (\text{B6})$$

This equation is the electric multipole expansion. To calculate the potential at P due to all protons in the nucleus, it is necessary to sum the potential at P due to each separately. After summing the potential at P due to all Z protons in a nucleus, the first term of Eq. (B6) becomes Ze/D , the electrostatic potential that would result by a total charge Ze located at the nuclear center of mass. The second term of the expansion becomes proportional to

$$\sum_1^z e r \cos\theta = \sum_1^z e z. \quad (\text{B7})$$

This quantity is the electric dipole moment. The third term of the expansion gives the electric quadrupole moment, the fourth the electric octupole, and so on. A similar expansion can be made for the magnetic multipoles.

For each term of the multipole expansion of H' , a matrix element

can be calculated such that the square of its absolute value is proportional to the probability that the transition occurred by interaction of the photon field with that particular electric or magnetic multipole moment of the nuclear field. The total probability of a transition per unit time depends on the squares of the values of all the electric and magnetic multipole transition matrix elements between the initial and final nuclear states.

There are certain simple rules that determine which matrix elements may contribute to the transition in the particular case. The electric L-pole (EL) matrix elements and the magnetic L-pole (ML) matrix elements are always zero unless the spins of the initial and final states differ vectorially by L units of angular momentum. In other words, electric dipole (E1) or magnetic dipole (M1) transitions may occur only between states of spin differing by one unit of angular momentum, quadrupole transitions (E2 and M2) may occur only between states differing by two units of angular momentum, etc. Thus, if J_i and J_f represents the spins of the initial and final states, respectively, and 2^L indicates the pole order ($L = 1$, dipole; $L = 2$, quadrupole; $L = 3$, octupole; and so on), the first transition "selection rule" is

$$[J_i - J_f] \leq L \leq J_i + J_f . \quad (B8)$$

The second transition selection rule is that of conservation of parity. An electric multipole has even parity when L is even and odd parity when L is odd. Magnetic multipole radiation has odd parity when L is even and even parity when L is odd. In general, parity of electric multipoles is $\pi = (-1)^L$, and parity for magnetic multipoles is $\pi = -(-1)^L$

where +1 means even parity and -1 means odd parity (92). If the parity of the initial state is denoted by π_i and the parity of the final state is given by π_f , then if a particular radiation multipole has a parity change π_r , conservation of parity would require that

$$\pi_i = \pi_f \pi_r . \quad (\text{B9})$$

This is the second transition selection rule. Transitions are forbidden between two levels which both have spin zero. Table B1 (92) summarizes the transition selection rules.

The transition rate, λ_{if} , between an initial and a final state is given by "Fermi's Golden Rule #2"

$$\lambda_{if} = \frac{2\pi}{\hbar^2} |M|^2 \frac{dN}{dE} . \quad (\text{B10})$$

In this expression M is the transition matrix element and dN/dE is the number of final states per unit energy. Blatt and Weisskopf (93) have estimated electric multipole and magnetic multipole transition rates (λ_{EL} and λ_{ML}) based on the independent particle shell model of the nucleus. The expressions they obtained are (85,92)

$$\lambda_{EL} = 2\pi\nu \frac{e^2}{c} S \left(\frac{R}{\lambda} \right)^{2L} \quad (\text{B11})$$

and

$$\lambda_{ML} = 10 \left(\frac{\hbar^2}{McR} \right) \lambda_{EL} \quad (\text{B12})$$

where ν is the radiation frequency, e is the electron charge, R is a linear dimension characterizing nuclear size, λ is the radiation's reduced

Table B1Transition Selection Rules

Classification	Symbol	Change in Angular Momentum	Parity Change
Electric dipole	E1	1	Yes
Magnetic dipole	M1	1	No
Electric quadrupole	E2	2	No
Magnetic quadrupole	M2	2	Yes
Electric octupole	E3	3	Yes
Magnetic octupole	M3	3	No
Electric 2^L - pole	EL	L	No (L even) Yes (L odd)
Magnetic 2^L - pole	ML	L	Yes (L even) No (L odd)

wavelength ($k = \lambda/2\pi$), c is the velocity of light, M is the nucleon mass and S is a statistical factor that depends on L and is shown in Table B2 (92).

Inspection of Eqs. (B11,B12) reveals the relative proportions each multipole may contribute to a given transition. In general, the transition rate of the multipole of lowest order usually exceeds that of all the other multipoles by a factor of at least 10^2 to 10^4 (85). Additionally, for a given value of L , electric multipole radiation is more probable than magnetic multipole radiation by a factor of approximately $4.4A^{2/3}$ (92).

Table B2

Values of the statistical factor S
as a function of multipole order L.

L	S
1	$(2.5) 10^{-1}$
2	$(4.8) 10^{-3}$
3	$(6.3) 10^{-5}$
4	$(5.3) 10^{-7}$
5	$(3.1) 10^{-9}$

APPENDIX C

Principles of Electron Linear Accelerator Operation

The linear accelerator used in this study was a Sagittaire/Therac 40 electron linear accelerator manufactured by CGR-MeV in France (94). This accelerator is a disk-loaded, traveling-wave clinical machine. The description presented in this Appendix pertains to traveling-wave accelerators like the Sagittaire. The discussion, however, has been kept of sufficient generality to apply to any traveling-wave clinical machine.

An electron linear accelerator is a device that accelerates electrons by virtue of an axial electric field. When the energy at injection is negligible, the final electron kinetic energy obtained is given by

$$T_e = \int_0^L (eE_z \cdot dl) \quad (C1)$$

where T_e = electron kinetic energy, e = electron charge, E_z = axial electric field, dl = increment in length, and L = accelerating tube length. The required axial electric field is provided by electromagnetic waves of microwave frequency, commonly 3000 MHz.

Evolution of the modern electron linear accelerator has been made possible by the development of high-power radiofrequency generators and specially designed microwave cavities and waveguides. Because of the important role of microwave technology in linear accelerators, a description of microwave cavities, waveguides, and power sources will be provided in the succeeding paragraphs (95-97). Also included is a discussion of the principles of electron acceleration by microwaves with particular emphasis placed on traveling-wave high-energy electron linear accelerators. Components characteristic of medical accelerators also will be described.

Microwave cavities and guides support certain specific electromagnetic wave configurations and are used in microwave power generation, microwave transport, and for electron acceleration. Energetic electrons can generate microwave power by exciting the cavities of microwave power amplifiers such as the klystron. On the other hand, a linear array of cavities can accelerate electrons by transferring electromagnetic energy from the cavity fields to an electron beam. Microwave cavity geometry and dimensions determine the particular application of the cavity. Rectangular waveguides are used primarily for high-power microwave energy transport while cylindrical cavities are used in microwave power amplification and electron acceleration.

The rectangular waveguide is the principal means by which microwave energy is transported long distances. Rectangular waveguides are used to transmit microwaves from the power amplifier to the electron acceleration section of a linear accelerator. This type of waveguide is operated in what is known as the transverse electric (TE) mode. In the TE mode, the electromagnetic wave has no electric field component in the direction of travel. Although microwave guides in general will transport waves of an infinite number of resonant frequencies, guide dimensions are designed for transport in the most convenient frequencies. In many cases this is the TE_{10} mode. The power transported is given by the vector cross product of the transverse electric field and the magnetic field intensity.

Cylindrical cavities, in electron linear accelerators, are used in both microwave power amplification and in electron acceleration. Similarly to the rectangular cavity, the lowest frequency, and most dominant, modes often are used. Cylindrical cavities are generally operated in what

is called the transverse magnetic mode, TM_{01} . This mode, characterized by an axial electric field and an azimuthal magnetic induction, is particularly suitable for transferring power to electron beams. In addition, microwave power amplification is usually accomplished in high-energy accelerators by the klystron, a device utilizing TM_{01} -mode cylindrical cavities.

The klystron, in its simplest form, consists of two interconnected cylindrical cavities, the first of which is called a buncher and the second a catcher. Microwaves from a radiofrequency oscillator are transported to the buncher cavity of the klystron. Electrons, thermionically emitted from a hot filament, enter the buncher cavity and are grouped or "bunched" by the alternating axial electric field. Bunched electrons are accelerated further by a DC field and travel through a drift tube to the catcher cavity. The catcher cavity, resonant at the arrival frequency of the electron bunches, extracts a large portion of the electron kinetic energy converting it to electromagnetic energy. As a result, microwaves of increased amplitude are produced. Even greater power amplification can be accomplished by klystrons of multiple cavities.

The cylindrical waveguides used for electron acceleration may be thought of as a linear array of many cylindrical cavities. This is accomplished by introducing circular "washer-shaped" disks called irises. Iris-loading of the cylindrical waveguide is necessary to reduce the phase velocity of the traveling wave in the waveguide to less than the velocity of light. This permits the coupling of the traveling-wave energy to the electrons under acceleration. The phase velocity of the traveling wave varies linearly with the spacing between the irises, thus, close iris

spacing means smaller phase velocity. On the other hand, because the axial electric field in the waveguide accelerates the electrons, iris spacing must be increased along the length of the waveguide so that the microwave phase velocity increases in synchrony with the electron velocity thus establishing phase stability. Eventually, as the electron velocity approaches the velocity of light, iris spacing becomes constant. Consequently, electrons injected into an iris-loaded cylindrical waveguide of proper dimensions are accelerated to kinetic energies which depend upon the magnitude of the axial electric field and the length of the accelerating guide as shown in Eq. (C1).

The remaining paragraphs describe the operation and the major components of a typical traveling-wave medical linear accelerator. This description is best provided by reference to Figure C1 which depicts, schematically, the basic components. The accelerator shown on Figure C1 and subsequently described possesses two acceleration sections and a phase-shifter component which are not typical of smaller linear accelerators. The basic accelerator may be divided into three major components: the microwave power supply component, the electron injector and accelerator section, and the gantry and treatment head components.

Microwave power is provided by an oscillator, which supplies 3000 MHz (in S-band accelerators) low-power microwaves, and a microwave amplifier, in this case a klystron. Pulses from a 100 Hz oscillator, which serves as a "traffic director" in the accelerator, control a modulator which in turn controls a high-power switching device called a thyretron. The thyretron transfers high-voltage DC power to the klystron. At the same time the 3000 MHz oscillator delivers microwaves to the klystron for

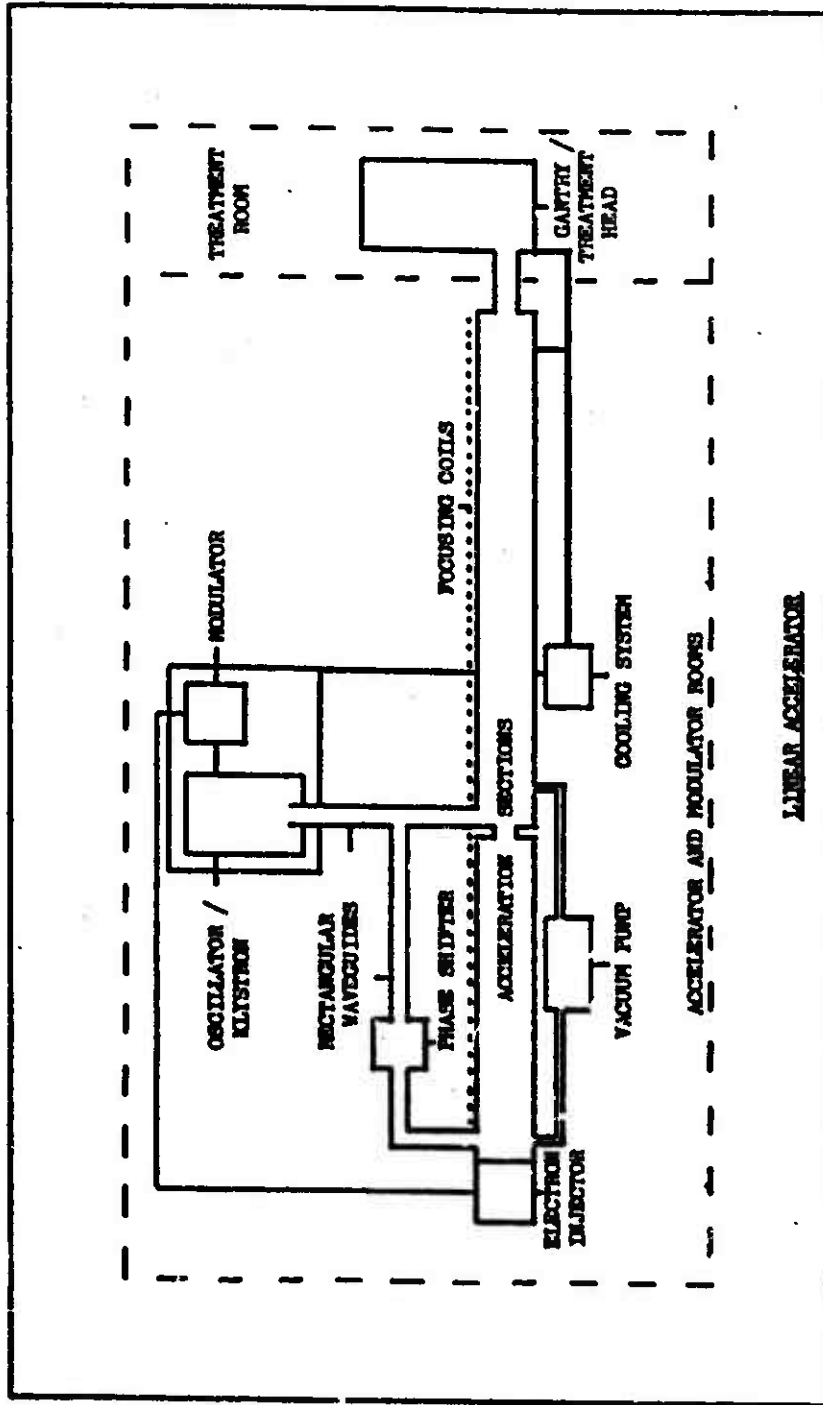


Figure C1. Block diagram of linear accelerator.

amplification. The amplified microwaves from the klystron are transported to the acceleration section by means of rectangular waveguides filled with a dielectric gas such as SF_6 .

The acceleration section consists of iris-loaded cylindrical waveguides. Electrons are injected into the acceleration guides by an electron gun which delivers electron pulses at repetition rates also controlled by the 100 Hz oscillator. The electrons are then accelerated by the amplified 3000 MHz microwaves traveling through the waveguide. The increase in electron momentum is given by (97)

$$\frac{dp}{dt} = eE_{oz} I_0(\alpha r) \cos\phi \quad (C2)$$

where dp/dt is the time rate of change of the electron momentum, e is the electron charge, E_{oz} is the amplitude function for the axial electric field, $I_0(\alpha r)$ is a modified Bessel function of the argument αr , and ϕ is the phase angle. The variable r describes the radial dimension in the accelerating cylindrical waveguide. The final electron kinetic energy, as can be seen from the above expression, is a function of the time the electron experiences the influence of the electric field (and hence total waveguide length), the magnitude of the axial electric field, and of the value of the $\cos\phi$ term which has to do with the phase coupling of the traveling waves in the guide.

In the accelerator shown in Figure C1, electron endpoint energy is controlled primarily by varying the relative phase between traveling waves in the two accelerating sections. This is accomplished by changing the phase velocity of the traveling wave in that part of the rectangular waveguide which feeds the first acceleration section. The component

called the phase-shifter performs this task. The phase-shifter consists of a quartz rod and a mechanism capable of adjusting continuously the penetration distance of the rod into the rectangular waveguide feeding section 1. The degree of penetration determines the dielectric constant of that section of the waveguide thus establishing the phase velocity of the wave in that region and shifting the relative phase of the microwaves in the first section with respect to the second section. Adjusting the phase-shifter changes the phase angle ϕ for the electrons in the second acceleration section and changes the electron momentum gain. In addition, magnetic induction coils are wrapped around both accelerating sections in order to focus the electrons into an electron beam along the centerline of the sections.

Accelerated electrons enter the gantry and therapy head section of the linac where the beam undergoes the necessary modifications required to produce an electron or bremsstrahlung beam. The gantry contains a series of bending magnets and quadrupoles that transport and steer the electron beam and analyze the energy. The gantry also serves to support the therapy head which contains components such as the variable collimators, the bremsstrahlung target and beam-flattening filter.

Upon entering the gantry, the electron beam energy is analyzed by means of a bending electromagnet and energy slit system (94). For a given magnetic field, electrons possessing certain discrete energies are deflected through some definite angle. Only electrons with energies within a certain percentage of a mean energy are transmitted through the energy slit opening. Microwave power is controlled by a servo energy slit system such that the electron beam energy is always adjusted to the

energy appropriate for transmission through the slit. Electron endpoint energy selection determines the magnetic field intensity by establishing the magnet deviation current. The resultant electron beam energy, T , is given by (59)

$$(T^2 + 2mc^2T)^{1/2} = Ber \quad (C3)$$

where T is the electron kinetic energy, m is the electron mass, e is the electron charge, c is the speed of light, B is the magnetic induction, and r is the electron orbit radius. After energy analysis, the electron beam is redirected by means of additional bending magnets to a direction perpendicular to the acceleration waveguide. The beam then enters the therapy head.

The linac therapy head contains the elements that perform the final beam modifications prior to its exit from the accelerator. These are the fixed and variable beam collimators which restrict the beam size, a removable target which allows bremsstrahlung beam production, a beam flattening filter which creates a uniform beam intensity in a plane perpendicular to the beam axis, and an ionization chamber system whose purpose is to monitor beam position and intensity.

The ionization chamber system consists of two pancake-type ionization chambers each divided diametrically in two. The chambers are stacked one on top of the other such that the beam traverses both of them. The chambers also are rotated 90° with respect to each other such that each of the four halves can be used to monitor the intensity of the beam in one of four perpendicular directions. The signals from each of the four halves are used as input to servo controls for beam-steering

magnetic quadrupoles, located in the gantry. These set to center the beam. In addition to other uses, the ionization chambers' current is compared to a standard current supply and the electron gun current is automatically adjusted so that the beam intensity remains constant. Finally, the ionization chambers serve to monitor the total integrated radiation dose delivered.

APPENDIX D

Semiconductor Detector Spectrometer Systems

Gamma-ray spectrometers are radiation measurement systems used to determine the energy spectrum and fluence of gamma- or x-ray-emitting radioisotopes. Semiconductor detector systems are particularly well-suited for this purpose. They possess the advantageous characteristics of high sensitivity and superior energy resolution which allow accurate spectroscopic measurement.

In this appendix, the general characteristics of semiconductor materials and the application of these materials to radiation detection are reviewed (63,98-103). The components and basic principles of pulse-height spectrometry systems also are described. Particular emphasis is placed on intrinsic germanium semiconductor detectors and on multichannel pulse-height analysis systems.

In many radiation detection applications, such as gamma-ray spectroscopy, the use of a solid detection medium is preferred over a gas-filled chamber because of the increased sensitivity. The use of scintillation detectors for spectroscopy is fairly common. Their energy resolution, however, is rather limited primarily due to the large contribution that statistical fluctuations make to the information-carrying pulse. The only way to reduce the influence of statistical fluctuations on the energy resolution of a detector is to increase the number of information carriers involved in pulse production.

The use of semiconductor detectors results in a large number of information carriers per detection event and a very small amount of statistical fluctuation in the processing of the charge pulse. Thus, much better energy resolution is achieved. For this reason, semiconductor detector systems are best suited for such radiation measurement applica-

tions as gamma-ray spectroscopy where accurate determination of the photon energy is required.

Electrons in an individual atom can assume only certain discrete energy levels. When atoms are brought into close proximity, such as in a crystal structure, these discrete energy levels tend to "smear" into energy bands. The most energetic electrons which are still bound to specific lattice sites within the crystal occupy what is known as the valence band. Electrons which are free to migrate through the crystal, and thus contribute to the material's electrical conductivity, occupy even higher energy states grouped into the conduction band. The valence and conduction bands are separated by a gap of normally forbidden energy states.

The size of this band gap determines whether a material is an insulator or a semiconductor. In semiconductors the band gap energy is of the order of several electron-volts (eV), whereas insulators have band gaps greater than 5 eV (63). In the absence of thermal energy, the valence band is completely filled and the conduction band is completely empty. Because of the relatively small band gap energy of semiconductors, in the presence of induced excitations, some valence band electrons may acquire sufficient energy to cross the band gap to the conduction band. An electron, now in the conduction band, and its associated vacancy in the valence band form what is known as an electron-hole pair. The presence of electron-hole pairs, produced by ionizing radiation, changes the electrical conductivity of the material. Thus electron-hole pairs constitute the basic information carriers of semiconductor detectors.

The presence of impurities effects the conductivity of semicon-

ductors. In a high purity or intrinsic semiconductor, the number of electrons in the conduction band equals the number of holes in the valence band. In relatively pure semiconductors such as germanium and silicon, however, even minute quantities of impurities can determine their electrical properties. Impurities may be electron donors or electron acceptors depending on their valence electron number. In the case of an electron donor impurity, excess loosely-bound electrons remain after the impurity has formed covalent bonds. A semiconductor containing this type of impurity is termed n-type and its electrical conductivity is determined by the flow of electrons. If the impurity is an electron acceptor, empty covalent bond sites result in the formation of holes. In these materials, the holes determine the electrical conductivity and the semiconductor is said to be p-type.

If donor and acceptor impurities are present in a semiconductor in equal concentrations, the material is said to be compensated. Compensated semiconductor materials have some of the properties of intrinsic semiconductors, i.e. equal amounts of electrons and holes. Compensation may be accomplished by the lithium ion drifting process in which donor atoms (lithium) are added to basically p-type semiconductor materials such as germanium or silicon. The widely used $\text{Ge}(\text{Li})$ and $\text{Si}(\text{Li})$ semiconductor detectors are made in this way.

Directly-ionizing radiation deposits energy in semiconductor materials resulting in the production of electron-hole pairs. The number of electron-hole pairs or charge carriers produced is determined by the amount of energy deposited. The total number of charge carriers in the semiconductor, however, will not be determined exclusively by the energy

deposited but will also include "background" charge carriers due to thermal excitations and to the presence of even minute amounts of impurities. Background carrier concentration can be reduced by applying an electric field to the semiconductor detector region. Care must be taken when applying the field in order to be sure that charge carriers removed at one end of the semiconductor detector region are not reintroduced into the region from the other end. For this purpose, special "blocking contacts" are required. The most suitable blocking contact is the junction of p-type and n-type semiconductor materials. This junction is referred to as the p-n junction.

When a p-type semiconductor is joined to an n-type semiconductor, a concentration gradient is created in the conduction band at the junction due to the increased density of conduction electrons in the n-type material. The gradient insures that the electrons will diffuse across the junction to the p-type material. Here the electrons will combine with the holes. A similar and symmetrical argument can be made for the migration of holes from the p-type to the n-type semiconductor material. This charge migration results in a net negative space charge in the p-type side of the junction and a net positive space charge in the n-type side. The residual space charge produces an electric field which opposes further diffusion across the junction thus establishing a steady-state charge distribution. The region of the charge imbalance is called the depletion region because the concentration of electrons and holes is greatly reduced.

If an electric potential is applied across a p-n junction such that the p-type side is made negative and the n-type side is made positive, the junction is said to be reverse biased. Under this condition, the

applied potential enhances the junction's natural space charge distribution and thus increases the potential difference across the junction. This ultimately results in a wider depletion region within which charge carriers that may be produced through the action of ionizing radiation can be efficiently collected. With the potential difference the junction also functions as a blocking contact because the reintroduction of charge carriers from outside the depletion region is prevented when charge carriers produced within the region are collected. The depletion region of a reverse biased p-n junction may, therefore, act as the sensitive volume of a semiconductor radiation detector.

The width of the depletion region of a semiconductor detector is proportional to the material's electrical resistivity if the material is free from impurities. The reduced concentration of impurity in high-purity germanium (HPGe) allows the formation of relatively large depletion regions. These enlarged depletion regions increase the active volume of the semiconductor detector thus making it suitable for the detection of penetrating ionizing radiation such as gamma rays.

The semiconductor properties of HPGe tend to be p-type due to the presence of small amounts of residual acceptor impurities or to acceptor centers associated with the Ge crystal itself. The basic configuration of an HPGe detector is sometimes referred to as $n^+ - p - p^+$ where n^+ , p^+ refers to high concentration n- and p-type semiconductor materials respectively and p refers to the bulk HPGe material itself.

HPGe detectors are often fabricated in what is known as coaxial geometry in order to achieve the largest active volumes. The outer surface of the crystal (n^+ -type) is formed by lithium diffusion onto the

crystal surface. The detector's depletion region is formed by reverse-biasing this n^+p junction. The inner (p^+ -type) contact is often formed by removing the inner core of the Ge crystal, etching the inner surface and then evaporating either gold or aluminum for electrical contact (63). If the reverse-biasing voltage is high enough, the entire p-region of the detector becomes totally depleted thus resulting in an active volume almost equal to the size of the crystal itself.

Germanium detectors are operated at cryogenic temperatures. This is necessary to minimize leakage current. Current due to thermally-generated charge carriers may constitute the largest source of leakage current. Germanium detectors are specially susceptible to leakage current because of the lower band gap energy, 0.67 eV. The current observed at the edges of a reverse-biased junction when a high voltage is applied constitutes another source of leakage. This current, called surface leakage, is negligibly small provided the detector has good encapsulation.

The charge carriers produced in an ionization or excitation event in a semiconductor detector produce a voltage pulse whose amplitude is directly proportional to the amount of energy deposited in the detector. An electronic system that is capable of discriminating and recording the distribution of amplitudes of a series of pulses produced by a detector is called a pulse-height spectrometer. The pulse-height spectrometer system generally consists of a detector, preamplifier, an amplifier, and a pulse-height analyzer frequently a multichannel analyzer. These components amplify, shape, analyze and record pulses according to their amplitude.

The charge involved in an individual detector output pulse is

so small that some initial amplification is required prior to processing and analysis. This function is accomplished by the preamplifier which is usually located in close proximity to the detector itself. The preamplifier also serves as an impedance matcher between the detector and the other components. It presents a high impedance to the detector to minimize loading while providing low impedance output to the signal cable and components which follow (101).

The preamplifier output pulse generally has small amplitude and rapid rise and long fall times. Linear amplifiers are used to convert such a low amplitude pulse to one of sufficient amplitude and proper shape to drive the pulse analysis components electronics. Semiconductor detector pulses are generally shaped, using RC circuit elements, into Gaussian-like pulses that have rapid rise and rapid fall times (100).

The multichannel analyzer (MCA) is the component of the pulse-height spectrometer that discriminates and sorts the pulses according to their amplitude. The operation of the MCA involves conversion of pulse amplitude, an analog signal, to an equivalent digital number. The conversion is accomplished by an analog-to-digital converter (ADC). Most ADC's use the Wilkinson-type linear ramp converter to digitize pulse height although other analog-to-digital conversion methods exist.

In the Wilkinson-type converter, a capacitor charges linearly in time to a level which depends on the amplitude of the input pulse. A comparator circuit compares the magnitude of the accumulated capacitor charge with the amplitude of the input pulse. During the time the capacitor is charging, clock pulses from a high-frequency oscillator (about 50 to 100 MHz) are counted. The number of pulses accumulated is proportional

to the charging time of the capacitor which in turn is proportional to the input pulse's amplitude.

The pulse amplitude values from the ADC fall into intervals of pulse height, or channels. The pulse-height distribution is stored in a computer-type memory which has as many addressable locations as the maximum number of channels. The number of memory locations is usually made a power of two with memories of 256 to 4096 channels being most common. The distribution in frequency of pulses observed as a function of pulse height is called the pulse-height spectrum. The pulse-height spectrum can be displayed or recorded on peripheral output devices such as a cathode ray tube or teletypewriter, can be transferred to some computer-accessible media such as paper tape or magnetic tape, or can be processed by microprocessor-type programs for spectrum analysis.

Intrinsic germanium and multichannel analyzer pulse-height spectrometer systems are particularly well-suited for gamma-ray detection and measurement applications where precise gamma-ray energy determination is necessary. Intrinsic germanium possesses the sensitivity and energy resolution required for such detailed analyses. Modern multichannel analyzer systems permit efficient data collection and manipulation so that pulse-height spectrum examination is facilitated. Such systems enable precise definition of the nature and amount of radioactive isotopes in a sample.

APPENDIX E

Thick-Target Bremsstrahlung Computer Program

This appendix presents a listing of the bremsstrahlung computer program described in the Bremsstrahlung Spectrum section of Chapter III. The program is written in Data General FORTRAN 5. It consists of a main program (BREM.FR) and seven subroutines (INT.FR, DFS.FR, AT.FR, ANG.FR, STP.FR, TRN.FR, and PBAT.FR). Each is briefly documented by comment statements appearing at the beginning of the computer code. Bremsstrahlung spectra, contained in the two-dimensional array NIJ(I,J), are written to the test file, BRMTST.OUT, to allow inspection of the spectra, and to the file BRM.OUT which is later used as input for the Least Structure cross section computer program.

```

C *****
C *** PROGRAM BREM.FR ***
C
C PROGRAM TO GENERATE BREM SPECTRA FROM THICK TARGETS
C FOR PHOTONUCLEAR CROSS-SECTION DETERMINATION.
C DATA GENERAL FORTRAN 5 CODE IS USED.
C
C KARL PRADO, MARCH 1983
C *****
C
C REAL NIJ(35,35), E(50), K(50), NK(50),
C . NPCTIJ(35,35), NPCTK(50)
C DIMENSION TITLE(5)
C DATA E/50*0.0/, K/50*0.0/, NK/50*0.0/,
C . NPCTK/50*0.0/
C
C DO 11 I=1,35
C DO 11 J=1,35
C NIJ(I,J)=0.0
C NPCTIJ(I,J)=0.0
11 CONTINUE
C
C OPEN INPUT AND OUTPUT FILES
C
C OPEN 5, 'BRM.IN'
C OPEN 6, 'BRM.OUT'
C
C TEST FILE BRMTST.OUT
C
C OPEN 7, 'BRMTST.OUT'
C
C READ THE INPUT FILE
C 1. TITLE
C 2. EMIN,DE
C 3. NPTS
C
C READ (5,190) TITLE
190 FORMAT (5A4)
C READ (5,290) EMIN,DE
290 FORMAT (F7.4,1X,F6.4)
C READ (5,390) NPTS
390 FORMAT (I3)
C
C DEFINE TARGET PARAMETERS
C
C TTHICK=7.72
C DELTAT=0.0386
C NSLABS=200
C XPLAT=3.065
C
C ENDPOINT AND PHOTON ENERGY BINS SET-UP
C
C XI1=0.0
C DO 10 I=1,NPTS
C E(I)=EMIN+XI1*DE
C K(I)=E(I)-0.5*DE

```

```

X11=X11+1.0
10 CDNTINUE
C
C
C
**** START ENDPOINT ENERGY DO LOOP ****
DO 1 I=1,NPTS
ENDPT=E(I)
DO 222 IJK=1,50
222 NPCTK(IJK)=0.0
C
C
C
**** START PHOTON ENERGY DO LDOP ****
DO 2 J=1,I
CAY=K(J)
C
C
C
*** 2% ENDPDINT SPREAD LOOP ***
DO 111 IPCT=1,3
IF(IPCT.EQ.1)ENDPT=(E(I)-.02*E(I))
IF(IPCT.EQ.2)ENDPT=E(I)
IF(IPCT.EQ.3)ENDPT=(E(I)+.02*E(I))
IF(IPCT.EQ.1)XPCT=.25
IF(IPCT.EQ.2)XPCT=.50
IF(IPCT.EQ.3)XPCT=.25
C
C
C
*** START SLAB SUMMATIDN DO LDOP ***
TEAVE=ENDPT
XNSUM=0.0
SWFRST=1.0
PTHETA=0.0
XI2=1.0
DO 3 ISLAB=1,NSLABS
C
C
C
SET UP SLAB DISTANCES
DISTI=(XI2*DELTAT)-(0.5*DELTAT)
DISTX=TTHICK-DISTI
XI2=XI2+1.0
C
C
C
TEAVE FOR THE SLAB
CALL STP (TEAVE,DTDS)
IF (SWFRST.EQ.1.0) GD TD 71
C
C
C
TEAVE FOR ISLAB > 1
DEETEE=(DELTAT*DTDS)/COS(THETA)
IF (DEETEE.GT.TEAVE) DEETEE=TEAVE
TEAVE=TEAVE-DEETEE
GO TD 77
C
C
C
TEAVE FOR ISLAB = 1
71 DEETEE=(0.5*DELTAT*DTDS)
IF (DEETEE.GT.TEAVE) DEETEE=TEAVE

```

```

TEAVE=TEAVE-DEETEE
SWFRST=0.0
77 CONTINUE
C
C
C   CALCULATE XNT & RMS ANGLE
C
C   CALL ANG (TEAVE,DELTAT,PTHETA,THETA)
C   PTHETA=THETA
C
C   AVNO=6.02217E23
C   TTOP=AVNO*DELTAT
C   BBOT=183.85*COS(THETA)
C   XNT=TTOP/BBOT
C
C
C   INTRINSIC SPECTRUM
C
C   CALL INT (TEAVE,CAY,DE,THETA,XNSK)
C   XNTK=XNSK*XNT
C
C
C   PHOTON ATTENUATION BY REMAINING SLABS
C
C   CALL AT (CAY,DISTX,ATFACT)
C   XNTK=XNTK*ATFACT
C
C
C   ELECTRON TRANSMISSION FACTOR
C
C   CALL TRN (ENDPT,DISTI,TRANS)
C   XNTK=XNTK*TRANS
C
C
C   SUM SLAB CONTRIBUTIONS
C
C   XNSUM=XNSUM+XNTK
C
C   *** END SLAB SUMMATION DO LOOP ***
C
3 CONTINUE
C
C
C   MULTIPLY BY SAMPLE SOLID ANGLE
C
C   XNPHOT=XNSUM*0.3288365
C
C
C   PHOTON ATTENUATION BY FLATTENING FILTER
C
C   CALL PBAT (CAY,XFLAT,PBATEN)
C   XNPHOT=XNPHOT*PBATEN
C
C
C   WRITE PHOTON NUMBER (XNPHOT) TO THE ELEMENT (I,J)
C   OF THE ARRAY NIJ, AND TO THE ELEMENT (J) OF THE
C   ARRAY NK.
C
C   NIJ(I,J)=XNPHOT*XPCT
C   NK(J)=XNPHOT*XPCT
C   NPCTIJ(I,J)=NPCTIJ(I,J)+NIJ(I,J)
C   NPCTK(J)=NPCTK(J)+NK(J)
C
C
C   *** END 28 LOOP ***

```

```
C
C 111 CONTINUE
C
C   *** END PHOTON ENERGY DO LOOP ***
C
C   2 CONTINUE
C
C   WRITE PHOTON SPECTRA TO TEST FILE
C
C   WRITE (7,195) ENDPT
195 FORMAT (5(/),1X,'ENDPOINT ENERGY = ',F7.4,/)
C   WRITE (7,295)
295 FORMAT (/ ,1X,'PHOTON',10X,'PHOTON',/,1X,
C       'ENERGY',10X,'NUMBER',//)
C   DO 44 L=1,I
44 WRITE (7,395) K(L), NPCTK(L)
395 FORMAT (1X,F7.4,4X,E14.6)
C
C   **** END ENDPOINT ENERGY DO LOOP ***
C
C   1 CONTINUE
C
C   WRITE BREM SPECTRA TO FILE BRM.OUT. FILE
C   BRM.OUT CONTAINS THE BREM SPECTRA TO BE
C   USED TO OBTAIN THE PHOTONUCLEAR CROSS-SECTION.
C
C   DO 55 I=1,NPTS
55 WRITE (6,495) (NPCTIJ(I,J), J=1,I)
495 FORMAT (E14.6)
C
C   CLOSE FILES AND END
C
C   CLOSE 5
C   CLOSE 6
C   CLOSE 7
C   CALL EXIT
C   END
```

```
C      *** SUBROUTINE INT.FR ***
C
C      INTEGRATES THE DIFFERENTIAL-IN-ANGLE SCHIFF
C      SPECTRUM (FROM SUB. DFS.FR) OVER ANGLES
C      UP TO THAT DETERMINED BY MULTIPLE SCATTERING
C      IN THE SLAB (FROM ANG.FR).
C
C      SUBROUTINE INT (T,CAY,DE,RADIAN,SPCT)
C
C      SPCT=0.0
C      DRAD=0.0174532
C      XN=0.0
C
C      SUM-OVER-ANGLES.DO LOOP
C
C      DO 2 I=1,44
C      XRAD=XN*DRAD
C      IF(XRAD.GT.RADIAN) GO TO 300
C      CALL DFS (T,CAY,DE,XRAD,TMP)
C      SPCT=SPCT+TMP
C      XN=XN+1.
C      2 CONTINUE
C
C      300 RETURN
C      END
```

```

C      ** SUBROUTINE DFS.FR **
C
C      SUBROUTINE FOR CALCULATING BREM. SPECTRA BASED
C      ON SCHIFF'S DIFFERENTIAL-IN-ANGLE CROSS SECTION.
C      FROM: LENT AND DICKINSON, UCRL-50442.
C
C      SUBROUTINE DFS (T,CAY,DK,ANGL,SPECTR)
C
C      U=0.511
C      Z=74.0
C      PI=3.14159
C      E=T+U
C      ROSQ=5.794E-28
C      SIGMAO=ROSQ*Z*(Z+1.)
C
C      PHI=(Z*ANGL)/U
C
C      IF (CAY.GT.T) GO TO 9
C      FACTOR=1.+(PHI**2.)
C      DIV1=111.*FACTOR
C      DIV2=Z**3.33333
C      SUM1=(DIV2/DIV1)**2.
C      PROD1=CAY/(E-CAY)
C      PROD2=U/(2.*E)
C      SUM2=(PROD2*PROD1)**2.
C      ONEOVR=SUM1+SUM2
C      EMPHI=1./ONEOVR
C      EMLN=ALOG(EMPHI)
C      XKE=CAY/E
C      S1=1.-XKE
C      S2=(4.*(PHI**2.))/FACTOR**2.
C      S3=1.+(1.-XKE)**2.
C      SQBRK=S3-(S2*S1)
C      BRC1=SQBRK*EMLN
C      BRC2=(2.-XKE)**2.
C      B1=(16.*PHI**2.)/FACTOR**2.
C      BRC3=B1*S1
C      BRACE=BRC3-BRC2+BRC1
C      FACT1=1./(FACTOR**2.)
C      F1=(E/U)**2.
C      FACT2=(F1*DK)/CAY
C      FACT3=(2.*SIGMAO)/PI
C      CONST=FACT3*FACT2*FACT1
C      SPECTR=CONST*BRACE
C      GO TO 1
C      9 SPECTR=0.0
C      1 RETURN
C
C      END OF SUBROUTINE
C
C      END

```

```

C      ** SUBROUTINE ANG.FR **
C
C      SUBROUTINE ANG CALCULATES RMS ANGLE (THETA) FOR
C      ELECTRONS IN TUNGSTEN. BICHSEL IN ATTIX RAD. DOSIMETRY I
C      Z=74, A=183.85, 2MEC2=1.022, B=7.35 (INTERPOLATION TABLE
C      XIII, P.221, ATTIX VOL. I, FOR DELTAT = 0.0386 GM/CM2)
C
C      MODIFIED ANGLE (MODTHETA) :
C      1. B=B-1.2 (HANSON A.O., ET AL, PHYS REV 84, 634 (1951))
C          THEREFORE B=6.15
C      2. MODTHETA=(THETA**2.+PTHETA**2.)**.5
C          PTHETA=PREVIOUS SLAB'S ANGLE
C      3. THETA LIMITED TO 0.734 RAD (42 DEG.)
C          (FERDINANDE H., ET AL, NUC INST METH 91, 135 (1971))
C      4. WILL USE B=B-5.01=2.34 BASED ON FWHM DATA
C
C      SUBROUTINE ANG (T,D,PPHI,PHI)
C
C      XNUMER=0.157*74.*75.*D*2.34
C      XDENOM=183.85*T*(T+1.022)
C      PHISQR=XNUMER/XDENOM
C      PHI1=SQRT(PHISQR)
C      PHI=SQRT(PHI1**2.+PPHI**2.)
C      IF(PHI.GT.0.7340) PHI=0.7340
C      RETURN
C      END

```

```

C      ** SUBROUTINE AT.FR **
C
C      SUBROUTINE AT CALCULATES THE PHOTON ATTENUATION FACTOR
C      EXP-(MU*X) MU TUNGSTEN (STORM & ISRAEL, NUC DAT TABLES
C      A7, 565, (1970)). X (DISTX IN MAIN) IS IN GM/CM2 AND IS
C      EQUAL TO TTHICK - DISTI.
C      ***** NOTE DISCONTINUITY AT ABOUT KK=1.0. *****
C      AT KK=1 MU IS FOR 1, AT KK<1 MU IS FOR 0.5, AT KK>1 MU
C      IS FROM CURVE.
C
C      SUBROUTINE AT (KK,X,ATNATN)
C
C      REAL KK, MU
C
C      FIND MU(KK)
C
C      IF(KK.LT.1.0) MU=0.1363
C      IF(KK.EQ.1.0) MU=0.0655
C      IF(KK.GT.1.0.AND.KK.LT.4.0) MU=0.0493*(ALOG10(KK))**2.0
C      . -0.0591*(ALOG10(KK))+0.0577
C      IF(KK.GE.4.0.AND.KK.LT.20.0) MU=0.0359*(ALOG10(KK))**2.0
C      . -0.0431*(ALOG10(KK))+0.0529
C      IF(KK.GE.20.0) MU=0.047*(ALOG10(KK))-0.0037
C
C      CALCULATE ATTENUATION FACTOR
C
C      EXPONT=-1.0*MU*X
C      ATNATN=EXP(EXPONT)
C
C      RETURN
C      END

```

```
C      ** SUBROUTINE STP.FR **
C
C      SUB. STP CALCULATES STOPPING POWER OF ELECTRONS IN
C      TUNGSTEN. BERGER & SELTZER NASA SP-3012
C
C      SUBROUTINE STP (EE,DTDS)
C
C      IF(EE.LT.1.0) DTDS=1.175
C      IF(EE.GE.1.0.AND.EE.LE.15.0) DTDS=1.25*(ALOG10(EE))**2.
C      . +1.175
C      IF(EE.GT.15.0.AND.EE.LE.30.0) DTDS=7.6433*(ALOG10(EE))
C      . -5.391
C      IF(EE.GT.30.0) DTDS=11.91*(ALOG10(EE))-12.59
C
C      RETURN
C      END
```

```
C      ** SUBROUTINE TRN.FR **
C
C      SUB. TRN CALCULATES A TRANSMISSION FACTOR FOR AN
C      ELECTRON BEAM OF ENERGY ENDPT THROUGH A DISTANCE
C      EQUAL TO DISTI. FROM: EBERT, PHYS REV 183, 422,
C      (1969).
C
C      SUBROUTINE TRN (ENDPT,DISTI,TRANS)
C
C      BETA1=387.0*ENDPT
C      BETA2=74.0*(1.+0.000075*74.0*(ENDPT**2.0))
C      BETA3=BETA1/BETA2
C      BETA=(BETA3)**0.25
C
C      ALPHA=(1.0-(1.0/BETA))**(1.0-BETA)
C
C      FAC1=(125.0/(74.0+112.0))*ENDPT*0.565
C      FAC2=(175.0/(74.0+162.0))*0.423
C      REX=FAC1-FAC2
C
C      EXPNT=(-1.0*ALPHA)*((DISTI/REX)**BETA)
C      TRANS=EXP(EXPNT)
C
C      RETURN
C      END
```

```
C   *** SUBROUTINE PBAT.FR ***
C
C   SUBROUTINE PBAT CALCULATES MU (CM2/G) FOR LEAD
C   FOR THE PURPOSE OF FLATTENING FILTER ATTENUATION
C   (STORM AND ISRAEL, NUC DAT TABLES A7, 565 (1970))
C
C   SUBROUTINE PBAT (XE,XD,XF)
C
C   IF(XE.LT.1.0) PBMU=.1590
C   IF(XE.EQ.1.0) PBMU=.0703
C   IF(XE.GT.1.0.AND.XE.LT.3.0) PBMU=.0746*(ALOG10(XE))**2.
C   . -.0812*(ALOG10(XE))+.0637
C   IF(XE.GE.3.0.AND.XE.LE.4.0) PBMU=.0416
C   IF(XE.GT.4.0.AND.XE.LE.15.0) PBMU=.0328*(ALOG10(XE))**2.
C   . -.0357*(ALOG10(XE))+.0513
C   IF(XE.GT.15.0) PBMU=.04977*(ALOG10(XE))-.0038
C
C   P1=-1.0*XD*PBMU
C   XF=EXP(P1)
C
C   RETURN
C   END
```

APPENDIX F

Bremsstrahlung Spectra at 25, 24, 22, 20, 18,
and 15 MeV Endpoint Energies

This appendix presents thick-target bremsstrahlung spectra, with and without the $\pm 2\%$ endpoint energy spread, at selected endpoint energies, obtained from the thick-target bremsstrahlung computer program. The spectra were produced assuming a 7.72 g/cm^2 tungsten target, a radiation cone of 0.329 steradians, and a beam filtration of 31.78 g/cm^2 (2.8 cm) of lead. Although these conditions apply strictly to bremsstrahlung produced by the Sagittaire accelerator, spectral shapes are considered fairly representative of flattened clinical beams generated at the above potentials.

25.0 MEV SPECTRUM

ENERGY BIN	PHOTON ENERGY	PHOTON FLUENCE	ENERGY FLUENCE
1.00	.50	1.198E 00	5.988E-01
2.00	1.50	1.780E 01	2.670E 01
3.00	2.50	1.355E 01	3.387E 01
4.00	3.50	9.606E 00	3.362E 01
5.00	4.50	6.907E 00	3.108E 01
6.00	5.50	5.127E 00	2.820E 01
7.00	6.50	3.898E 00	2.534E 01
8.00	7.50	3.019E 00	2.264E 01
9.00	8.50	2.370E 00	2.015E 01
10.00	9.50	1.879E 00	1.785E 01
11.00	10.50	1.500E 00	1.575E 01
12.00	11.50	1.201E 00	1.381E 01
13.00	12.50	9.629E-01	1.204E 01
14.00	13.50	7.705E-01	1.040E 01
15.00	14.50	6.135E-01	8.896E 00
16.00	15.50	4.829E-01	7.485E 00
17.00	16.50	3.760E-01	6.204E 00
18.00	17.50	2.888E-01	5.055E 00
19.00	18.50	2.176E-01	4.026E 00
20.00	19.50	1.590E-01	3.101E 00
21.00	20.50	1.111E-01	2.277E 00
22.00	21.50	7.179E-02	1.544E 00
23.00	22.50	4.098E-02	9.221E-01
24.00	23.50	1.780E-02	4.183E-01
25.00	24.50	3.081E-03	7.549E-02

25.0 MEV SPECTRUM (+/- 2%)

ENERGY BIN	PHOTON ENERGY	PHOTON FLUENCE	ENERGY FLUENCE
1.00	.50	1.198E 00	5.990E-01
2.00	1.50	1.781E 01	2.671E 01
3.00	2.50	1.355E 01	3.388E 01
4.00	3.50	9.609E 00	3.363E 01
5.00	4.50	6.909E 00	3.109E 01
6.00	5.50	5.128E 00	2.821E 01
7.00	6.50	3.900E 00	2.535E 01
8.00	7.50	3.020E 00	2.265E 01
9.00	8.50	2.371E 00	2.015E 01
10.00	9.50	1.880E 00	1.786E 01
11.00	10.50	1.500E 00	1.575E 01
12.00	11.50	1.202E 00	1.382E 01
13.00	12.50	9.633E-01	1.204E 01
14.00	13.50	7.708E-01	1.041E 01
15.00	14.50	6.138E-01	8.900E 00
16.00	15.50	4.832E-01	7.489E 00
17.00	16.50	3.761E-01	6.206E 00
18.00	17.50	2.891E-01	5.059E 00
19.00	18.50	2.178E-01	4.028E 00
20.00	19.50	1.592E-01	3.104E 00
21.00	20.50	1.113E-01	2.281E 00
22.00	21.50	7.206E-02	1.549E 00
23.00	22.50	4.129E-02	9.291E-01
24.00	23.50	1.821E-02	4.278E-01
25.00	24.50	3.806E-03	9.326E-02

24.0 MEV SPECTRUM

ENERGY BIN	PHOTON ENERGY	PHOTON FLUENCE	ENERGY FLUENCE
1.00	.50	1.105E 00	5.528E-01
2.00	1.50	1.647E 01	2.470E 01
3.00	2.50	1.250E 01	3.125E 01
4.00	3.50	8.845E 00	3.096E 01
5.00	4.50	6.345E 00	2.855E 01
6.00	5.50	4.698E 00	2.584E 01
7.00	6.50	3.563E 00	2.316E 01
8.00	7.50	2.750E 00	2.063E 01
9.00	8.50	2.151E 00	1.828E 01
10.00	9.50	1.698E 00	1.613E 01
11.00	10.50	1.348E 00	1.416E 01
12.00	11.50	1.073E 00	1.233E 01
13.00	12.50	8.531E-01	1.066E 01
14.00	13.50	6.759E-01	9.124E 00
15.00	14.50	5.320E-01	7.714E 00
16.00	15.50	4.118E-01	6.384E 00
17.00	16.50	3.143E-01	5.185E 00
18.00	17.50	2.351E-01	4.114E 00
19.00	18.50	1.709E-01	3.162E 00
20.00	19.50	1.187E-01	2.314E 00
21.00	20.50	7.658E-02	1.570E 00
22.00	21.50	4.317E-02	9.282E-01
23.00	22.50	1.868E-02	4.202E-01
24.00	23.50	3.196E-03	7.511E-02

24.0 MEV SPECTRUM (+/- 2%)

ENERGY BIN	PHOTON ENERGY	PHOTON FLUENCE	ENERGY FLUENCE
1.00	.50	1.106E 00	5.529E-01
2.00	1.50	1.647E 01	2.470E 01
3.00	2.50	1.250E 01	3.126E 01
4.00	3.50	8.847E 00	3.095E 01
5.00	4.50	6.346E 00	2.856E 01
6.00	5.50	4.699E 00	2.584E 01
7.00	6.50	3.564E 00	2.316E 01
8.00	7.50	2.751E 00	2.063E 01
9.00	8.50	2.152E 00	1.829E 01
10.00	9.50	1.699E 00	1.614E 01
11.00	10.50	1.349E 00	1.416E 01
12.00	11.50	1.073E 00	1.234E 01
13.00	12.50	8.534E-01	1.067E 01
14.00	13.50	6.761E-01	9.127E 00
15.00	14.50	5.321E-01	7.716E 00
16.00	15.50	4.120E-01	6.387E 00
17.00	16.50	3.145E-01	5.189E 00
18.00	17.50	2.353E-01	4.117E 00
19.00	18.50	1.711E-01	3.166E 00
20.00	19.50	1.189E-01	2.318E 00
21.00	20.50	7.681E-02	1.575E 00
22.00	21.50	4.358E-02	9.369E-01
23.00	22.50	1.907E-02	4.290E-01
24.00	23.50	3.902E-03	9.169E-02

22.0 MEV SPECTRUM

ENERGY BIN	PHOTON ENERGY	PHOTON FLUENCE	ENERGY FLUENCE
1.00	.50	9.300E-01	4.650E-01
2.00	1.50	1.392E 01	2.088E 01
3.00	2.50	1.052E 01	2.630E 01
4.00	3.50	7.408E 00	2.593E 01
5.00	4.50	5.286E 00	2.379E 01
6.00	5.50	3.891E 00	2.140E 01
7.00	6.50	2.932E 00	1.906E 01
8.00	7.50	2.246E 00	1.685E 01
9.00	8.50	1.741E 00	1.480E 01
10.00	9.50	1.360E 00	1.292E 01
11.00	10.50	1.065E 00	1.118E 01
12.00	11.50	8.332E-01	9.582E 00
13.00	12.50	6.483E-01	8.103E 00
14.00	13.50	4.997E-01	6.746E 00
15.00	14.50	3.797E-01	5.506E 00
16.00	15.50	2.805E-01	4.348E 00
17.00	16.50	2.011E-01	3.319E 00
18.00	17.50	1.378E-01	2.412E 00
19.00	18.50	8.805E-02	1.629E 00
20.00	19.50	4.944E-02	9.642E-01
21.00	20.50	2.115E-02	4.336E-01
22.00	21.50	3.453E-03	7.424E-02

22.0 MEV SPECTRUM (+/- 2%)

ENERGY BIN	PHOTON ENERGY	PHOTON FLUENCE	ENERGY FLUENCE
1.00	.50	9.301E-01	4.650E-01
2.00	1.50	1.392E 01	2.088E 01
3.00	2.50	1.052E 01	2.631E 01
4.00	3.50	7.409E 00	2.593E 01
5.00	4.50	5.287E 00	2.379E 01
6.00	5.50	3.892E 00	2.140E 01
7.00	6.50	2.932E 00	1.905E 01
8.00	7.50	2.247E 00	1.685E 01
9.00	8.50	1.742E 00	1.480E 01
10.00	9.50	1.360E 00	1.292E 01
11.00	10.50	1.065E 00	1.118E 01
12.00	11.50	8.334E-01	9.584E 00
13.00	12.50	6.486E-01	8.108E 00
14.00	13.50	5.001E-01	6.751E 00
15.00	14.50	3.798E-01	5.507E 00
16.00	15.50	2.807E-01	4.351E 00
17.00	16.50	2.012E-01	3.320E 00
18.00	17.50	1.380E-01	2.415E 00
19.00	18.50	8.816E-02	1.631E 00
20.00	19.50	4.962E-02	9.676E-01
21.00	20.50	2.151E-02	4.410E-01
22.00	21.50	4.117E-03	8.851E-02

20.0 MEV SPECTRUM

ENERGY BIN	PHOTON ENERGY	PHOTON FLUENCE	ENERGY FLUENCE
1.00	.50	7.672E-01	3.836E-01
2.00	1.50	1.157E 01	1.735E 01
3.00	2.50	8.700E 00	2.175E 01
4.00	3.50	6.089E 00	2.131E 01
5.00	4.50	4.317E 00	1.943E 01
6.00	5.50	3.155E 00	1.735E 01
7.00	6.50	2.357E 00	1.532E 01
8.00	7.50	1.788E 00	1.341E 01
9.00	8.50	1.369E 00	1.163E 01
10.00	9.50	1.052E 00	9.992E 00
11.00	10.50	8.072E-01	8.476E 00
12.00	11.50	6.158E-01	7.082E 00
13.00	12.50	4.636E-01	5.795E 00
14.00	13.50	3.412E-01	4.606E 00
15.00	14.50	2.439E-01	3.536E 00
16.00	15.50	1.650E-01	2.558E 00
17.00	16.50	1.039E-01	1.714E 00
18.00	17.50	5.750E-02	1.006E 00
19.00	18.50	2.439E-02	4.512E-01
20.00	19.50	3.769E-03	7.350E-02

20.0 MEV SPECTRUM (+/- 2%)

ENERGY BIN	PHOTON ENERGY	PHOTON FLUENCE	ENERGY FLUENCE
1.00	.50	7.674E-01	3.837E-01
2.00	1.50	1.157E 01	1.735E 01
3.00	2.50	8.701E 00	2.175E 01
4.00	3.50	6.090E 00	2.132E 01
5.00	4.50	4.318E 00	1.943E 01
6.00	5.50	3.155E 00	1.736E 01
7.00	6.50	2.358E 00	1.532E 01
8.00	7.50	1.788E 00	1.341E 01
9.00	8.50	1.359E 00	1.164E 01
10.00	9.50	1.052E 00	9.995E 00
11.00	10.50	8.077E-01	8.481E 00
12.00	11.50	6.159E-01	7.083E 00
13.00	12.50	4.637E-01	5.797E 00
14.00	13.50	3.415E-01	4.611E 00
15.00	14.50	2.440E-01	3.538E 00
16.00	15.50	1.652E-01	2.551E 00
17.00	16.50	1.040E-01	1.716E 00
18.00	17.50	5.775E-02	1.011E 00
19.00	18.50	2.465E-02	4.560E-01
20.00	19.50	4.518E-03	8.811E-02

18.0 MEV SPECTRUM

ENERGY BIN	PHOTON ENERGY	PHOTON FLUENCE	ENERGY FLUENCE
1.00	.50	6.190E-01	3.095E-01
2.00	1.50	9.407E 00	1.411E 01
3.00	2.50	7.031E 00	1.758E 01
4.00	3.50	4.885E 00	1.710E 01
5.00	4.50	3.435E 00	1.546E 01
6.00	5.50	2.486E 00	1.367E 01
7.00	6.50	1.836E 00	1.193E 01
8.00	7.50	1.373E 00	1.030E 01
9.00	8.50	1.032E 00	8.770E 00
10.00	9.50	7.736E-01	7.350E 00
11.00	10.50	5.757E-01	6.045E 00
12.00	11.50	4.205E-01	4.836E 00
13.00	12.50	2.985E-01	3.732E 00
14.00	13.50	2.023E-01	2.731E 00
15.00	14.50	1.271E-01	1.842E 00
16.00	15.50	6.954E-02	1.078E 00
17.00	16.50	2.914E-02	4.808E-01
18.00	17.50	4.907E-03	8.588E-02

18.0 MEV SPECTRUM (+/- 2%)

ENERGY BIN	PHOTON ENERGY	PHOTON FLUENCE	ENERGY FLUENCE
1.00	.50	6.190E-01	3.095E-01
2.00	1.50	9.406E 00	1.411E 01
3.00	2.50	7.030E 00	1.758E 01
4.00	3.50	4.885E 00	1.710E 01
5.00	4.50	3.434E 00	1.545E 01
6.00	5.50	2.486E 00	1.367E 01
7.00	6.50	1.836E 00	1.193E 01
8.00	7.50	1.372E 00	1.029E 01
9.00	8.50	1.031E 00	8.767E 00
10.00	9.50	7.737E-01	7.350E 00
11.00	10.50	5.755E-01	6.043E 00
12.00	11.50	4.204E-01	4.835E 00
13.00	12.50	2.984E-01	3.730E 00
14.00	13.50	2.022E-01	2.729E 00
15.00	14.50	1.270E-01	1.841E 00
16.00	15.50	6.965E-02	1.080E 00
17.00	16.50	2.927E-02	4.830E-01
18.00	17.50	5.312E-03	9.297E-02

15.0 MEV SPECTRUM

ENERGY BIN	PHOTON ENERGY	PHOTON FLUENCE	ENERGY FLUENCE
1.00	.50	4.218E-01	2.109E-01
2.00	1.50	6.473E 00	9.709E 00
3.00	2.50	4.771E 00	1.193E 01
4.00	3.50	3.260E 00	1.141E 01
5.00	4.50	2.248E 00	1.012E 01
6.00	5.50	1.589E 00	8.738E 00
7.00	6.50	1.139E 00	7.400E 00
8.00	7.50	8.175E-01	6.131E 00
9.00	8.50	5.814E-01	4.942E 00
10.00	9.50	4.046E-01	3.844E 00
11.00	10.50	2.703E-01	2.838E 00
12.00	11.50	1.681E-01	1.934E 00
13.00	12.50	9.253E-02	1.157E 00
14.00	13.50	3.890E-02	5.251E-01
15.00	14.50	6.128E-03	8.886E-02

15.0 MEV SPECTRUM (+/- 2%)

ENERGY BIN	PHOTON ENERGY	PHOTON FLUENCE	ENERGY FLUENCE
1.00	.50	4.219E-01	2.109E-01
2.00	1.50	6.474E 00	9.711E 00
3.00	2.50	4.772E 00	1.193E 01
4.00	3.50	3.261E 00	1.141E 01
5.00	4.50	2.249E 00	1.012E 01
6.00	5.50	1.589E 00	8.742E 00
7.00	6.50	1.139E 00	7.402E 00
8.00	7.50	8.176E-01	6.132E 00
9.00	8.50	5.818E-01	4.945E 00
10.00	9.50	4.050E-01	3.848E 00
11.00	10.50	2.706E-01	2.842E 00
12.00	11.50	1.686E-01	1.938E 00
13.00	12.50	9.262E-02	1.158E 00
14.00	13.50	3.911E-02	5.280E-01
15.00	14.50	6.831E-03	9.905E-02